2013

Measurement of heavy flavor electron flow in Au + Au collisions at sqrt(s_{NN}) = 62.4 GeV

Lei Ding
Iowa State University

Measurement of heavy flavor electron flow in Au + Au collisions at $\sqrt{s_{NN}}$ = 62.4 GeV

by

Lei Ding

A dissertation submitted to the graduate faculty

in partial fulfillment of the requirements for the degree of

DOCTOR OF PHILOSOPHY

Major: Nuclear Physics

Program of Study Committee:

Craig Ogilvie, Major Professor

Marzia Rosati

Jianwei Qiu

Chunhui Chen

Klaus Schmidt-Rohr

Iowa State University

Ames, Iowa

2013

TABLE OF CONTENTS

LIST OF TABLES

LIST OF FIGURES

ACKNOWLEDGEMENTS

First of all, I would like to express my gratitude to my advisor Craig Ogilvie. Craig's enthusiasm for physics guided me through my PhD work. I have received comprehensive training in the scientific field with a focus on independent research. What I learned from him is invaluable for my future endeavor. I express my thanks to Marzia Rosati for the guidance and support she provided me in the past 5 years. Working with her was a great experience.

I had an enjoyable time working with the ISU experimental nuclear group. Alan Dion shared his broad knowledge of electron analysis with me. I learned a lot about flow and the VTX detector from Maya Shimomura. I also would like to thank Cesar Luiz da Silva, Sarah Campbell, Alex Lebedev, John Hill, John Lajoie and Shawn Whitaker for their encouragement and friendship.

It is my pleasure to be part of the PHENIX collaboration. I am grateful to Yasuyuki Akiba. His advice helped me to perfection my work. The help of Ermias Atomssa, Deepali Sharma, Jianyin Sun on the HBD clusterizer and electron analysis was important for me to accomplish the electron measurement using the HBD detector. I also express my thanks to Shengli Huang, Matt Durham, Rachid Nouicer, Stefan Bathe and John Koster for their kind help on both the data analysis and the hardware work.

Finally, I would like to thank my parents and Richard, for their constant love, patience and support.

ABSTRACT

The measurement of the nuclear modification factor $R_{\rm AA}$ and azimuthal anisotropy v_2 of single electrons from semi−leptonic decay of open heavy flavor mesons in the PHENIX experiment has provided important insight into the properties of the Quark Gluon Plasma (QGP). PHENIX results of $R_{\rm AA}$ and v_2 in Au+Au collision at $\sqrt{s_{NN}} = 200$ GeV for heavy-flavor decays are comparable to the results of light hadrons. This indicates that both the flow and the energy loss characteristics in heavy quarks are similar as in light quarks, which is not well understood.

We have extended the PHENIX systematic study of the invariant yield and azimuthal anisotropy of heavy flavor electrons by reducing the beam energy to $\sqrt{s_{NN}} = 62.4$ GeV. At this energy, the medium formed in Au+Au collisions is expected to have a lower energy density. A large Cronin enhancement is observed in the yield of heavy flavor electrons at this lower energy. There is a hint of heavy flavor suppression in the most central collisions at p_T larger than 3 GeV/c. We will also show that non-zero v_2 of heavy flavor electrons is observed in the mid centrality events.

CHAPTER 1. INTRODUCTION

The Quark Gluon Plasma (QGP), a color deconfined state that once existed in the very early stage of the universe after the big bang, is thought to be created in ultra-relativistic heavy ion collisions. It is of great interest to understand the properties of the QGP. The Relativistic Heavy Ion Collider (RHIC) is designed to collide heavy nuclei to create the QGP at very high temperature and large density.

1.1 Quark Gluon Plasma

Quantum Chromodynamics (QCD) is a theory of strong interactions between the quarks and gluons. In normal conditions, quarks and anti-quarks are confined in color neutral hadrons and mesons, and cannot exist as independent particles. However, at very large density or very high temperature, QCD allows normal matter to transition to a so-called Quark Gluon Plasma (QGP) in which the gluons and quarks are deconfined [1]. Fig. 1.1 shows the QCD phase diagram. At low temperature and low density, the quarks and anti-quarks are confined in nucleons and exist as hadron matter. As temperature or density increases, beyond the phase transition point, the quarks and gluons form the QGP. The critical point of the transition is around $T_c = 170$ MeV and an energy density around 1 GeV/fm^3.

1.2 Heavy Ion Collisions

The QGP can be created in the ultra-relativistic heavy ion collisions in RHIC and the Large Hadron Collider (LHC). Ref. [2] is a summary of the early physics results and the evidence of the creation of the QGP in the four experiments at RHIC. However, since the medium lives only for a short time after the collision, around 10 fm/c, the only way to study the properties of the

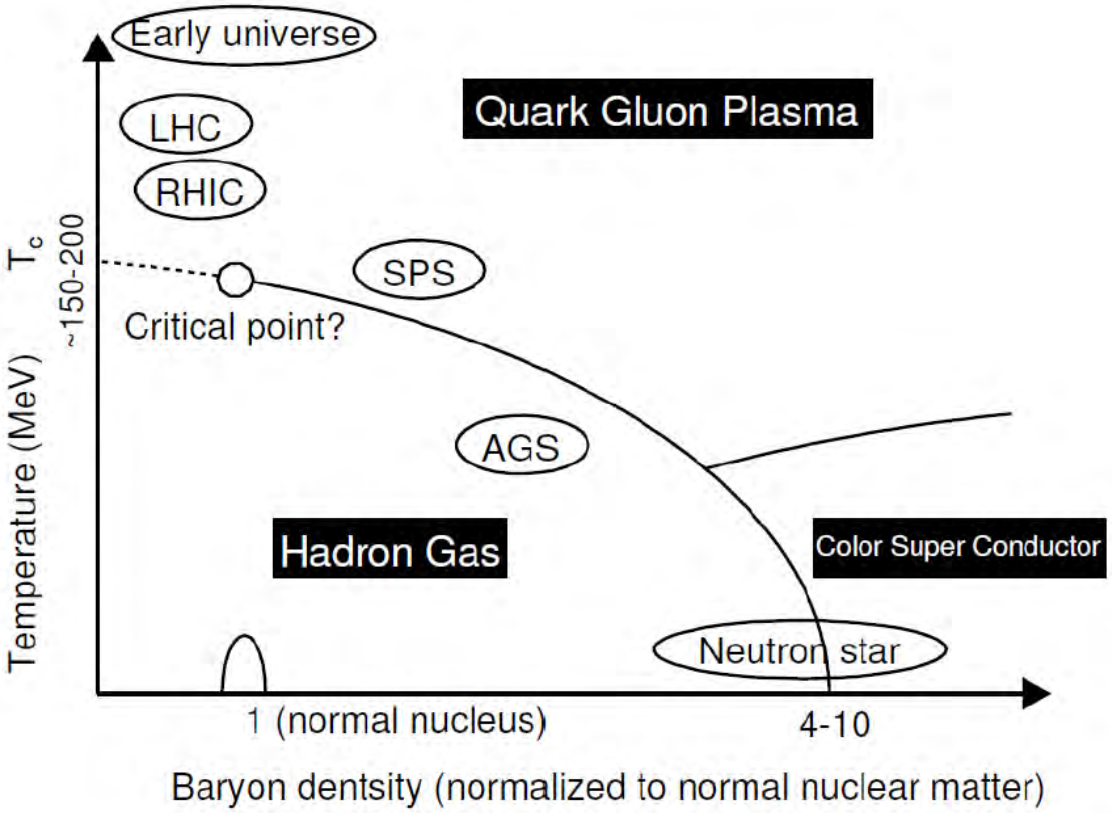

Figure 1.1: Schematic QCD phase diagram.

medium is to use the particles that are created in the collision and interact with the medium, as probes of the medium. There are two kinds of probes: hard probes and electromagnetic probes. The hard probes are particles produced in the hard scattering at the initial stage of the collisions, for instance, jets and particles containing heavy quarks. The hard probes carry information from the early stage of the interaction, and by studying how hard probes interact with the medium and lose energy in the medium, we can understand the properties of the QGP. The electromagnetic probes are leptons and photons with long mean free path. They carry the information about the initial state of their creation.

In this analysis, we will focus on the heavy quarks and the electrons from the heavy meson decays.

1.3 Heavy Quarks in the Heavy Ion Collisions

1.3.1 Heavy Quark Production

Heavy quarks, including charm and bottom, are mainly produced by parton-parton collisions in the early stage of the collisions because of their large mass. These quarks propagate through and interact with the medium. Compared to light quarks, which can be produced in soft and hard processes during all stages of the collisions, heavy quarks are considered as clean and important probes of the QGP created in the collisions.

The heavy quark production cross section in p + p collisions can be predicted by a perturbative QCD (pQCD) calculation. For example, at the Tevatron, where the collision energy is 1.8 TeV, the bottom quark production and the charm quark production is consistent with the next-to-leading-order (NLO) pQCD calculation [3, 4]. At RHIC, the heavy quark production in p + p collisions at $\sqrt{s_{NN}}$ = 200 GeV is also consistent with the upper limit of the fixed-order-plus-next-to-leading-log (FONLL) pQCD calculation [5]. The heavy quark production cross section can be used as the baseline to study the modification of the heavy quarks in the medium.

1.3.2 Modification of Heavy Quarks in the Medium

After the heavy quarks are produced in the collisions, they propagate through and interact with the QGP. The yield of the heavy quarks is modified by the medium. The nuclear modification factor $R_{\rm AA}$ is the observable to quantify the modification of the particle in the medium compared to the yield in p + p collisions. $R_{\rm AA}$ is defined as

$$R_{\rm AA} \equiv \frac{dN_{AA}}{T_{AB} \times d\sigma_{pp}} = \frac{dN_{AA}}{\langle N_{coll} \rangle \times dN_{pp}} \tag{1.1}$$

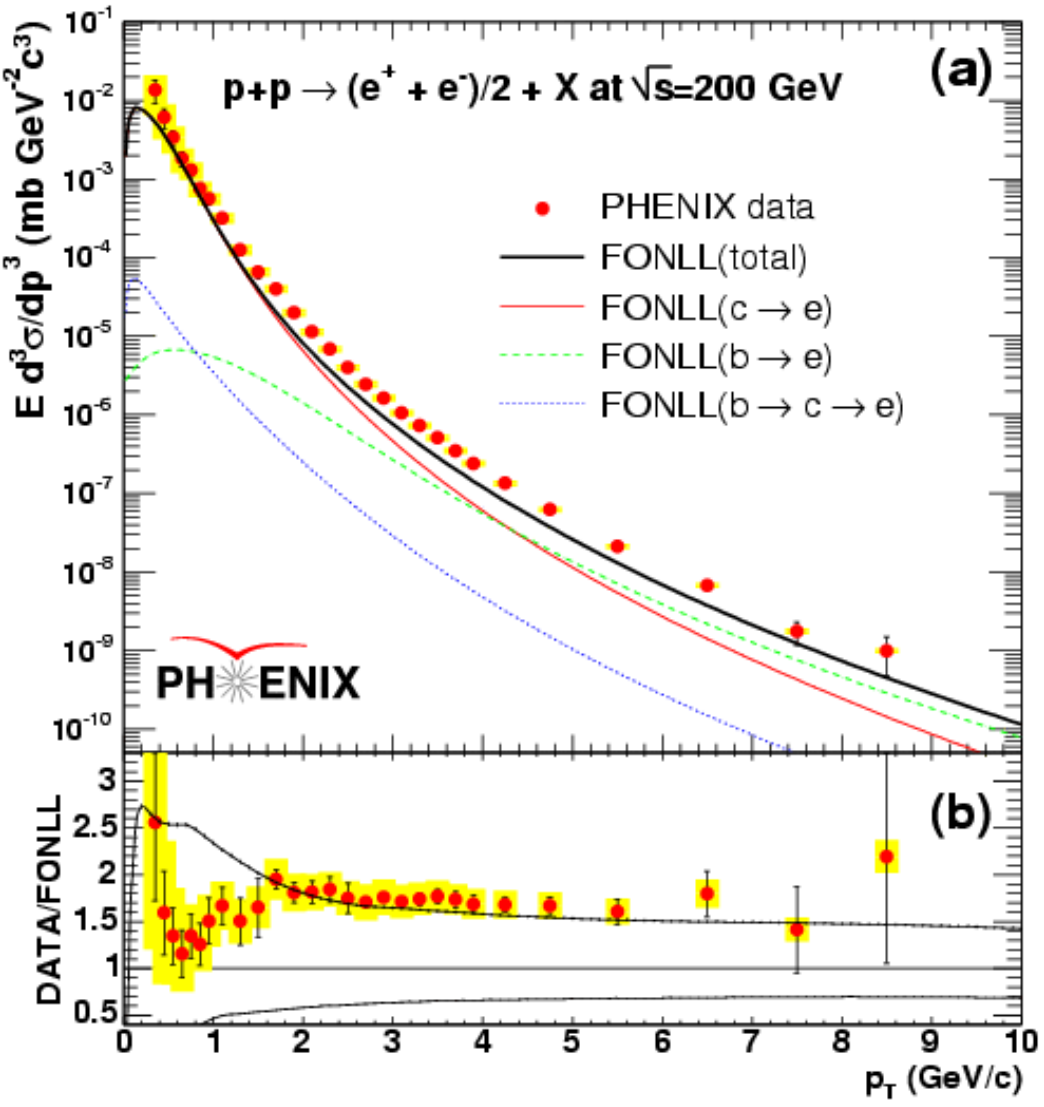

Figure 1.2: Invariant cross section of heavy flavor electrons in p + p collisions at $\sqrt{s_{NN}} = 200$ GeV at RHIC and the FONLL calculation [5].

Where N_{AA} is the yield of the particle in A + A collisions, σ_{pp} is the cross section of the particle in p + p collisions, T_{AB} is the nuclear overlap function, and $\langle N_{coll} \rangle$ is the average number of binary collisions happen in one A + A collision for a given centrality.

If the particle does not interact with the medium, then the yields can be described by the superposition of $\langle N_{coll} \rangle$ independent p + p collisions and $R_{\rm AA}$ should be equal to unity. If $R_{\rm AA}$ is smaller than 1, the particle yield is suppressed in the medium. If $R_{\rm AA}$ is larger than 1, the particle yield is enhanced in the medium. Fig. 1.3 shows the $R_{\rm AA}$ of π^0 in Au + Au collisions at $\sqrt{s_{NN}}$ = 200 GeV for central events and peripheral events measured at PHENIX [6]. The suppression in the central events is greater than the peripheral events, which means the π^0 suffers from parton energy loss in the QGP created in the central Au + Au collisions at $\sqrt{s_{NN}}$ = 200 GeV.

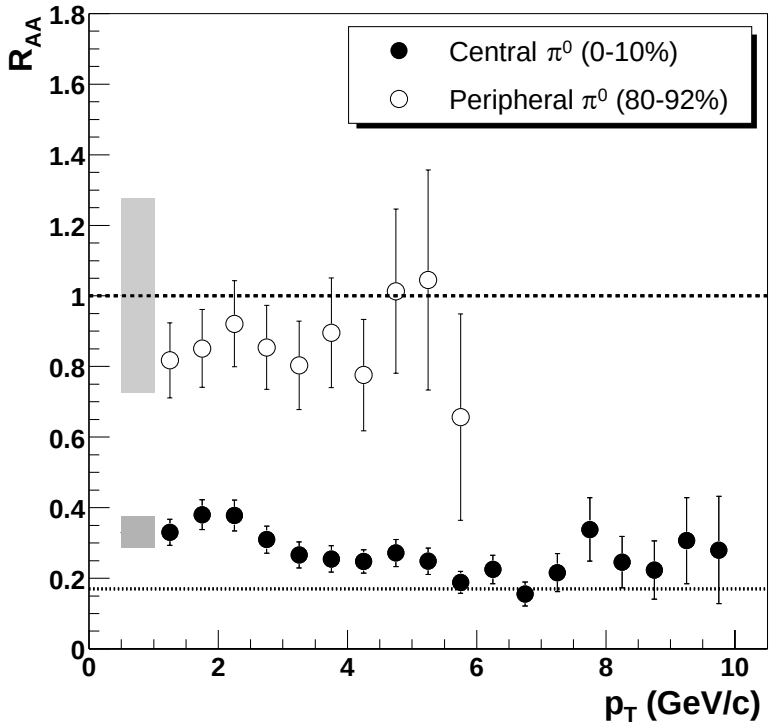

Figure 1.3: The $R_{\rm AA}$ of π^0 in Au + Au collisions at $\sqrt{s_{NN}}$ = 200 GeV for central events and peripheral events [6].

1.3.2.1 Energy Loss of Heavy Quarks

The energy-loss mechanism of heavy quarks is not expected to be the same as that of light quarks. The major way quarks are modelled to lose energy in the medium is through gluon radiation. However, the gluon radiation from massive quarks and from massless partons are different, since at angles smaller than the ratio of quark mass to energy the gluon radiation is highly suppressed: this is the so-called dead cone effect [7, 8]. For heavy quarks, because of their large mass, it is predicted that the smaller angle gluon radiation is suppressed and heavy quarks have less radiative energy loss in the medium compared with light quarks. However, the PHENIX measurement of single electrons from heavy flavor meson semi-leptonic decays shows a large suppression in $R_{\rm AA}$ (the top panel in Fig. 1.4) in Au + Au collisions at $\sqrt{s_{NN}}$ = 200 GeV [9, 10]. The suppression of heavy flavor electrons is comparable to π^0 at high p_T, which indicates that the heavy quarks lose a significant amount of energy as they propagate through the medium before fragmentation. This result is contrary to the theory prediction. It is possible that, although the energy loss of light quarks is dominated by the gluon radiation, a large part of the energy loss of heavy quarks is the collisional energy loss, especially at low to intermediate p_T [11, 12, 13, 14, 15].

1.3.2.2 Cold Nuclear Matter Effect

The cold nuclear matter (CNM) effects are initial state effects in Au + Au collisions which can also be reflected in the final state spectra. These initial state effects, for example, modification of the parton distribution in the nucleus or the Cronin effect, do not exist in p + p collisions, but exist in both d+A and A+A collisions. These effects can compete with the hot nuclear effect (the energy-loss and modification in the QGP). It is important to understand these for heavy-flavor to correctly interpret the A + A results.

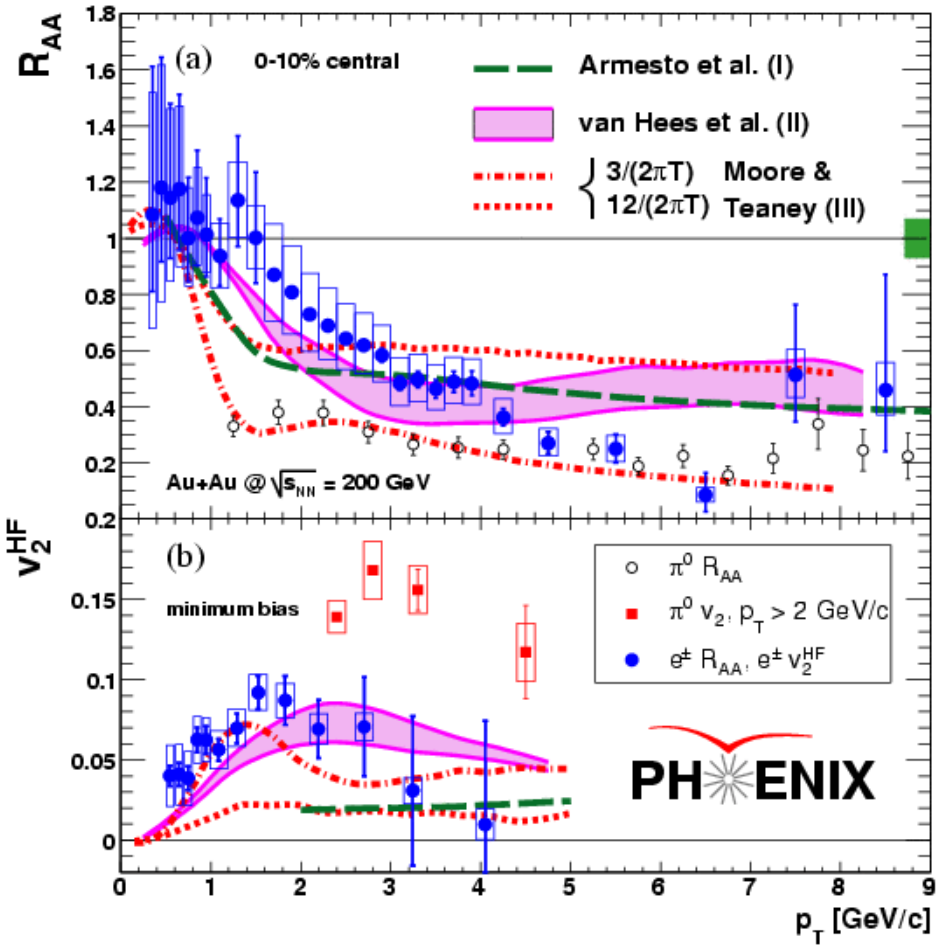

Figure 1.4: The $R_{\rm AA}$ (top) and v_2 (bottom) of single electrons from heavy flavor meson semi-leptonic decays in Au + Au collisions at $\sqrt{s_{NN}}$ = 200 GeV compare to π^0 measurement and multiple theory models [9].

Gluon Shadowing

The European Muon Collaboration (EMC) experiment [16] finds out that the ratio of the nuclear Parton Distribution Functions (nPDF) to those of free nucleons is a function of square of momentum transfer Q^2 and momentum fraction x. In nuclei, nucleons shadow each other and modify the nPDF. As shown in Fig. 1.5, in the small x region, if the modification is smaller than 1, then it is called shadowing. The distribution of gluons in the nucleus can affect the heavy quark cross section since the heavy quarks are mainly produced by the gluon fusion in the collisions.

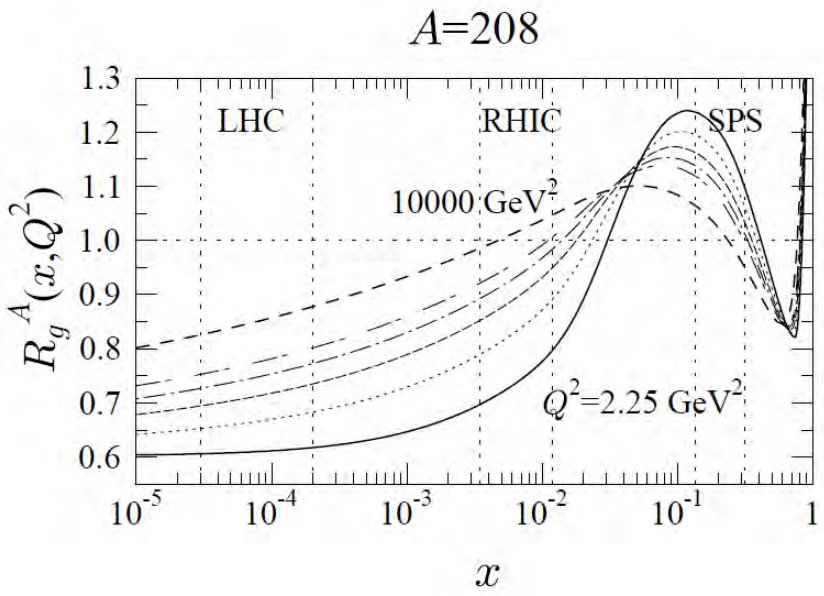

Figure 1.5: The ratio R_g^A for nucleus A = 208 according to EKS98 [17].

Cronin Effect

The Cronin effect is the observation that the yield of particle at moderate p_T increases faster than the number of binary collisions. The simplest explanation of the Cronin effect is that, in the collisions, before the interaction, partons in the nucleus undergo multiple scattering which boosts the momentum of the scattered parton in the transverse direction. The boost broadens the parton p_T spectrum and causes an enhancement of the final state particles at the moderate p_T.

The Cronin effect was first observed in p + A collisions in the 1970s [18]. The PHENIX measurement of the nuclear modification factor R_{dAu} for the charged pions, kaons and protons in d + Au collisions at $\sqrt{s_{NN}} = 200$ GeV [19] shows that the Cronin enhancement increases as the mass of the particle increases (Fig. 1.6). As shown in Fig. 1.7, the Cronin enhancement also increases as the collision energy decreases. Because of the large mass, the Cronin effect for heavy flavor mesons is expected to be much larger than for light mesons. Fig. 1.8 shows the Cronin enhancement for heavy flavor electrons in d + Au collisions at $\sqrt{s_{NN}} = 200$ GeV at moderate p_T. Fig. 1.9 compares the R_{AA} and R_{dAu} for π^0 and heavy flavor electrons in Au + Au or d + Au collisions at $\sqrt{s_{NN}} = 200$ GeV. The enhancement for heavy flavor electrons is much larger than the π^0. In Au + Au collisions, the Cronin effect also exists and can be reflected in the final state R_{AA}.

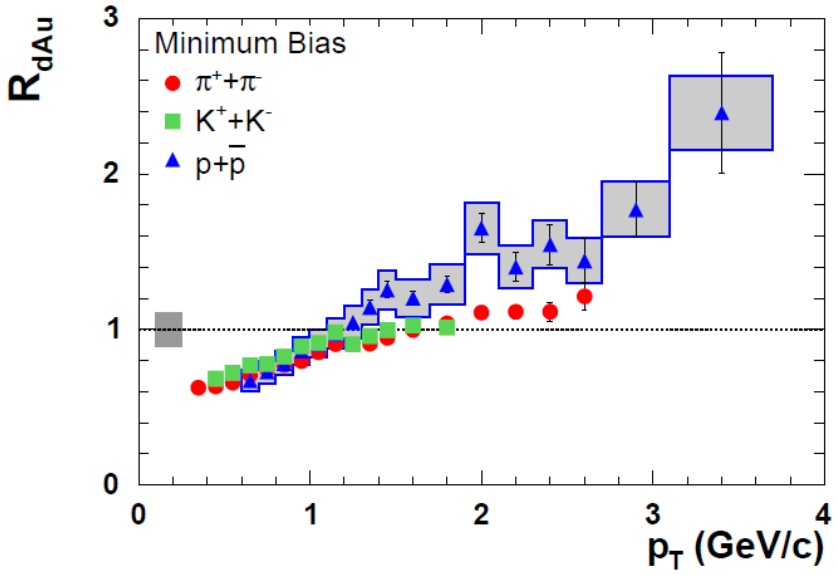

Figure 1.6: R_{dAu} for pions, kaons, and protons in d + Au collisions at $\sqrt{s_{NN}} = 200$ GeV measured in PHENIX. [19]

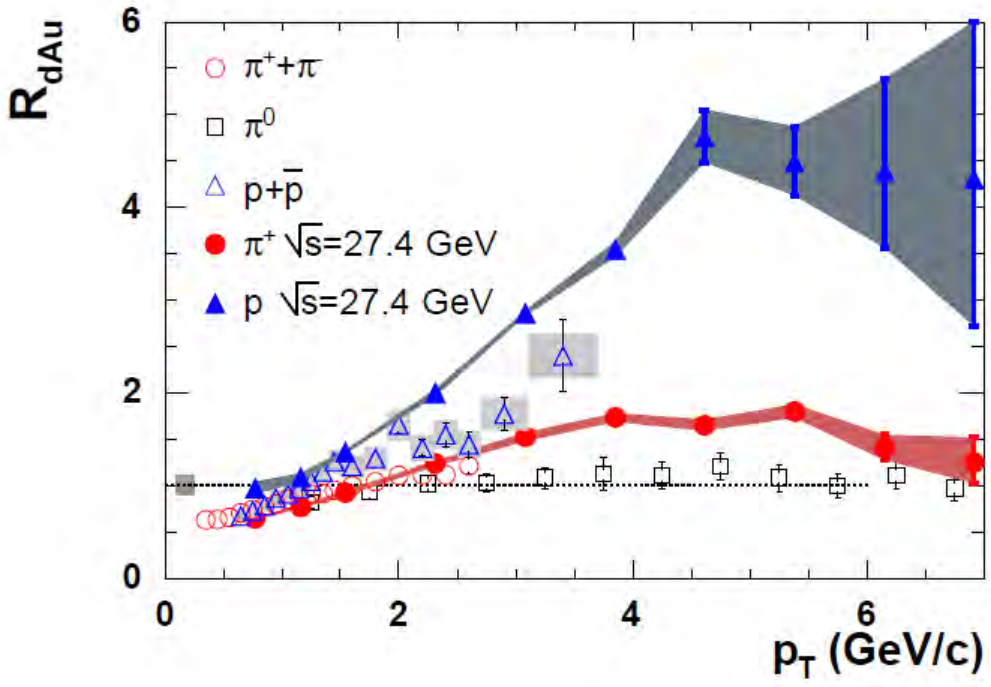

Figure 1.7: R_{dAu} for pions, kaons, and protons in d + Au collisions at $\sqrt{s_{NN}} = 200$ GeV and 27.4 GeV [19]

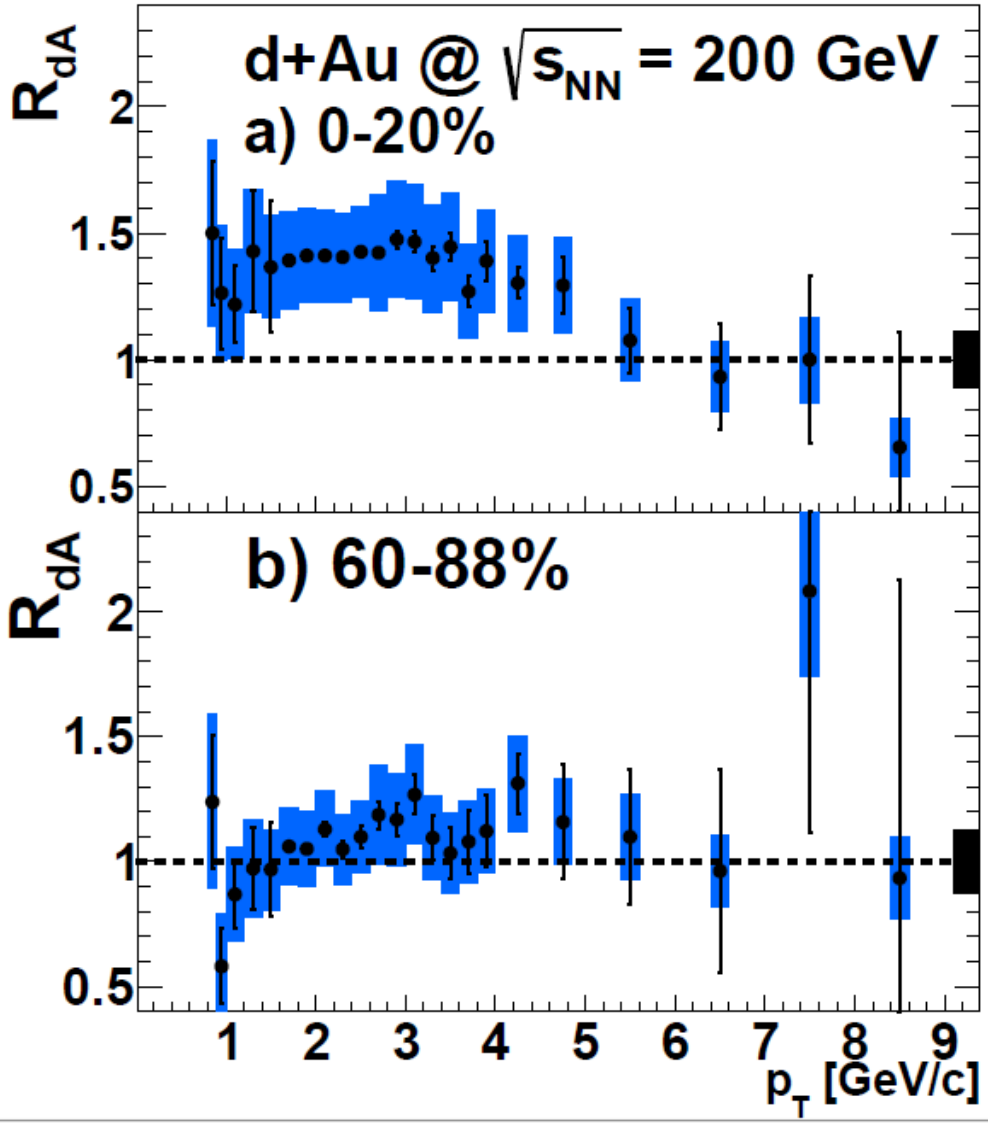

Figure 1.8: R_{dAu} for heavy flavor electrons in d + Au collisions at $\sqrt{s_{NN}} = 200$ GeV [20]

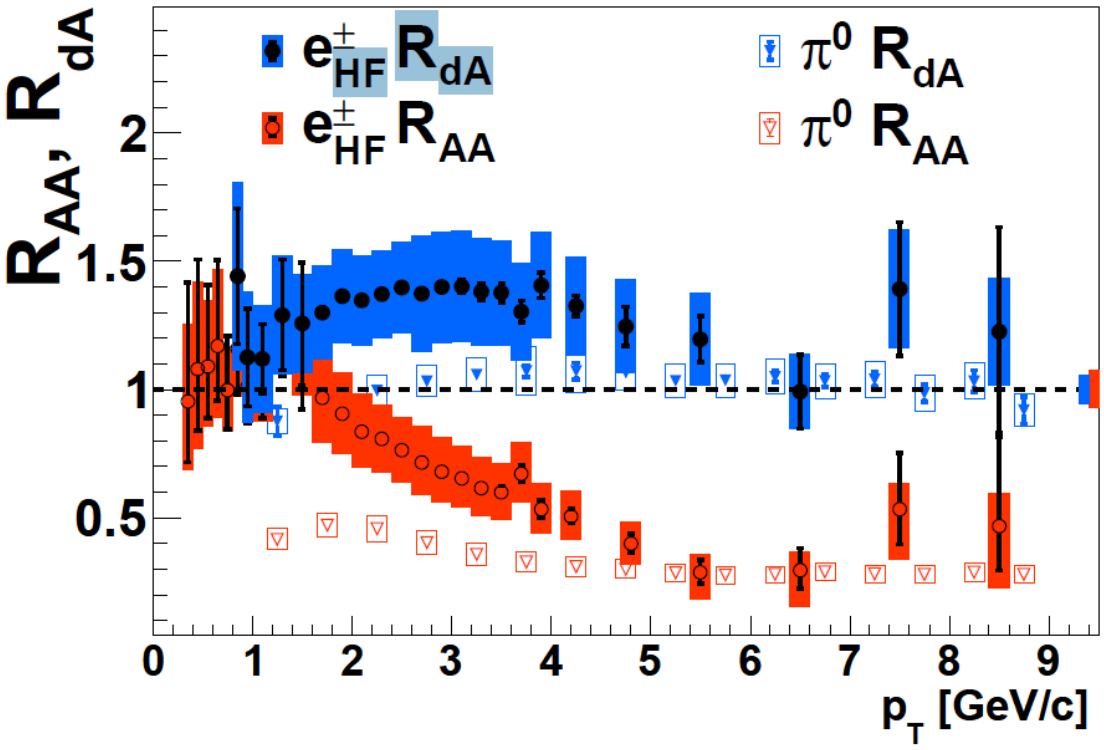

Figure 1.9: Comparison of the $R_{\rm AA}$ and $R_{\rm dAu}$ for π^0 and heavy flavor electrons in Au + Au or d + Au collisions at $\sqrt{s_{_{NN}}} = 200$ GeV [20].

Enhancement due to Radial Expansion of the Medium

In central collisions of heavy nuclei, the radial expansion of the medium can boost the particle p_T, hence modify the p_T distribution of the particle and cause an enhancement of particle yield in the low to moderate p_T [21, 22]. Because the enhancement caused by the radial flow increases with the flow velocity and the particle mass, especially for the nonrelativistic p_T, it may be observable in the heavy flavor measurement, especially at lower beam energy where the initial p_T distribution of heavy quarks is steeper.

The blast wave model is a simple hydrodynamic motivated model to describe the particle distribution assuming that local equilibration is achieved. In the blast wave model, particles move with a collective radial flow velocity field. The particle p_T spectral shape is given by Eq. 1.2 [23] when assuming the particle density is uniform in a hard sphere, the kinetic freeze-out temperature is T_{fo} and the radial flow velocity is β

$$\frac{dN}{p_\perp dp_\perp} \propto \int_0^R r dr m_\perp I_0\left(\frac{p_\perp \sinh\rho}{T_{fo}}\right) K_1\left(\frac{m_\perp \cosh\rho}{T_{fo}}\right) \tag{1.2}$$

Here I_0 and K_1 are the modified Bessel functions, and the radial boost rapidity is

$$\rho = \tanh^{-1}(\beta) \tag{1.3}$$

and

$$\beta(r) = \beta_{max}\left(\frac{r}{R}\right)^n \tag{1.4}$$

Where β_{max} is the maximum velocity at the surface of the blast wave, and r/R represents the relative radial position in the thermal medium. Ref. [24] systematically studied the identified particle spectra using the blast wave model and determined T_{fo} and β_{max} in p + p, d + Au collisions at at $\sqrt{s_{NN}}$ = 200 GeV and Au + Au collisions at $\sqrt{s_{NN}}$ = 200, 130 and 62.4 Gev.

Fig. 1.10 shows the invariant yield of heavy flavor electrons in the 10% central Au + Au collisions at $\sqrt{s_{NN}}$ = 130 GeV and the theoretical curves for D and B mesons from the PYTHIA calculation and the blast wave model [25]. Remember that the curves for the D and B mesons calculated by the blast wave function assumes that D and B mesons achieve local equilibrium in the medium. The blast wave curves show enhancement at low to moderate p_T compared to PYTHIA calculation.

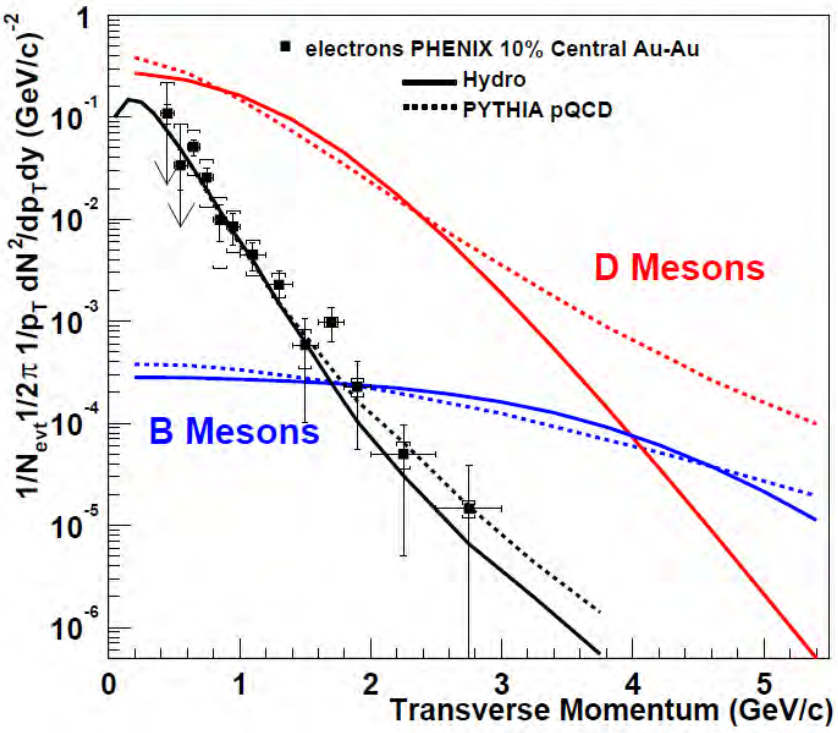

Figure 1.10: Invariant yield of heavy flavor electron in the 10% central Au + Au collisions at $\sqrt{s_{NN}} = 130$ GeV and the theoritical curves for D and B mesons from the PYTHIA calculation and the blast wave model [25].

1.3.3 Flow and Azimuthal Anisotropy of Heavy Quarks

The azimuthal anisotropy v_2 is another important way to study the energy-loss mechanism of the particle in the medium and the property of the medium. The azimuthal anisotropy of particles' distribution in the non-central heavy ion collisions comes from the anisotropic overlap area of the colliding nuclei in geometry. Because of the geometrical anisotropy of the colliding matter, the spatial distribution of the initial energy density of the medium is also anisotropic, which causes a pressure gradient in the medium to push particles to move faster in the shortest direction of the medium. Fig. 1.11 shows a schematic view of the flow in non-central heavy ion collisions.

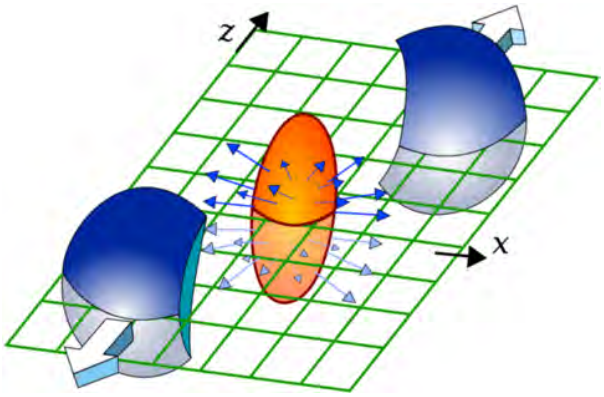

Figure 1.11: Schematic view of the flow in non-central heavy ion collisions.

In the case of heavy quarks, in the thermodynamic limit, the low p_T heavy quarks can be thermalized and join the collective flow of the medium. Even for heavy quarks at high p_T, although they may not be thermalized, the energy loss in the shortest direction of the medium is smaller than the loss in the longest direction. The path length dependence of the energy loss also causes an azimuthal dependence of the momentum distribution of the heavy quarks.

The azimuthal anisotropy v_2 is defined as the second Fourier coefficient in Eq. 1.5.

$$\frac{dN}{d\phi} = N_0(1 + 2v_1\cos(\phi - \Phi_{RP}) + 2v_2\cos 2(\phi - \Phi_{RP}) + 2v_3\cos 3(\phi - \Phi_{RP}) + ...) \qquad (1.5)$$

Where N is the particle yield, ϕ is the azimuth angle of the particle, Φ is the reaction plane angle which represents the direction between the centers of the nuclei. The first Fourier coefficient v_1 is cancelled due to symmetry reasons. The higher order Fourier coefficients are difficult to measure for heavy quarks due to finite reaction plane resolution and limited statistics. Hence, in this analysis, we will focus on the second Fourier coefficient term v_2 for the heavy quarks.

The bottom panel of Fig. 1.4 shows the v_2 of heavy flavor electrons and π^0 in Au + Au collisions at $\sqrt{s_{NN}} = 200$ GeV [9, 10]. The non-zero v_2 of heavy flavor electrons shows us that the heavy quarks flow in the QGP.

1.4 Measurements of Heavy Flavor in RHIC and LHC

In experiments, heavy quarks can not be measured directly since they hadronize to open heavy flavor mesons and heavy flavor quarkonia, for instance J/ψ, after the collision. The suppression of J/ψ mesons is observed in d + Au and Au + Au collisions [26, 27], as shown in Fig. 1.12 and 1.13. However, the final state quarkonia effects, such as screening is a mechanism of suppression. Recombination of J/ψ also affects the final yields. These complications make interpretation of the J/ψ yields difficult.

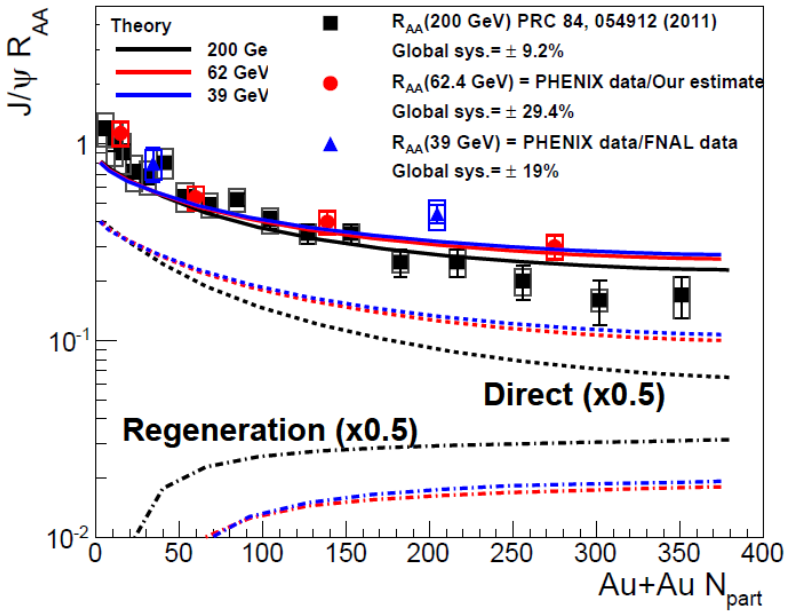

Figure 1.12: $R_{\rm AA}$ of J/ψ in Au + Au collisions at $\sqrt{s_{NN}}$ = 39, 62.4, 200 GeV [27].

Open heavy flavor mesons could be measured through the decay products in the experiment. In PHENIX, before the installation of the Silicon Vertex Tracker (VTX), the open heavy flavor mesons can be measured indirectly through the electrons or muons from the heavy flavor meson semi-leptonic decays. Ref. [9, 10] observed large suppression and non-zero flow of heavy flavor electrons in Au + Au collisions at $\sqrt{s_{NN}}$ = 200 GeV. Ref. [20] observed the Cronin enhancement in $R_{\rm dAu}$ of heavy flavor electrons in d + Au collisions at $\sqrt{s_{NN}}$ = 200 GeV. The STAR experiment also observed the suppression of heavy flavor electrons at high p_T in Au + Au collisions at $\sqrt{s_{NN}}$ = 200 GeV [28], which is consistent with the PHENIX results.

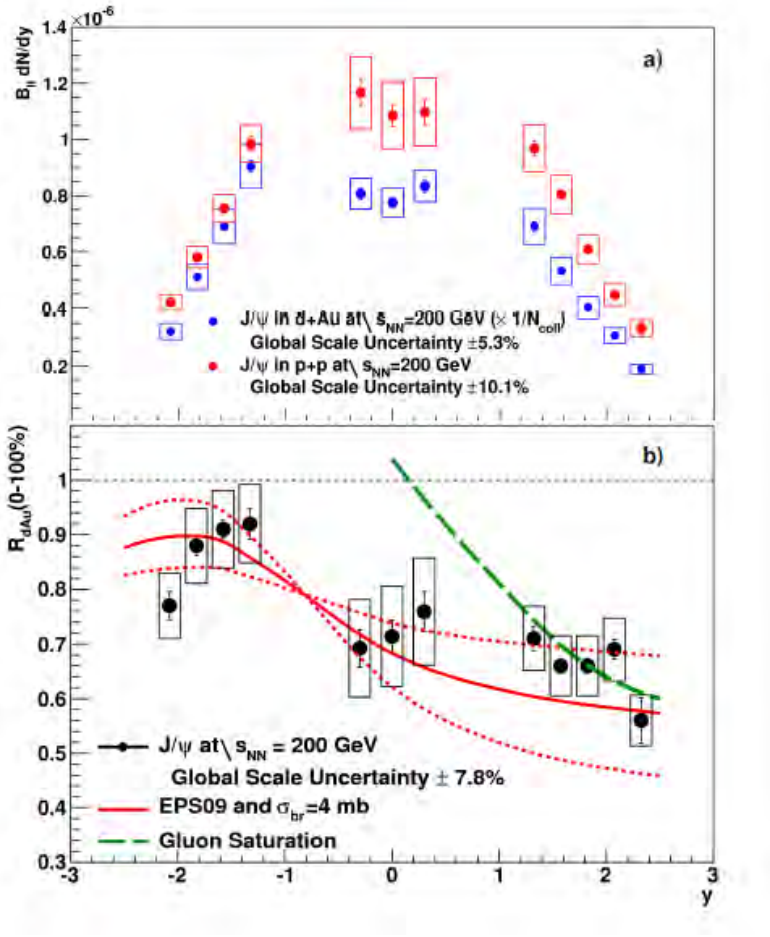

Figure 1.13: R_{AA} of J/ψ in p + p, d + Au and Au + Au collisions at $\sqrt{s_{NN}} = 200$ GeV vs rapidity [26].

In the Large Hadron Collider (LHC), with a much larger collision energy, the nuclear modification factor and v_2 of D mesons are measured in Pb + Pb collisions at $\sqrt{s_{NN}} = 2.76$ TeV with ALICE experiment [29, 30]. Large suppression and non-zero v_2 of D mesons was observed up to $p_T = 10$ Gev/c, as shown in Fig. 1.14

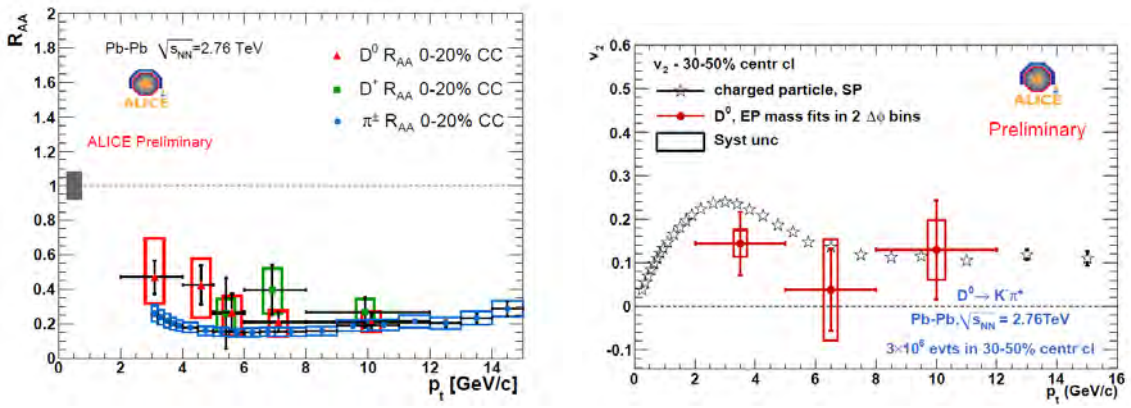

(a) R_{AA} [29] (b) v_2 [30]

Figure 1.14: The ALICE measurement of R_{AA} and v_2 of D mesons in Pb + Pb collisions at $\sqrt{s_{NN}}$ = 2.76 TeV.

1.5 Measurement of Heavy Quarks at $\sqrt{s_{NN}}$ = 62.4 GeV

Since heavy quark energy loss is not yet understood, it is important to change the energy density of the QGP and investigate how heavy quarks interact with a lower-energy QGP. In Run-10, RHIC started the energy scan program and delivered Au + Au collisions at $\sqrt{s_{NN}}$ = 19.5, 39, 62.4 and 200 GeV.

Ref. [31, 32] shows that the suppression and flow of light hadrons at 62.4 GeV are consistent with or slightly less than at 200 GeV. The measurement of J/ψ in Au + Au collisions at $\sqrt{s_{NN}}$ = 62.4 GeV also shows the suppression of J/ψ [27] (Fig. 1.12). However, as we discussed, the final state effects (recombination, color screening) can impact the suppression in the J/ψ yield.

For open heavy flavor mesons, the p_T spectrum at 62.4 GeV is expected to be steeper than the spectrum at 200 GeV. The suppression and flow due to energy loss are expected to be smaller than 200 GeV, however, at the same time, the Cronin enhancement and enhancement due to the blast wave for heavy mesons at 62.4 GeV is larger than that at 200 GeV. The measurement of heavy flavor electrons in Au + Au collisions at 62.4 GeV will provide rich information about the energy density dependence of energy loss of heavy flavors in the medium, the Cronin effect in the initial state, and the properties of the medium at low energy.

CHAPTER 2. EXPERUMENT SETUP

This chapter introduces the accelerator and the detector setup during the 2010 RHIC run (Run-10). We will focus on the detectors which are used for electron analysis, especially on the HBD detector which plays an significant role in the electron identification and background elimination.

2.1 The Relativistic Heavy Ion Collider

The Relativistic Heavy Ion Collider (RHIC), located at Brookhaven National Laboratory (BNL) in New York, is the second largest heavy ion accelerator in the world. It is also the only collider which collides polarized protons. The RHIC is designed to collide a broad range of nuclear species (p + p, Au + Au, Cu + Cu, d + Au, U + U, Cu + Au) at a wide range of center of mass energies from $\sqrt{s_{NN}}$ = 7 GeV to 200 GeV (or 500 GeV for p + p) to study the properties of the matter under extremely high density and high temperature.

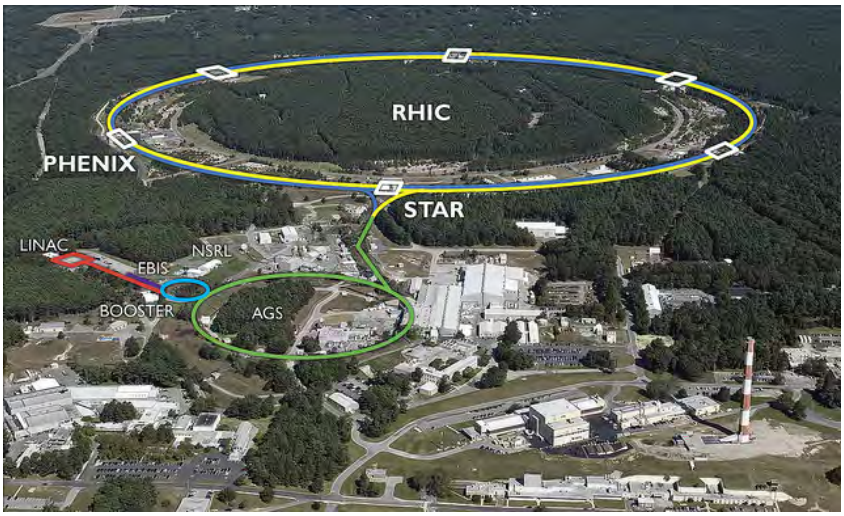

Figure 2.1: The Relativistic Heavy Ion Collider.

Four experiments, PHOBOS, BRAHMS, STAR and PHENIX were built on the RHIC ring to study the collisions. The PHENIX experiment is located at the 8 o'clock position of the ring.

2.2 The PHENIX Experiment

PHENIX (Pioneering High Energy Nuclear Interaction eXperiment) is a complex detector system designed to study the property of the QGP via collisions of heavy ion particles. The PHENIX consists a number of independent detector subsystems. Fig. 2.2 shows the PHENIX detector system in Run-10. The global detectors, including the Beam-Beam Counters (BBC), Zero-Degree Calorimeters (ZDC), and Reaction Plane Detector (RXNP), work as triggers and also provide information about the collisions, such as the collision vertex position, centrality measurement, and reaction plane information. The two central spectrometers, including Drift Chamber (DC), Pad Chambers (PC1 and PC3), Ring Imaging Cerenkov Counter (RICH), Time Expansion Chamber (TEC), Time of Flight detector (TOF), and Electromagnetic Calorimeter (EMCal), provide particle identification capabilities for charged tracks and also measure momentum and energy of charged tracks, energy of photons. The central arms covers rapidity range of $|\eta| < 0.35$. The top half of Fig. 2.2 shows the detectors in the central arms in Run-10. The Hadron Blind Detector (HBD) is an upgrade of the PHENIX experiment in Run-9 and Run-10 for the measurement of electron pairs. In addition to central spectrometers, two muon arms measure muons in the forward and backward rapidity regions ($1.2 < |\eta| < 2.4$). The muon arms include the Resistive Place Chambers (RPC), Muon Tracker (MuTr) and Muon Identifier (MuID). The bottom half of Fig. 2.2 shows the detectors in the muon arms in Run-10. A summary of the PHENIX detector system can be found in [33].

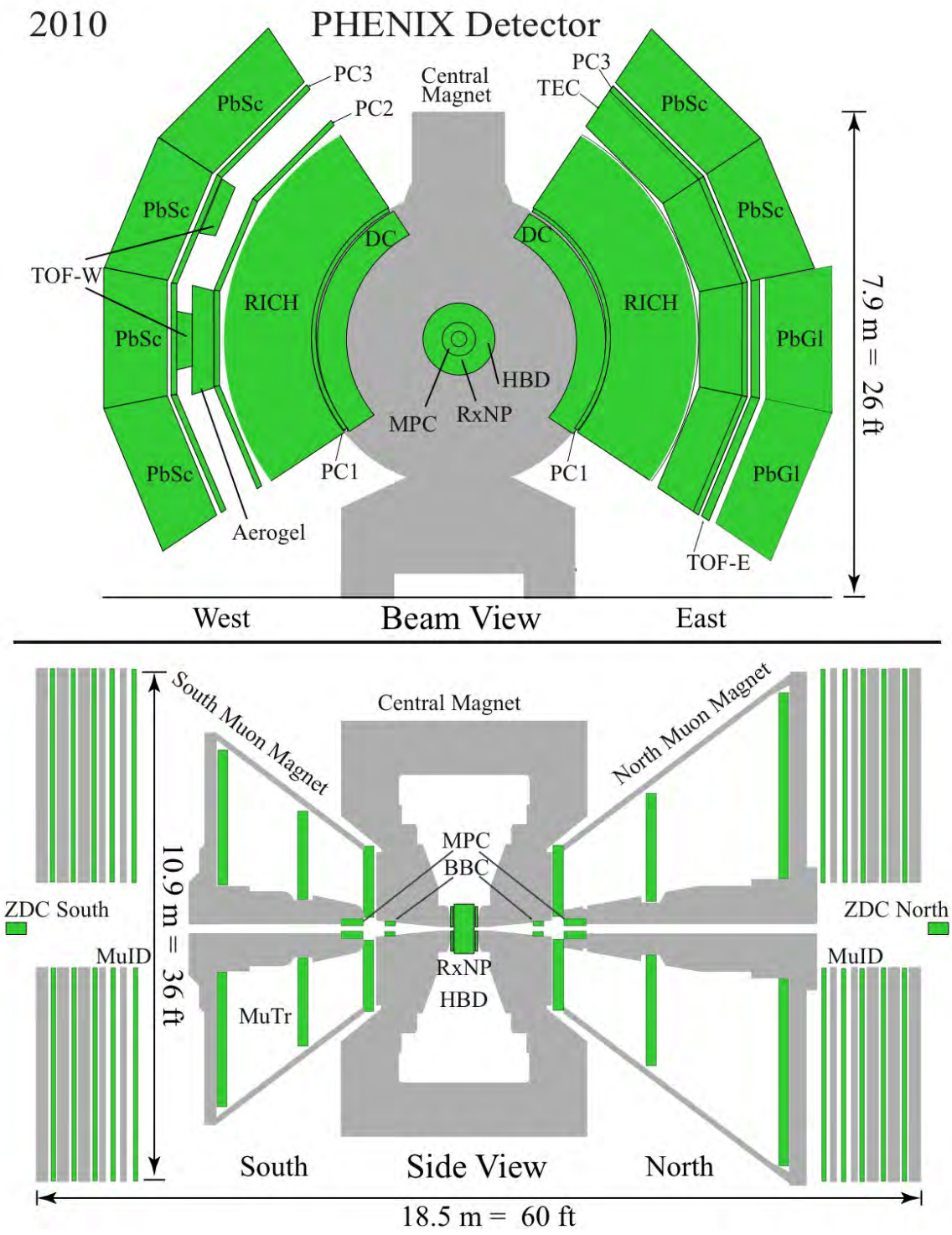

Figure 2.2: PHENIX detector configuration in Run-10. Top shows the PHENIX central arm from the beam view. Bottom shows the PHENIX muon arm from the east side view.

2.2.1 Global Detectors

Beam-Beam Counters

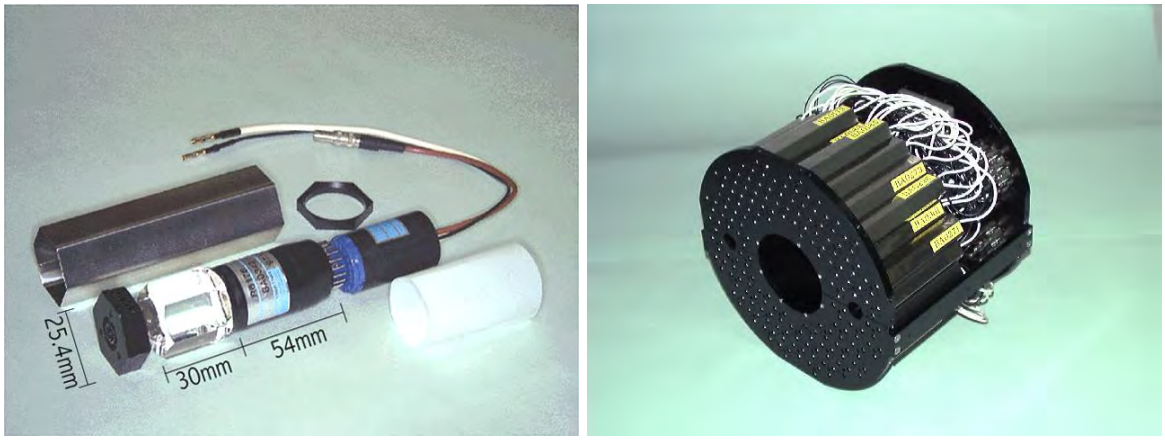

Figure 2.3: A single BBC element consisting of quartz Cherenkov radiator and meshed dynode PMT (left) and the BBC array with 64 elements (right) [34]

Two beam beam counters (BBC) are installed along the beam axis at 144 cm from the center of PHENIX with a rapidity coverage of $3.0 < |\eta| < 3.9$. The purpose of the BBC is to determine the collision position, the collision time, and the centrality of an event (determined together with the zero-degree calorimeter). The BBC also provides a minimum bias trigger. Each BBC counter has 64 one-inch mesh dynode photomultiplier tubes (PMT) and each PMT is equipped with 3 cm quartz on the head as a Cherenkov radiator(Fig. 2.3) [34]. Typical p + p collisions only produce a few tracks, but in central Au + Au collisions the number of tracks turns to be hundreds . Each PMT is capable of measuring 1 to 30 ionizing particles, which makes BBC efficient for most collision process as a minimum bias trigger.

The timing resolution of each PMT is 50 ps. The difference of the average hit time of PMTs between the north and the south BBC determines the collision vertex position along the beam direction. The vertex resolution is 1.2 cm in the beam direction in p + p collisions and 0.3 cm in Au + Au collisions.

Zero Degree Calorimeters

The zero degree calorimeters (ZDC) are hadron detectors located 18 m from the center of PHENIX along the beam axis [35]. ZDC measures neutrons from nucleus-nucleus collisions

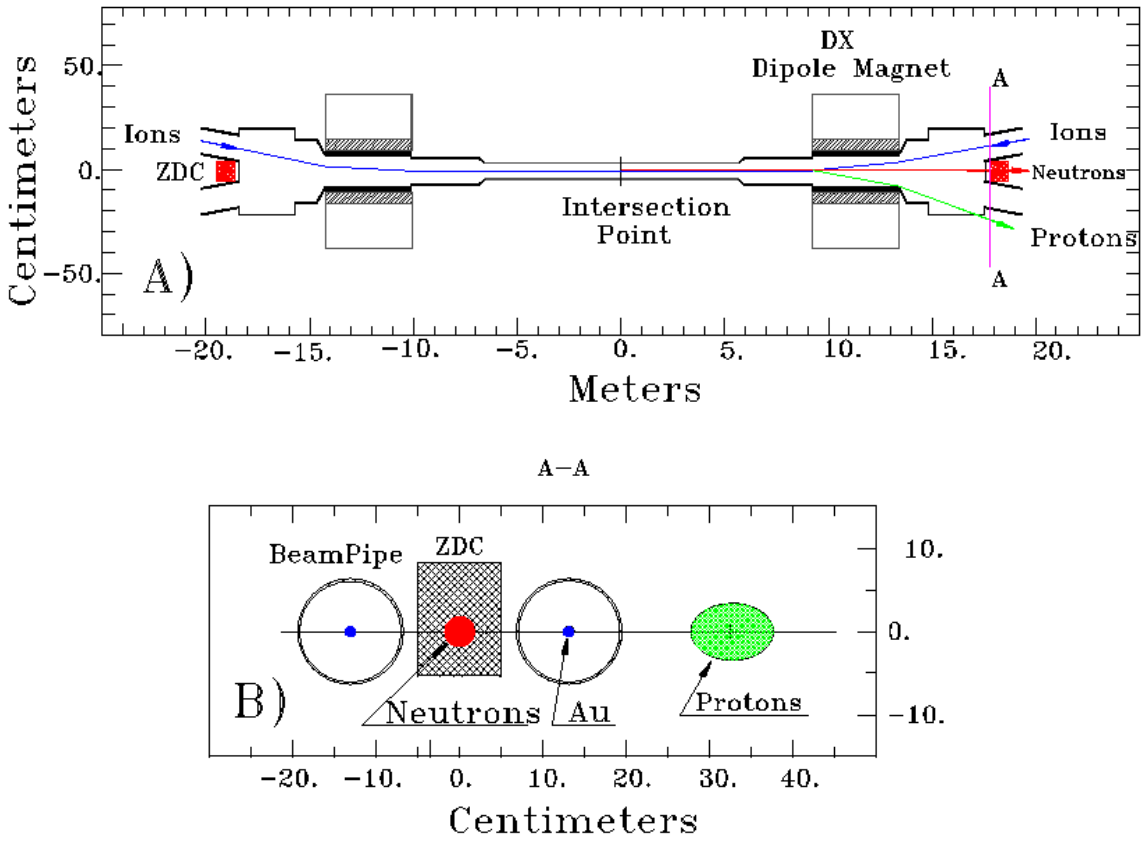

Figure 2.4: Position of ZDC along the beam pipe. The accelerate dipole magnets bent the charged particles, but leave the neutrons to enter the ZDC acceptance [35].

with the scattering angle less than 2 milli-radians. Fig 2.4 shows the position of the ZDC. Since ZDC is behind the accelerate dipole magnets, only neutrons can be detected while all charged particles are bent out of the ZDC acceptance. Each ZDC consists of 3 modules, and each module contains tungsten absorber plates. The neutrons lose energy in the plates and the signal can be detected in the photomultiplier tubes.

ZDC and BBC work together to determine the centrality of each collision. Fig 2.5 plots correlation between the energy measured in the ZDC and the total charge in the BBC. The centrality is determined in 5% centrality bins with equal number of events. The central events are the collisions with a large overlapping region of participating nuclei, and with a large number of produced particles and small number of spectator neutrons. Therefore, central events have high BBC response and low ZDC response. The ZDC is also used in the minimum bias trigger.

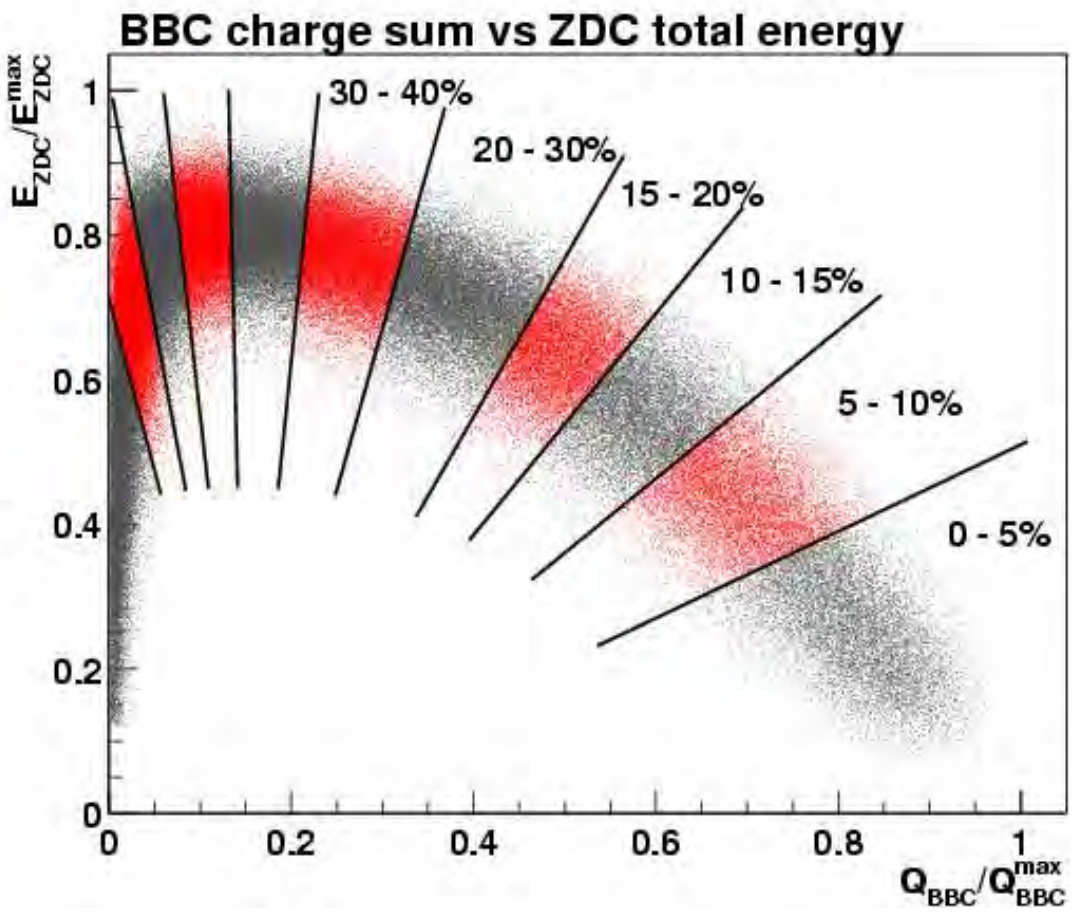

Figure 2.5: The total number of charge measured in BBC vs the the energy deposited in ZDC. The centrality is determined with equal number of events in each 5% centrality bin in this plot.

Reaction Plane Detector

The Reaction Plane Detector (RXNP) is a plastic scintillator paddle detector installed prior to Run-7. The purpose of the RXNP is to accurately measure the reaction plane (RP) angle, defined by the beam axis and the impact parameter of the collisions.

The RXNP is located at $\pm$ 39 cm along the beam pipe from the center of PHENIX with a set of 24 scintillators on each arm. A schematic view of scintillators is illustrated on the left pane of Fig. 2.6, where inner and outer layer of one RXNP arm are highlighted. The hole in the center of the arm represents the position of the beam pipe. The right part of Fig. 2.6 is a picture of the north arm of RXNP installed in PHENIX. Each arm covers a rapidity range

of $1.0 < |\eta| < 2.8$ and 2π in azimuthal angle. Each scintillator is embedded with fiber light guides on the surface every 0.5 cm and uses PMTs as readout. In the mid central Au + Au collisions at $\sqrt{s_{NN}} = 200$ GeV, the RP resolution of RXNP is 0.7, which is almost twice of the RP resolution measured by BBC before the RXNP installed. Better RP resolution of RXNP significantly enhanced accuracy of particle flow measurement in heavy ion collisions.

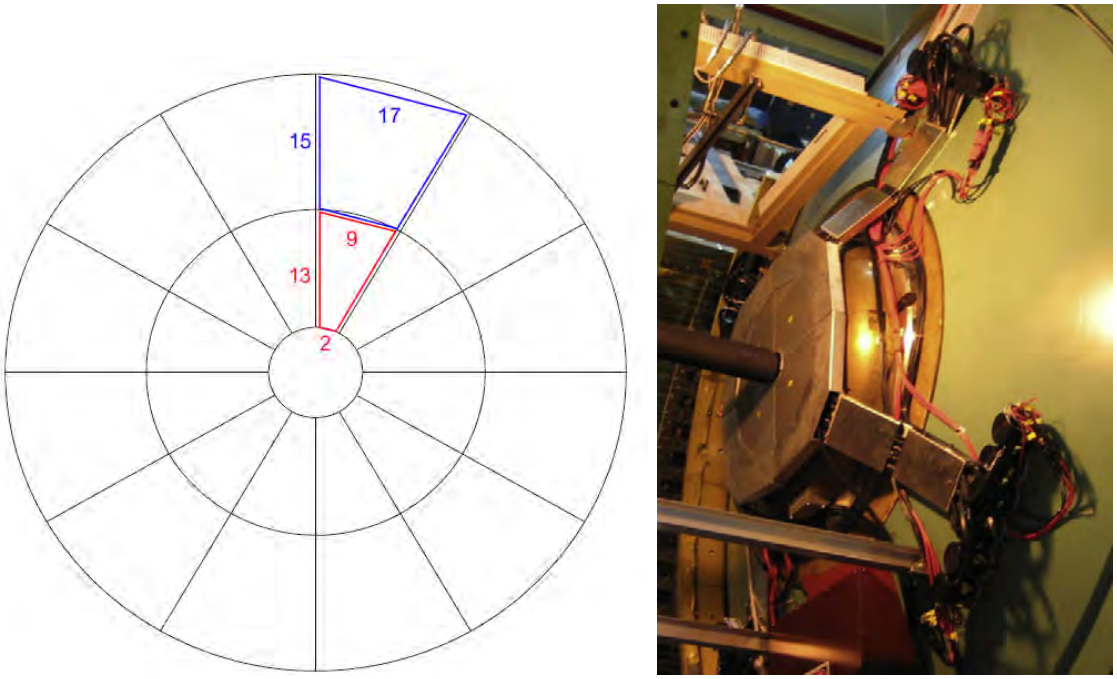

Figure 2.6: Schematic view of the arrangement of the 24 scintillators in one RXNP arm (left) and picture of the north arm of RXNP in the PHENIX interaction area (right) [36].

2.2.2 The Hadron Blind Detector

Many particles have e^+ or e^- decay channels. Electron pairs from π^0 Dalitz decays ($\pi^0 \rightarrow \gamma + e^+ + e^-$) or photon conversions ($\gamma \rightarrow e^+ + e^-$) account for the majority of background electrons. Electron pairs produced in both processes have small opening angles in the lab frame. The Hadron Blind Detector (HBD) is designed to separate close pairs (for example, electron pairs from π^0 Dalitz decay with small opening angle) from open pairs with large opening angle and single electrons.

The HBD is a windowless Cherenkov detector operated with a CF_4 radiator [37] [38]. It is installed in the PHENIX in Run-9 and Run-10 and successfully collected large amounts of

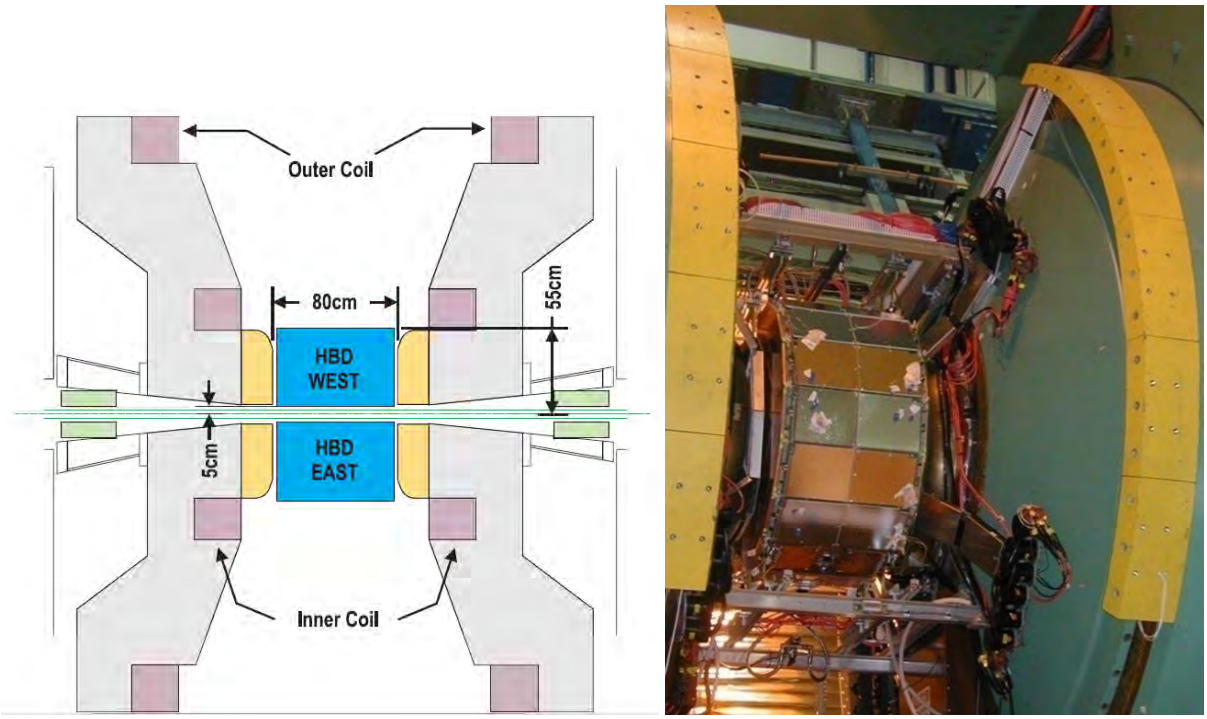

Figure 2.7: Location of the HBD detector (left) [38]. And a picture of the HBD west arm in the IR (right)

data in p + p and Au + Au collisions. Fig. 2.7 shows the position of the HBD and the central arm coils and a picture of the HBD west arm. The HBD was located before the inner coil of the central magnet. During its operation, the currents in the the inner and outer coils flow in opposite directions to create a field free region in the HBD area, which preserves the opening angle of electron pairs so that the HBD can identify and reject the close pairs.

CF_4 gas is used as the radiator and detector gas. The 50 cm long radiator is directly coupled in a windowless configuration to a readout element which consists of a triple gas electron multiplier (GEM) stack. A CsI photocathode is evaporated on the top surface of the top GEM, and a pad readout is located at the bottom of the stack [38], as seen in Fig. 2.8. When an electron traverses the HBD, it emits Cherenkov lights in the CF_4 gas. Photo-electrons are produced on the photosensitive CsI photocathode on the surface of the top GEM. The triple GEM stacks then amplifies and reads out the signal. By operating the detector with a reverse bias voltage, the ionization of the charged tracks are repelled to the opposite direction of the

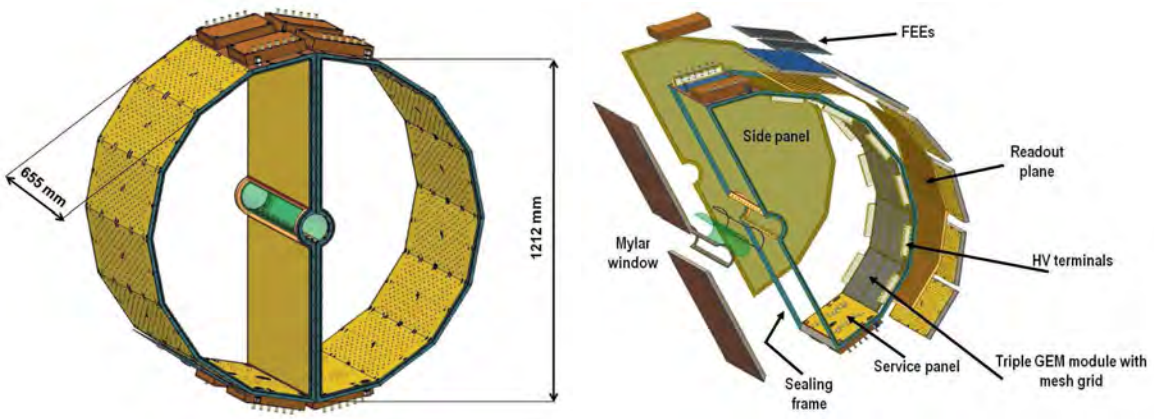

Figure 2.8: Design of the HBD detector [38].

first GEM. Therefore, the HBD is hadron-blind in the reverse bias mode (Fig. 2.9).

The size of the readout pad is 6.2 cm^2, which is same or smaller than the blob size of the Cherenkov lights (maximum area of 9.9 cm^2). The signal of a single electron is usually shared among 2 to 3 pads. Because of the large size and the low granularity of the pads, the signal of the electron pairs with small opening angles will overlap on a cluster of neighboring pads. Therefore close electron pairs can be separated from other electrons by the charge collected in HBD clusters. Electron pairs with mass $m_{ee} < 0.15 GeV/c$ measured in the PHENIX central arms are used to test HBD response. These low mass pairs are mostly from the π^0 Dalitz decay and photon conversions. The left plot in Fig. 2.10 is the charge collected in HBD from open pairs, which means each track in the pair is associated with different HBD clusters. The peak of the HBD response to open pairs (or single electrons) is around 20 photoelectrons (p.e.). For comparison, the right plot in Fig. 2.10 is the HBD response to double electron hits (close pairs) with two tracks from the same pair associated with the same HBD cluster. The peak of the HBD response to double electron hits is around 40 p.e.. For this analysis, the HBD plays an important role detector to reduce background electrons from π^0 Dalitz decays and photon conversions.

More information of HBD's specifications can be found in Table 2.1

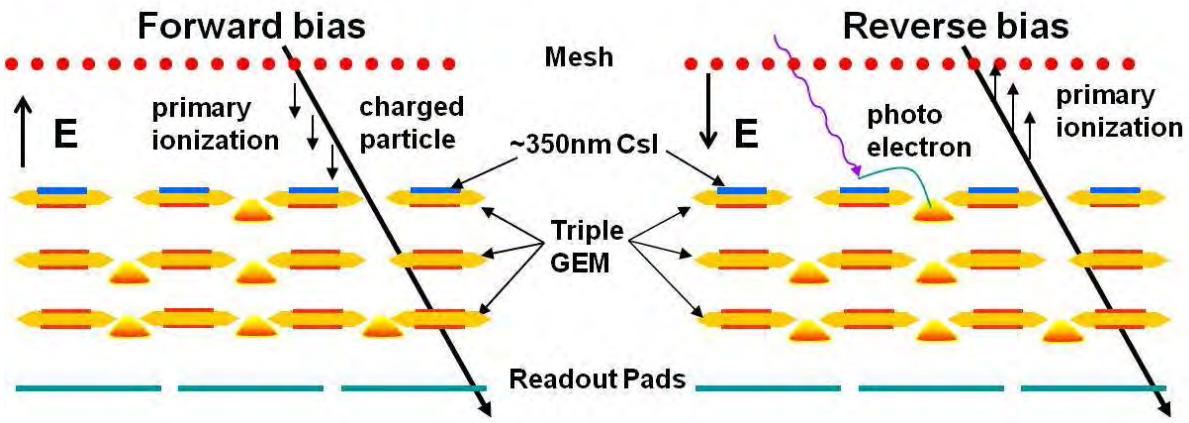

Figure 2.9: Comparison of signals received in the GEM with the standard forward bias voltage (left) and the reverse bias voltage (right). The HBD is hadron-blind when operating in the reverse bias mode [38].

Table 2.1: Design parameters of the HBD [38].

Acceptance	$\|\eta\| < 0.45, \delta\phi = 135^o$
GEM size ($\phi \times z$)	$23 \times 27 cm^2$
GEM supporting frame and cross (w × d)	frame: $5 \times 1.5 mm^2$, cross: $0.3 \times 1.5 mm^2$
Hexagonal pad side length	a = 15.5 mm
Number of pads per arm	1152
Dead area within central arm acceptance	7%
Total Radiation length within central arm acceptance	2.40%
Weight per arm (including HV and gas connectors)	< 10 kg

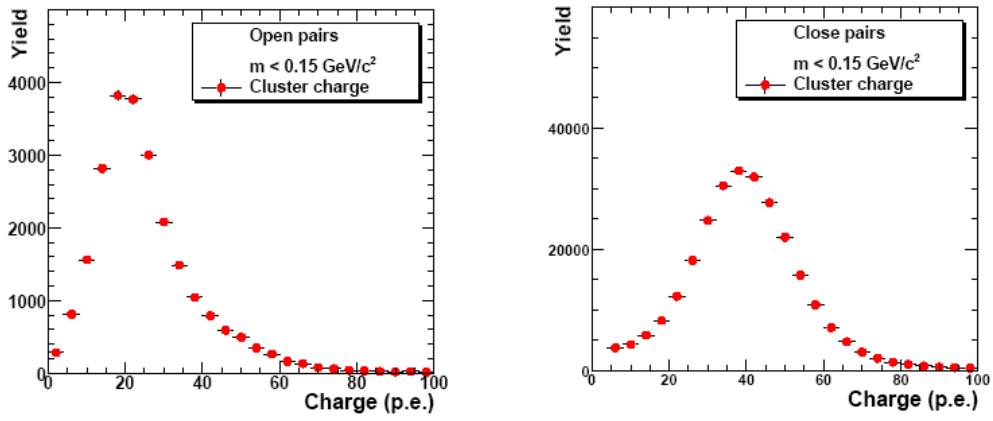

Figure 2.10: The HBD response to single (left) and double (right) electron hits [38].

2.2.3 Central Magnet

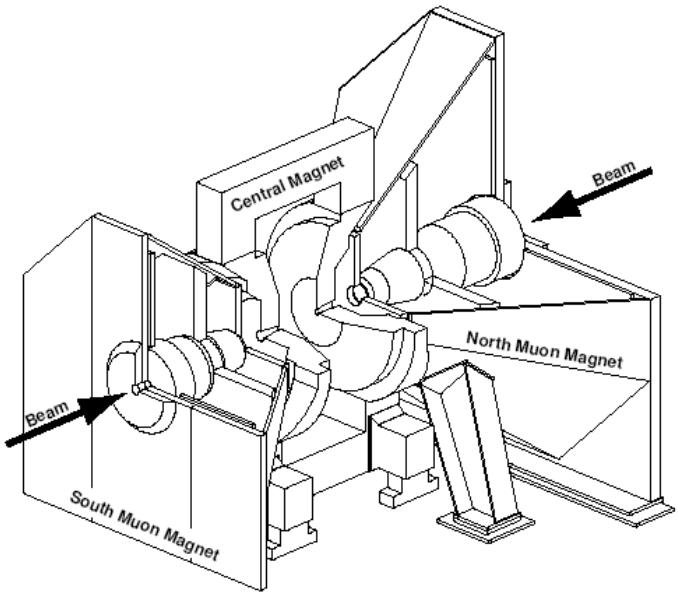

Figure 2.11: The PHENIX magnet subsystems.

There are three magnets in PHENIX: the central magnet, muon magnet south and muon magnet north, as shown in Fig. 2.11. The central magnet is 9 m tall with a weight of about 500 tons. It is energized by two pairs of concentric coils to provide an axial field with an integrated strength of 0.78 Tesla-meters at 90 degrees.

The central magnet in Run-10 run was operated in +- mode, which means the field generated by the two coils cancels within 50 cm from the center of the PHENIX in the radial direction. This configuration is required by the Hadron Blind Detector to identify electron pairs. The charged particles can still be bent by the magnetic field before entering the Drift Chamber for tracking.

2.2.4 Central Arm Detectors

This section only includes detectors that are designed to measure electrons in the central arm.

Drift Chamber

The Drift Chambers (DC), located between 2 to 2.4 m in radius from the center of the PHENIX and 2 m along the beam direction, are the main tracking detector in PHENIX. The coverage of each DC arm in azimuth is $\frac{\pi}{2}$. The DC work as multiwire chambers to measure the trajectories and determine the momenta of charged particles.

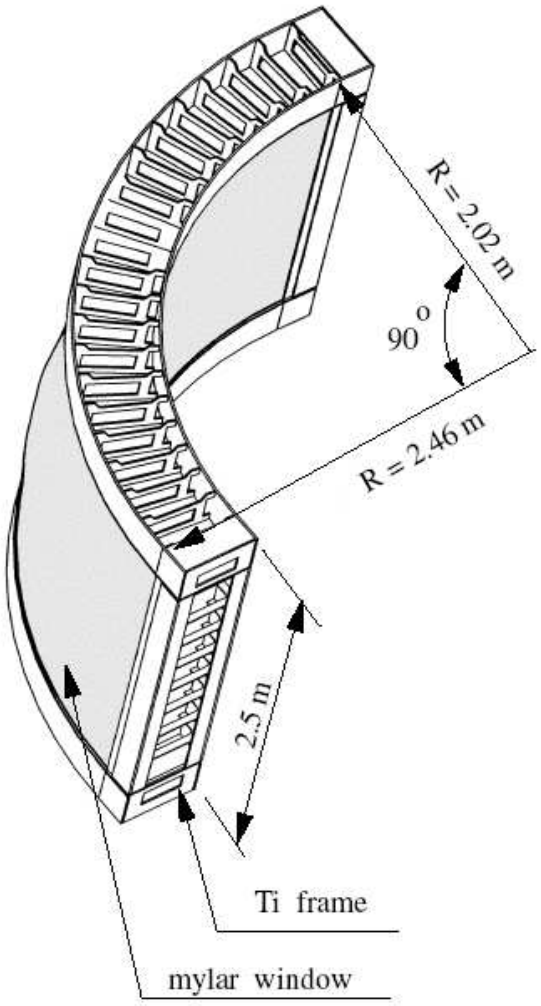

Figure 2.12: One arm of the Drift Chamber (DC) [39].

Each DC arm contains a cylindrically shaped titanium supporting frame and 20 keystones, as seen in Fig. 2.12. Each keystone contains six wire modules (X1, U1, V1, X2, U2 and V2). The X wires are parallel to the beam direction to measure trajectories of charged particles in

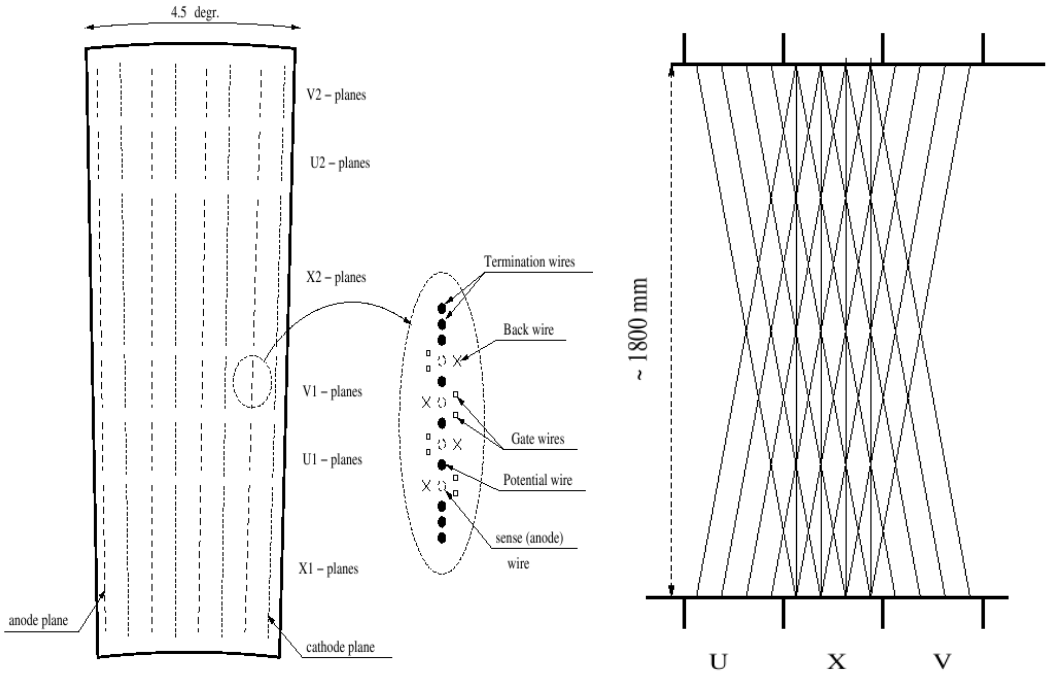

Figure 2.13: Structure of DC wires. [39].

the $r-\phi$ plane. The U, V wires are placed at a angle of 6^o with respect to the X wires in order to measure the z-coordinate (Fig. 2.13). A gas mixture of 50% argon and 50% ethane is filled in the DC active area. When a charged particle passes through DC, ionization in the gas is drifted towards the wires, then read out as a DC signal.

Pad Chambers

The Pad Chambers (PC), which are multiwire proportional chambers, are also an important part of the PHENIX central tracking system. The PHENIX cental arm contains 3 layers of PC. The first layer (PC1) is installed behind the DC to provide the information of the z coordinate of the track. The second layer (PC2) is only installed behind the RICH detector in the west arm. The third layer (PC3) are located in front of the EMCal in both arms to provide additional tracking information for the tracks which enter the EMCal. Fig 2.14 shows a schematic view of the three PC layers.

Each PC contains a single plane of wires inside a gas volume bounded by two cathode planes [39]. Each cathode consists of an array of pixels. When a charged particle ionizes in the gas

in PC and cause an avalanche on anode wires, the image charge induced on the pixel cathodes is read out to measure the straight trajectory of the charged particle. The resolution of PC is 1.7 mm in the z direction and 2.5 mm in the $r - \phi$ plane.

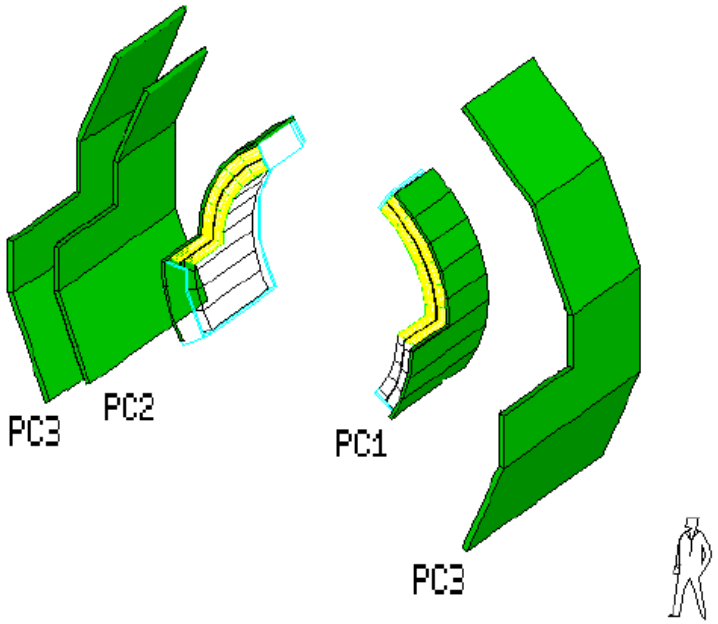

Figure 2.14: Schematic view of three PC layers [40].

Ring Imaging Cherenkov Counter

The Ring Imaging Cherenkov Counter (RICH) installed on each of the PHENIX central arms is the primary detector for electron identification and electron-pion separation. Located at r= 2.575 to 4.1 m from the beam pipe, the RICH detector is a threshold gas Cherenkov detector with a high angular segmentation to cope with the high particle density, at about 1000 charged particles per unit rapidity, expected in collisions with the highest muliplicities at RHIC [42]. CO_2 gas is filled in the radiator which allows relativistic electrons to emit Cherenkov light. Charged pions with p_T larger than 4.9 GeV/c also radiate in the CO_2 gas, which makes the electron-pion separation only possible for $p_T < 4.9 GeV/c$.

Fig. 2.15 shows the cutaway view and the cut through view of the RICH detector. When an electron or high p_T charged pion emits Cherenkov light in the gas, the light is reflected by

the spherical mirror onto two 16×80 arrays of PMTs. The angular resolution of the PMT is $1^o \times 1^o$ in θ and ϕ

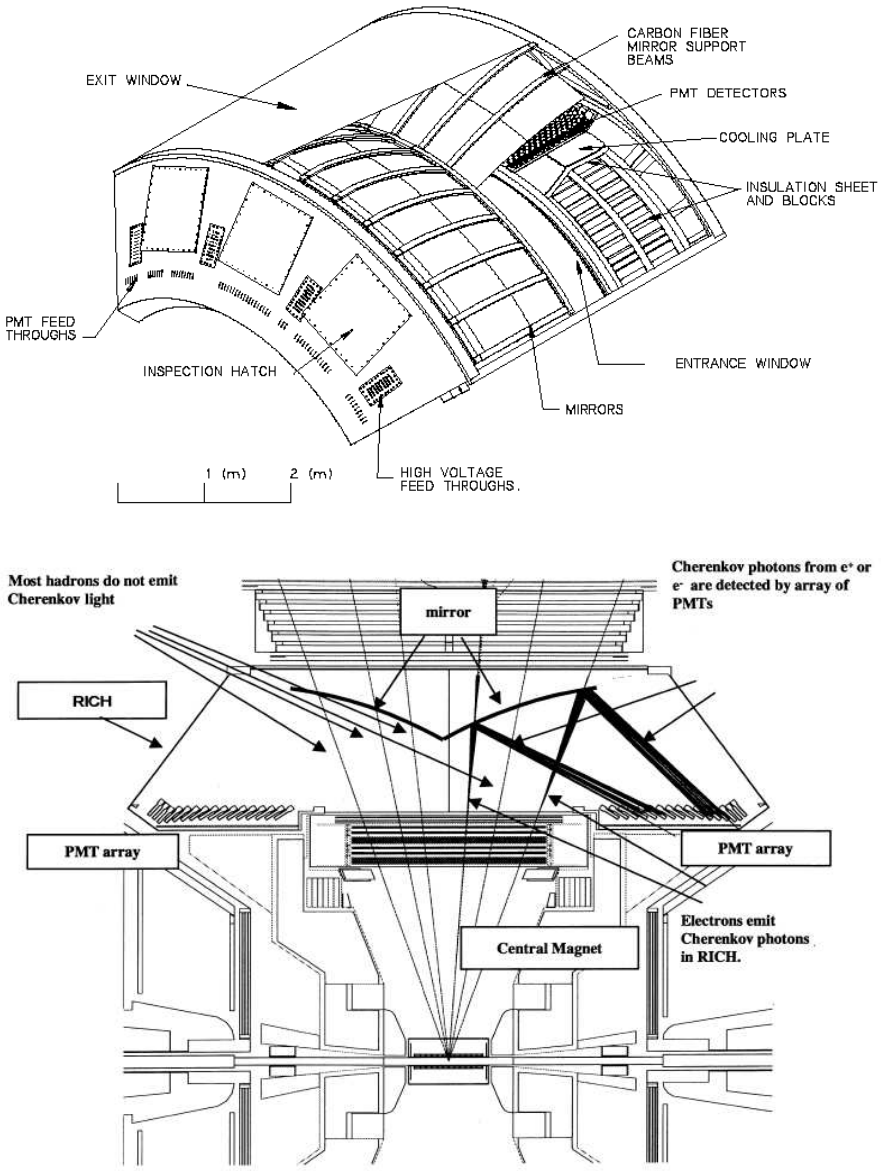

Figure 2.15: Structure and design of RICH [41] [42].

Electromagnetic Calorimeters

The Electromagnetic Calorimeter (EMCal), the outermost detector in the PHENIX central arm, is designed to provide the energy and spatial position of electrons and photons. The coverage of each EMCal arm is $70^o < \theta < 110^o$ and $\frac{\pi}{2}$ in ϕ. The four EMCal sections in the west arm are all lead scintillator calorimeters (PbSc), while the four sections in the east arm consist of two lead scintillator calorimeters and two lead glass Cherenkov calorimeters (PbGL).

The PbSc is a shashlik type sampling calorimeter made of alternating tiles of Pb and scintillator consisting of 15552 individual towers and covering an area of approximately 48 m^2 [43]. The energy resolution of the PbSc is $8.1\%/\sqrt{E} \bigoplus 2.1\%$, while the timing resolution is 200 ps or better for electromagnetic showers.

The PbGL contains 9216 elements and were used in the WA98 experiment in CERN before. The energy resolution of the PbGl is $6\%/\sqrt{E}$, and the timing resolution is better than 300 ps.

Fig. 2.16 shows the structure of the lead scintillator module and the lead glass module. More details can be found in [43].

The total depth of PbSc and PbGL is 18 and 14.4 radiation length. As shown in Fig. 2.17, the energy deposit in EMCal for electrons, protons and pions are different, which allow us to separate electrons and pions with the energy to momentum ratio.

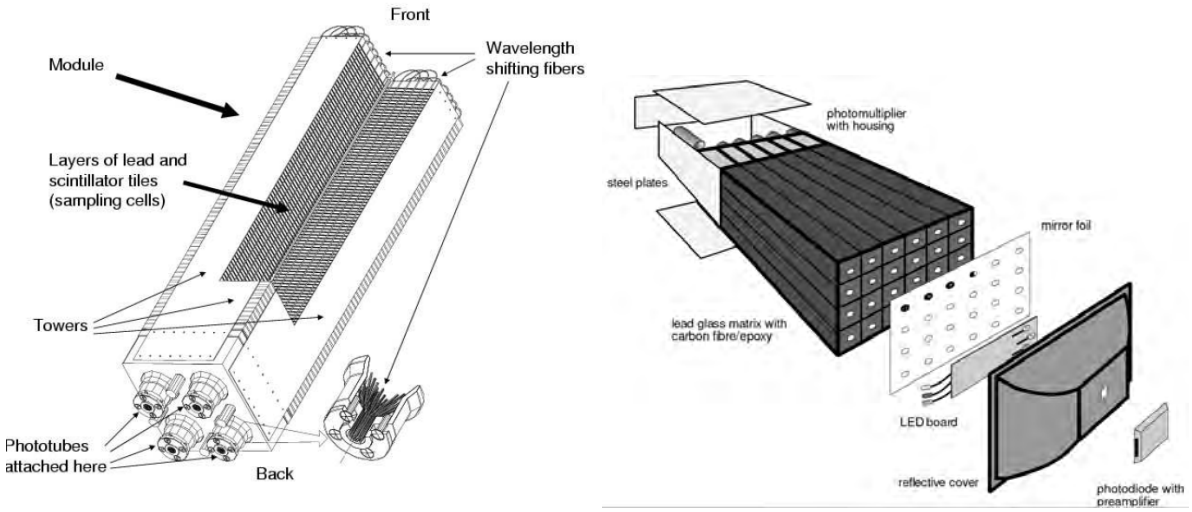

Figure 2.16: Interior view of a lead scintillator module (left) and exploded view of a lead glass module (right) [43].

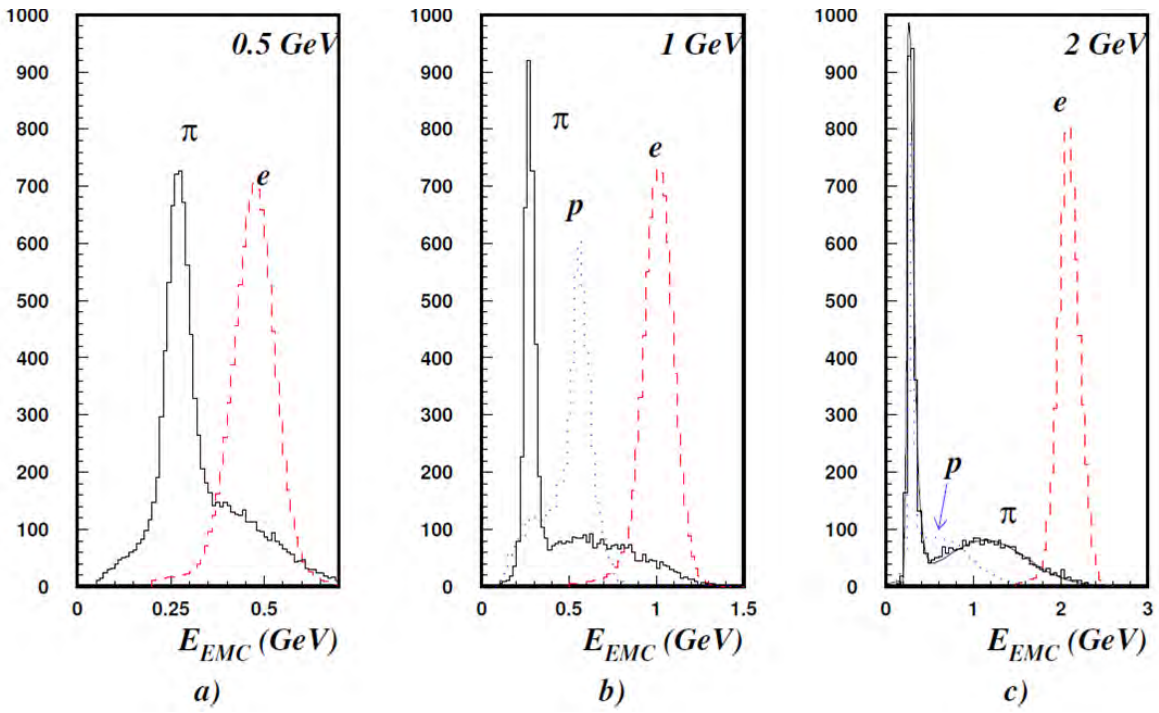

Figure 2.17: The energy distribution in EMCal for electrons, protons and pions with p_T at 0.5, 1, 2 GeV/c [43].

CHAPTER 3. MEASUREMENT OF INCLUSIVE ELECTRON SPECTRUM AND FLOW

This chapter describes the measurement of inclusive electrons spectrum and v_2 using data taken by PHENIX detectors during the 2010 RHIC run period. The collision system is Au+Au collisions at $\sqrt{s_{NN}} = 62.4$ GeV.

3.1 Run Selection

PHENIX data are recorded in runs which contain a large number of events (collisions) that were collected between a successive start and end issued by PHENIX data acquisition system (DAQ). Each PHENIX run is assigned a unique run number. The run number for Au + Au collisions at 62.4 GeV ranged from 313472 to 314994. The operating conditions for each run may be different due to changing detector dead areas, unstable DAQ conditions and etc., all of which can cause fluctuations in the electron yield per event in a given run. Therefore, to make sure the PHENIX detectors have stable performance and our data have good quality, run-by-run quality checks are necessary before we select our electron samples.

An important quality check is the average number of electrons or positrons per event in each run. A set of tracking and particle identification cuts, as shown in Table 3.1 is applied to the data to select electron or position candidates in each run. We will discuss the details of each cut in Section 3.2 and 3.3. The average number of electrons or positrons per event is the total number of electrons or positrons divided by the number of events in the run.

The average number of electrons or positions per event is plotted as a function of run number (Fig. 3.1). Runs with too high or too low average number of electrons or positions per event will not be considered in this analysis. We calculate the mean average number per

run and the one-sigma RMS value. If the average number of electrons in a run is more than 3 sigma away from the mean value, this run is marked as a bad run. 4 runs are excluded in our analysis. They are: 311979,312371,312483,312825

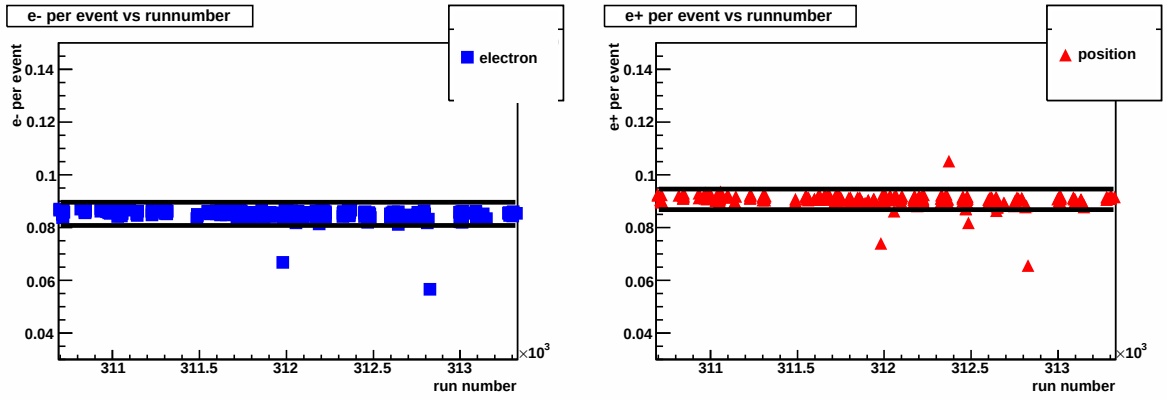

Figure 3.1: number of electron (positron) per event (left is electron ratio vs run number and right is positron ratio vs run number. Black lines are 3 sigma away from the center. 4 runs are outside the 3 sigma region)

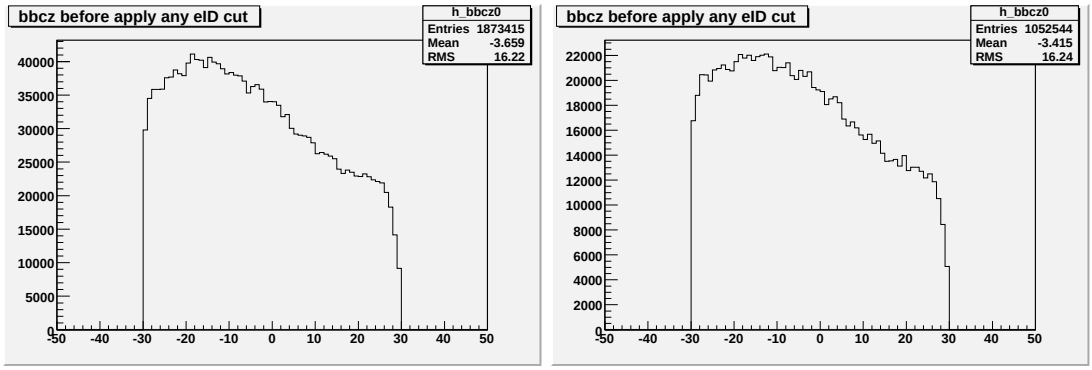

(a) run311990 (b) run311991

Figure 3.2: This is the bbcz distribution of run 311990 and run311991.The x axis is bbcz and the y axis is the count N.

Additional run quality measures are the distribution of the collision vertex in z direction measured by BBC (bbcz) and centrality distribution. Run 311990 and Run 311991 have non-flat bbcz distribution as shown in Fig. 3.2. Run 312891 has a non-flat centrality distribution. These runs are also excluded in the analysis.

3.2 Event Selection

In PHENIX, not every event is recorded since the real collision rate is usually much higher than the data acquisition bandwidth. PHENIX only records the events that satisfy one or more triggers. The minimum bias (MB) trigger, which is the basic and least selective trigger, is used in this analysis.

The Au+Au MB is defined by Eq. 3.1, requires at least one hit on each side of BBC.

$$MinimumBias \equiv "BBCLL1(>0tubes)" or "BBCLL1(>0tubes)novertex" \tag{3.1}$$

The events analyzed in this analysis are also required to pass the bbcz cut: $\mid bbcz \mid \leq 20$ cm. bbcz (or z-vertex) is the z position of the collision vertex. It is calculated from the timing differences between north and south sides of the BBC. This cut is determined by plotting the average number of electrons or positrons per event vs z-vertex. Fig. 3.3 shows that for collision vertexes within $\pm$ 20 cm, the distribution of electron or positron per event is approximately flat. This z-vertex cut helps us to remove collisions that happened far away from the center of the PHENIX detector.

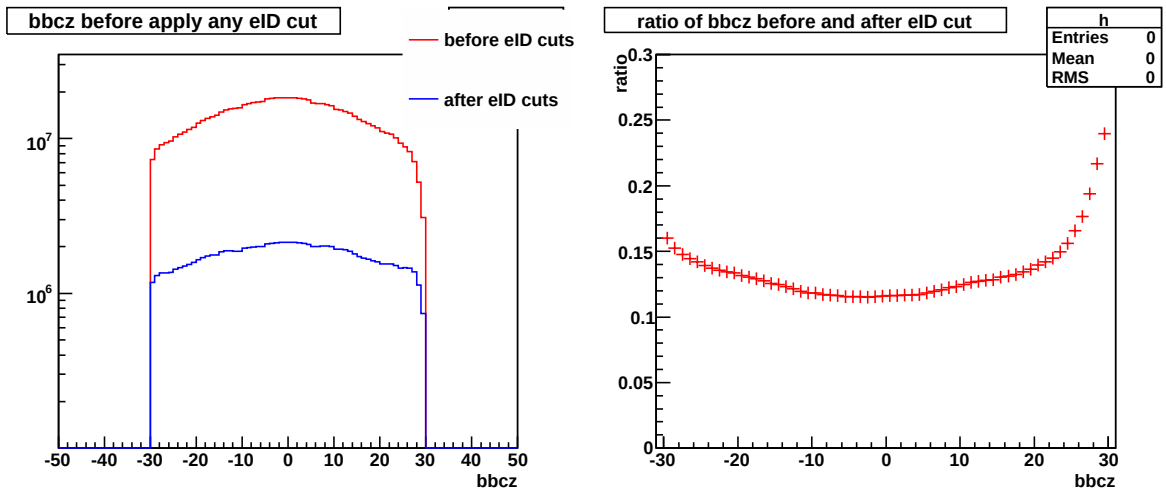

Figure 3.3: Left plot is the bbcz distribution with/without eID cuts; Right plot is electrons per event, i.e. the ratio between two left plots, vs bbcz

3.3 Track Selection

In this section, we will discuss how to select good-quality electron candidate tracks using the information from the detectors described in Chapter 2.

Charged tracks are reconstructed by the DC and PCs. The RICH and EMCal are the main detectors for electron identification (eID). As we mentioned in Chapter 2, the HBD is installed in PHENIX in Run-10 increasing our ability for eID and background rejection.

3.3.1 Electron Identification using Central Arm

The following Central Arm (CA) variables are used for track selection and electron identification:

- **quality**: the associated bit pattern indicating the number of DC and PC hits for each track. This analysis requires tracks to have hits in X1, X2 sections, be uniquely associated with UV hits and have at least one PC1 hit (quality = 31 or 63);
- **n0**: the number of phototubes fired in the RICH detector in a normal- sized ring around the track projection. The inner radius of the ring is 3.4 cm and the outer radius is 8.4 cm, with the expected radius of the Cerenkov ring from electron emission being 5.8 cm;
- **disp**: the displacement of the ring center with respect to the track projection in cm;
- **emcsdphi**: the displacement in ϕ direction between the track projection and the associated EMCal hit. This displacement is normalized by the variance of the distribution, i.e. is available as the number of sigma away from zero;
- **emcsdz**: the displacement in z direction between the track projection and the associated EMCal hit, again is normalized by the variance of the distribution;
- **prob**: the probability that the shower measured in EMCal is electromagnetic;
- E/p: the ratio of energy deposited in EMCal and momentum reconstructed in DC. Since $E = \sqrt{m^2 + p^2}$, a electron deposits most of its energy in the EMCal, the E/p distribution of electrons is a Gaussian distribution centered around 1. On the other hand, a hadron

does not deposit all of its energy and has a large mass, hence the E/p of hadrons is smaller than 1. The standard deviation of the E/p distribution ($\sigma_{E/p}$) depends on particle p_T;

- **dep**: dep is calculated as $dep = \frac{E/p-1}{\sigma_{E/p}}$. The dep distribution of electrons should be a standard Gaussian distribution centered at 0 with width = 1.

For low momentum tracks ($p_T < 4.8GeV/c$), only electrons can fire RICH. Hence cuts of $n_0 > 3 \&\& disp < 5$ are applied to data to select electron candidates. For a track with $p_T > 4.8GeV/c$, charged hadrons, especially pions, also have a chance to fire RICH. However, because of limited statistics, there are very few tracks with $p_T > 4.8GeV/c$, therefore, we will use the same n_0 cut for the whole p_T range.

Although the RICH cuts can efficiently remove most of the hadron tracks, there are still some hadron tracks can pass the RICH cuts by accidentally associating with a Cerenkov ring in the RICH detector. This ring is produced by another particle. Therefore, EMCal matching, $prob > 0.02$ and $dep > -2$ are also required for an electron candidate. $prob > 0.02$ cut can reject a large fraction of hadrons and keep 98% efficiency for an electron or photon shower. $dep > -2$ also helps to remove hadrons with a small E/p.

To summary, the CA eID cuts used in this analysis are listed in Table 3.1

Table 3.1: Track selection and eID cuts used in run selection and data analysis

Variable	**Cuts**
p_T	> 0.2 GeV/c
$quality$	$= 31 or 63$
n_0	> 3
$disp$	< 5
$\sqrt{emcsdphi^2 + emcsdz^2}$	< 3
$prob$	> 0.02
dep	> -2

3.3.2 HBD Charge Cut

In additional to CA eID cuts, the HBD can also be used for electron identification and background rejection.

The HBD is a Cerenkov detector designed to separate electron pairs from Dalitz decays and single electrons. The HBD variable used to remove background is called hbdq, which is the number of photoelectrons (n.p.e.) recorded by HBD in a cluaster. If a track associates with a HBD cluster, there are three possible cases:

1. The track is a single electron or an electron from a so called open electron pair. It emits Cerenkov light and a mean number of 20 photoelectrons is recorded by HBD. Hbdq distribution is a Gaussian-like distribution centered at 20 n.p.e.

2. The track is an electron or a positron from a close electron pair from Dalitz decays or photon conversions with small opening angle. Both the electron and the positron emit Cerenkov light and the HBD clusters are merged. A mean number of 40 photoelectrons are associated with the track. Hbdq distribution is a Gaussian-like distribution centered at 40 n.p.e.

3. The track does not fire HBD itself but is randomly associated with an existing HBD cluster due to the high multiplicity. The track can be either a hadron or an electron from photon conversions which happen at the HBD backplane. The hbdq distribution has low value and is exponential-like distribution.

In this analysis, the single electrons from heavy flavor meson decays which correspond to case 1 are our signal, while tracks from case 2 and case 3 are background. Hence $hbdq < 35$ is used to reduce tracks from close Dalitz decay electron pairs (case 2). $hbdq > 10$ is used to reduce tracks from random association (case 3). Notice that since the HBD is in front of the Central Arm, electrons from photon conversions at HBD backplane pass all the CA eID cuts but can only be rejected by the HBD cut. Approximately, almost 90 % of our electron candidates that passed all regular CA eID cuts are electrons from HBD backplane conversion.

The HBD cut used in this analysis is:

- $10 < hbdq < 35$

This hbdq cut removes more than 90% of the background from HBD backplane or PHENIX Central Arm and keeps 65% of the electron signal in the most central events.

3.4 Fiducial Cuts

The fiducial cuts are used to remove the inefficient acceptance area in the detector and to ensure that both the real data and the Monte Carlo simulation have the same stable active area. Fiducial cuts are very important for us to get the accurate acceptance correction factor and measure the invariant yield of electrons.

The basic fiducial cuts is:

- $|zed| < 75cm$

Where zed is the z coordinate of the track in DC at a reference radius of 2 m. This cut removes the inefficient area in DC.

More fiducial cuts are made to match the detector live area in the simulation to the real data. For example, if one channel in DC was dead during data taking but it may not be marked as dead in the Monte Carlo simulation of the detector, to match the simulation with the real data, we can use the fiducial cuts to mark this channel and apply the cuts to both the data analysis and the simulation. Distributions of bbcz vs $\cos(\theta_0)$ and DC variables are studied in both the data and the simulation. After applying the fiducial cuts, the variable distributions in the data and the simulation show a good agreement, which indicates that the fiducial cuts successfully removes inefficient area in both data and simulation. More details will be shown in Fig. 3.7 and Fig. 3.9 in Section 3.6.1

3.5 Background Subtraction and HBD Swapping Method

There may still be some hadron tracks left in our sample. Because of the high multiplicity in Au + Au collisions, even at 62.4 GeV, almost the whole HBD detector recorded signals. Hence conversion electrons produced at HBD backplane can randomly match with a cluster in HBD and pass all eID cuts, even the hbdq cut. The swapping method can be used to statistically remove the remaining background due to random association.

HBD swapped variables are obtained by randomly matching a Central Arm track to the opposite side of HBD detector in the software, i.e. swapping between east and west sides of the HBD. Then we apply the same HBD cut but with the swapped variables to data. Because any

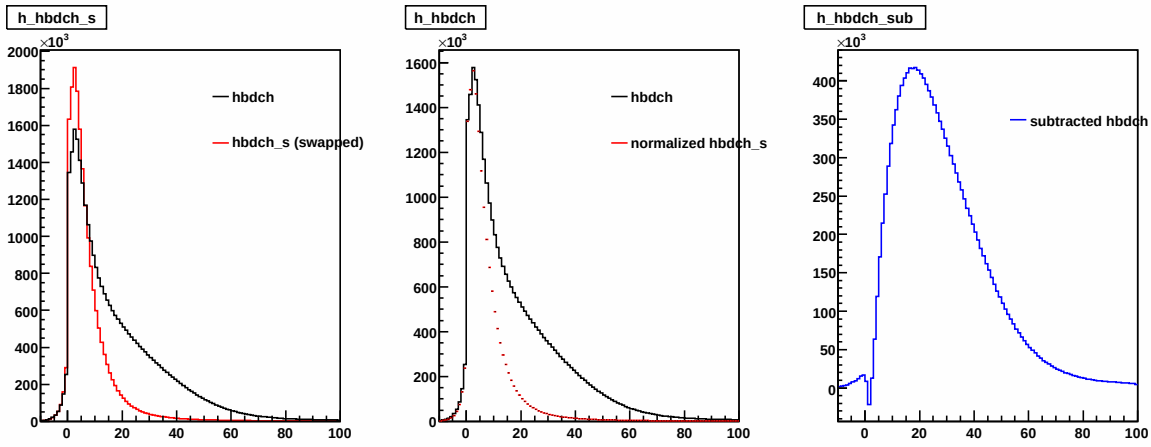

Figure 3.4: These plots show hbdq distribution (MB data). The black line is hbdq, the red line is the swapped hbdq and the blue line is the subtracted hbdq. The left plot is the distribution from data. The middle plot shows how to scale swapped hbdq. The right plot is the hbdq after subtraction.

electron candidates that pass the swapped hbdq cut are from random matching, this provides us a statistical estimate of how many electrons which pass the regular hbdq cut are from randomly matching in the HBD detector. The electron candidates that pass the swapped HBD cut are statistically subtracted from the electron candidates that pass the regular cuts. In Fig. 3.4, the left plot shows the hbdq and swapped hbdq distribution in MB data. At very low hbdq, there are more swapped hbdq tracks than regular hbdq tracks, that is because of the electrons generated before HBD. Therefore, before subtracting swapped hbdq, we scale the swapped hbdq distribution down to match the distribution of the regular hbdq at the very low charge. This is shown in the middle plpt of Fig. 3.4. The right plot of Fig. 3.4 is the hbdq distribution after the statistical subtraction of the swapping method. We can clearly see the peak around 20 for single electrons and electrons from open Dalitz decays. Fig. 3.5 shows the regular hbdq, swapped hbdq and subtracted hbdq distribution for different p_T range.

The swapped hbd cut is:

- $10 < hbdq_s < 35$

After applying all the cuts discussed in Section 3.3 and 3.5, we examine the shape of the E/p distribution to make sure no hadron background are left in the sample.

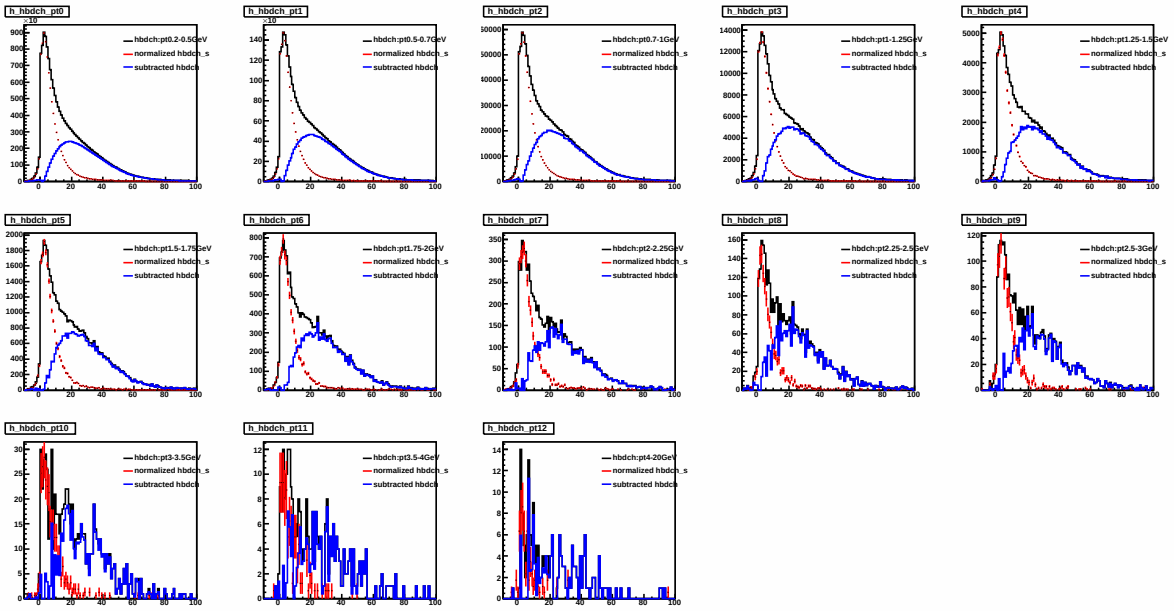

Figure 3.5: These plots show hbdq distribution (MB data) for different p_T range. The black line is hbdq, the red line is the swapped hbdq and the blue line is the subtracted hbdq.

Fig. 3.6 shows the E/p distribution at different p_T range: $0.5-0.7, 0.7-1, 1-1.5, 1.5-2, 2-3, >3 (GeV/c)$. All the cuts we discussed above are applied except the dep cut. The E/p distribution is fitted with a Gaussian + exponential function. The hadron background part is estimated by the exponential function, while the Gaussian function can describe electrons generated near the collision vertex. From this figure, the exponential part is negligible within 2 sigma of the Gaussian distribution, which shows that our cuts can remove hadron background efficiently.

3.6 Acceptance and Efficiency Corrections

The electrons reconstructed by PHENIX Central Arms and selected by our cuts are not all the electrons produced in the Au+Au collisions because PHENIX Central Arms only cover half of the azimuth, ± 0.35 in rapidity, and we also lose efficiency when applying any cuts. Without correcting for these acceptance and efficiency loss, it is difficult to compare our results with other experiments or theoretical calculation. One important variable we measure is the invariant yield

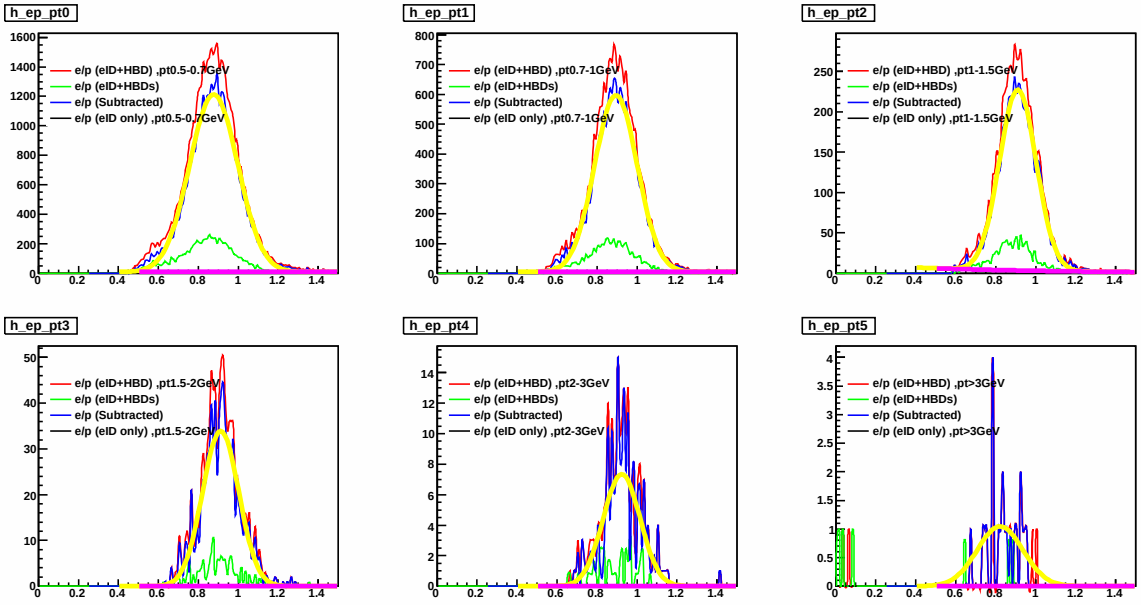

Figure 3.6: E/p distribution for different p_T range (with HBD regular cuts(red), with HBD swapped cuts(green) and subtracted(blue), The subtracted E/p distribution is fitted with Gaussian (yellow curve) + exponential (magenta curve) function.

of electrons (Eq. 3.2), which can be compared directly between different particles or different experiments. To obtain it, all the acceptance and efficiency effects need to be corrected.

$$E\frac{d^3N}{d^3p} = \frac{cd^2N}{2\pi p_T dp_T dy} \tag{3.2}$$

The general way to calculate these corrections is to randomly generate large amount of electrons or positrons in simulation, then let all the particles run through a GEANT based PHENIX detector simulation called PISA to simulate the detector response, finally use the same software to reconstruct simulated tracks and apply the identical cuts used in data analysis to select electron candidates. The comparison between the input simulated particles and the output tracks tells us how many percent of particles is lost in our analysis due to the detector coverage or cut efficiency.

3.6.1 Central Arm Single Track Acceptance and Efficiency

For a single track, the efficiency loss in the Central Arm comes from three parts:

1. Geometric loss ϵ^{geo} represents the fraction of particles that do not hit the detector's live area due to the finite coverage of the detectors.

2. Reconstruction efficiency ϵ^{rec} accounts for the difference between the measured particle spectra and the real spectra caused by the track reconstruction algorithm.

3. eID cuts efficiency ϵ^{eID} accounts for the signal loss by applying all the eID cuts.

In order to obtain the CA efficiency correction for single tracks, 5 million single electrons and 5 million single positrons were generated randomly with the following conditions:

- flat p_T distribution from 0 to 10 GeV/c;
- flat rapidity distribution in $-0.5 < \eta < 0.5$;
- flat bbcz distribution within $\pm$30cm;
- flat azimuthal angle ϕ from 0 to 2π;

A flat p_T distribution is used to generate single particles to get reasonable statistics at high p_T. All simulated particles are weighted by a realistic p_T function to correctly account for the p_T smearing and any p_T dependent effects in real data. The rapidity $-0.5 < \eta < 0.5$ and azimuthal angle $0 < \phi < 2\pi$ are greater than the CA coverage make it easy to correct the raw data to 2π in azimuth and 1 unit in rapidity.

All the simulated electrons and positrons are run through the whole PISA and reconstruction chain. All cuts in Table 3.1 are used to select tracks. Because we calculate HBD efficiency separately, the HBD cut is not applied to the simulated tracks.

To accurately account for the geometric loss, the active area of the detectors in simulation must be same as the actual active area of the detectors during data taking. The same detector live channel maps and fiducial cuts are used for both simulation and data analysis. Fig. 3.7 – Fig. 3.11 shows that the detector live area in simulation matches the real data.

The simulated distributions of all the variables used in our cuts are also compared to the measured distributions in real data. (Fig. 3.11). The simulation of n_0 and prob (Fig. 3.11(a) and Fig. 3.11(d)) don't match with data perfectly. Other variables show good matching

between simulation and real data, especially within the eID cuts. The remaining hadron contamination in the electron sample may be the reason for the difference between the simulation and actual measurement of n0 and prob. The systematic error from the imperfect modelling of our detectors in PISA will be calculated later by varying our eID cuts in Chapter 5.

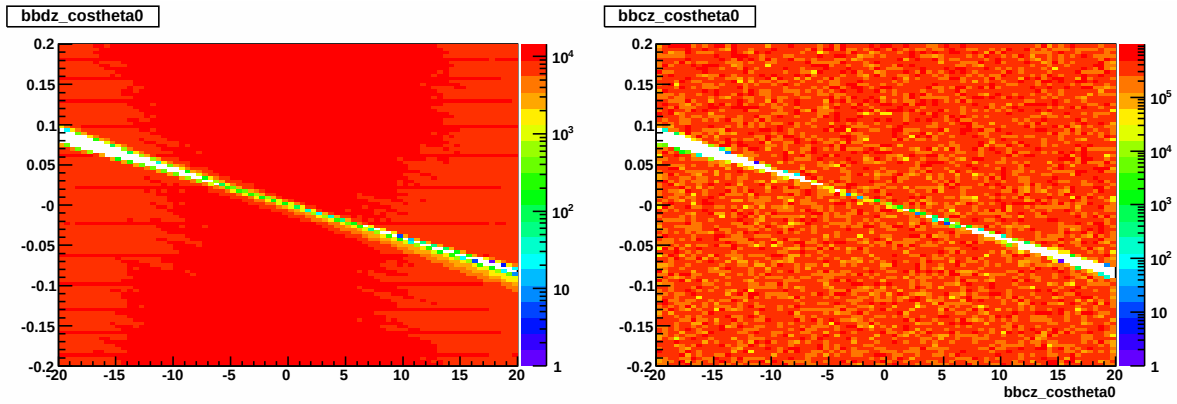

Figure 3.7: bbcz vs $\cos(\theta_0)$ in data (left plot) and simulation (right plot)

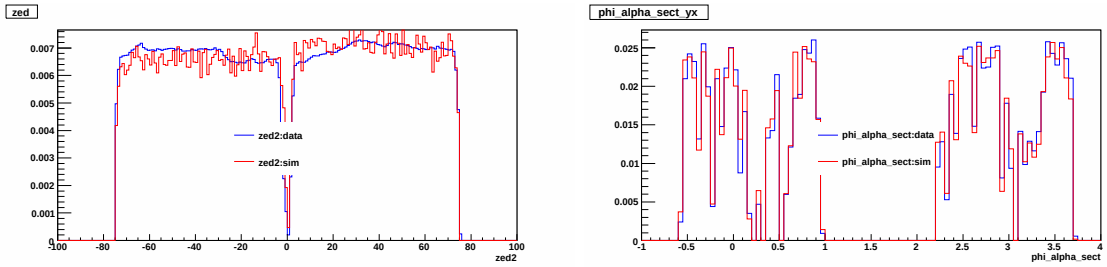

(a) zed (b) phi

Figure 3.8: zed and phi in data and simulation

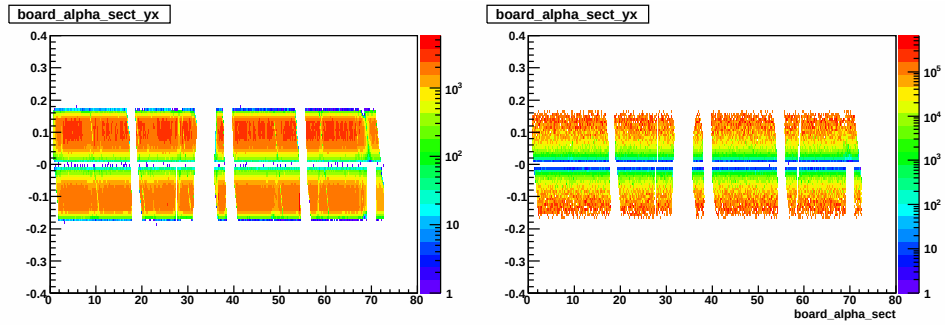

(a) sector 0

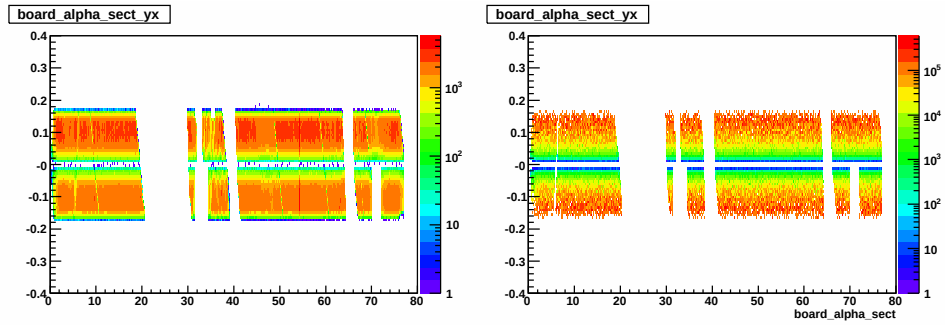

(b) sector 1

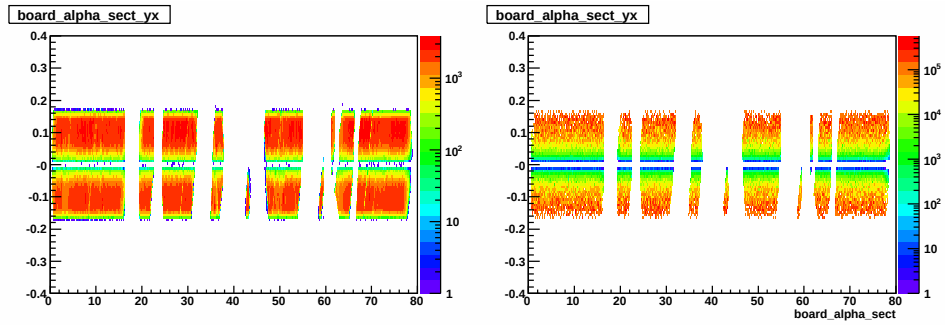

(c) sector 2

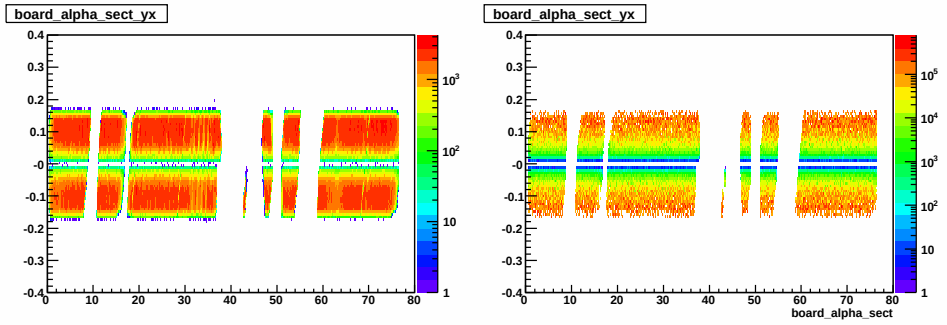

(d) sector 3

Figure 3.9: board vs alpha in data(left) and simulation(right)

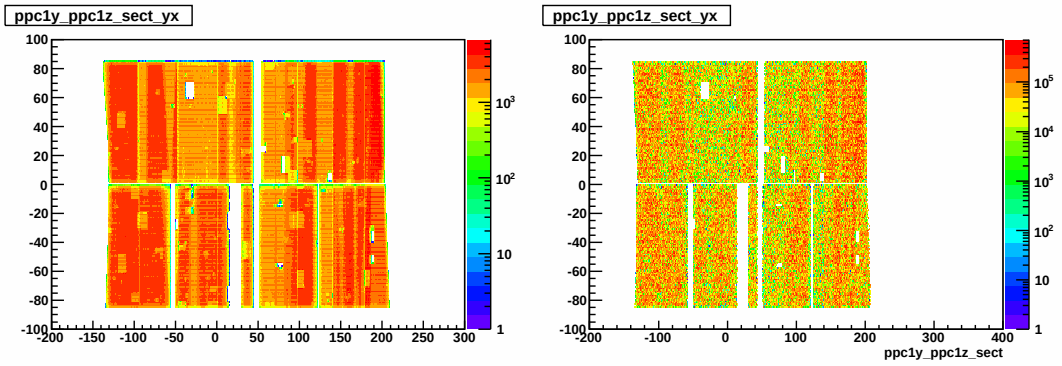

Figure 3.10: pc1y vs pc1z distribution in data (left plot) and simulation (right plot)

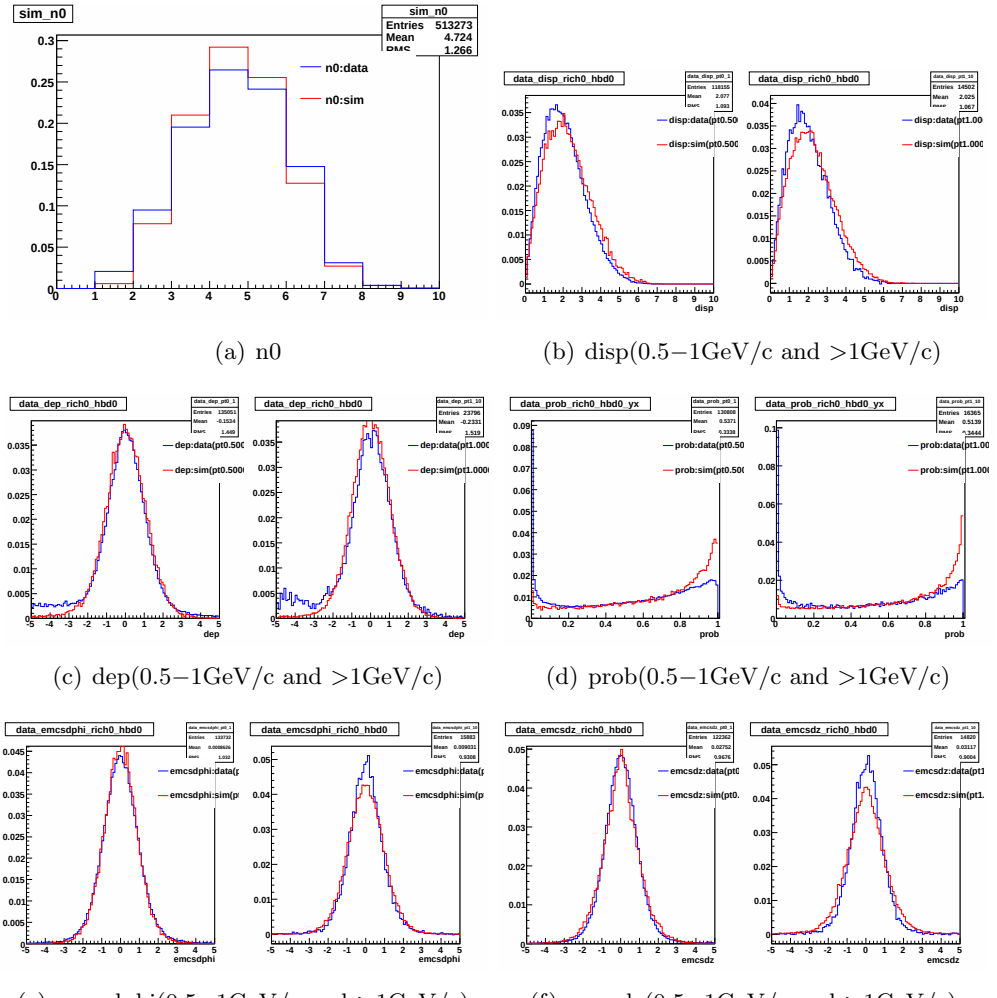

(a) n0

(b) disp(0.5−1GeV/c and >1GeV/c)

(c) dep(0.5−1GeV/c and >1GeV/c)

(d) prob(0.5−1GeV/c and >1GeV/c)

(e) emcsdphi(0.5−1GeV/c and >1GeV/c)

(f) emcsdz(0.5−1GeV/c and >1GeV/c)

Figure 3.11: n0, disp, dep, prob, emacsdphi, emacsdz distribution in simulation and real data

The CA acceptance and efficiency can be calculated by :

$$\epsilon^{CA}_{single} = \epsilon^{geo} \times \epsilon^{rec} \times \epsilon^{eID} = \frac{dN^{out}/dp_T}{dN^{in}/dp_T} \tag{3.3}$$

where dN^{in}/dp_T is the p_T distribution of the randomly generated single electrons or positrons as the PISA input. dN^{out}/dp_T is the p_T distribution of electrons or positrons which go through PISA and are reconstructed and passed all the eID cuts in the simulation.

The left plot of Fig. 3.12 shows the p_T distribution of the input single electrons, the electrons within CA active area and the electrons pass all the eID cuts. Efficiency loss is observed in each step. The middle plot of Fig. 3.12 shows the same distributions, but all the distributions are weighted with the actual p_T distribution of electrons. The right plot of Fig. 3.12 shows the acceptance (black curve) and the total CA efficiency for single electron tracks (blue curve).

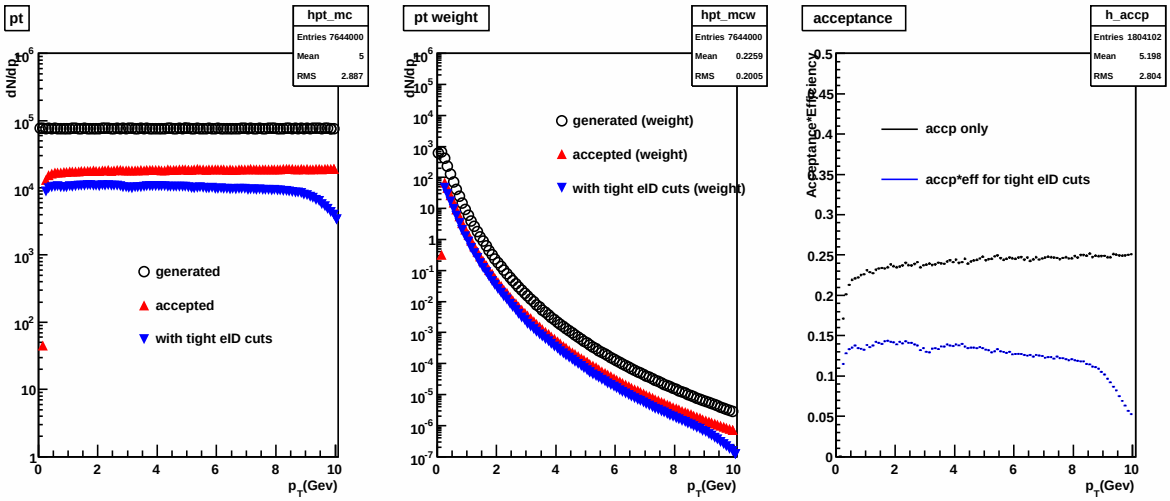

Figure 3.12: Central Arm acceptance and reconstruction efficiency vs p_T. The left plot is the unweighted simulation spectrum (black is generated, red is accepted by CA, blue is the electrons spectrum which passed all eID cuts). The middle plot is the weighted spectrum. The right plot is the acceptance plot (black) and acceptance×efficiency(blue)

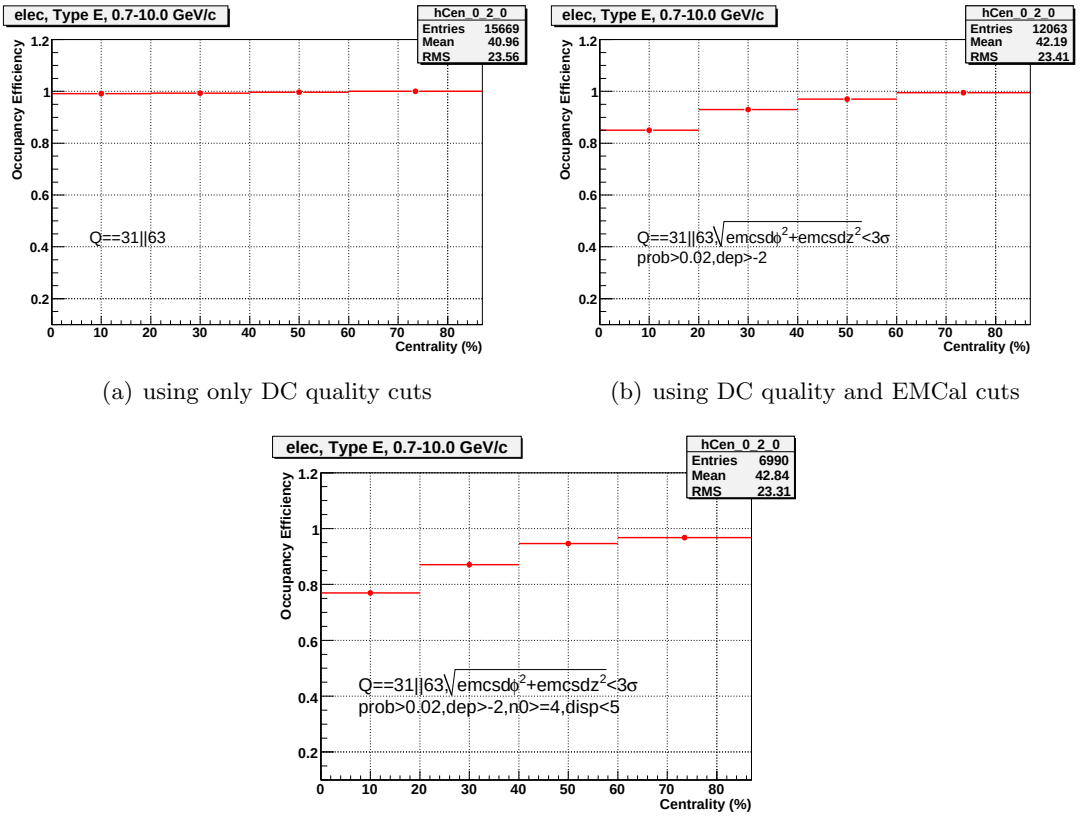

(a) using only DC quality cuts

(b) using DC quality and EMCal cuts

(c) using DC quality, EMCal and RICH cuts

Figure 3.13: Central Arm embedding efficiency vs centrality

3.6.2 Central Arm Multiplicity Dependent Efficiency

In additional to the single track efficiency loss, the efficiency loss due to the presence of nearby particles should also be considered. In Au + Au collisions, especially in the central events, there are multiple hits in the detector. We can imagine more particles there are, more difficult it is for the software to reconstruct each track, more efficiency is lost. Embedding method is used to estimate this kind of multiplicity dependence of efficiency loss.

The strategy is: single electron tracks are generated and pass through PISA chain, then the hits from single electron simulation are merged with the real Au + Au events whose z-vertex match the simulated events. The embedded electrons are reconstructed and applied all eID cuts in the same way as real data. Multiplicity dependent efficiency can be evaluated by Eq. 3.4.

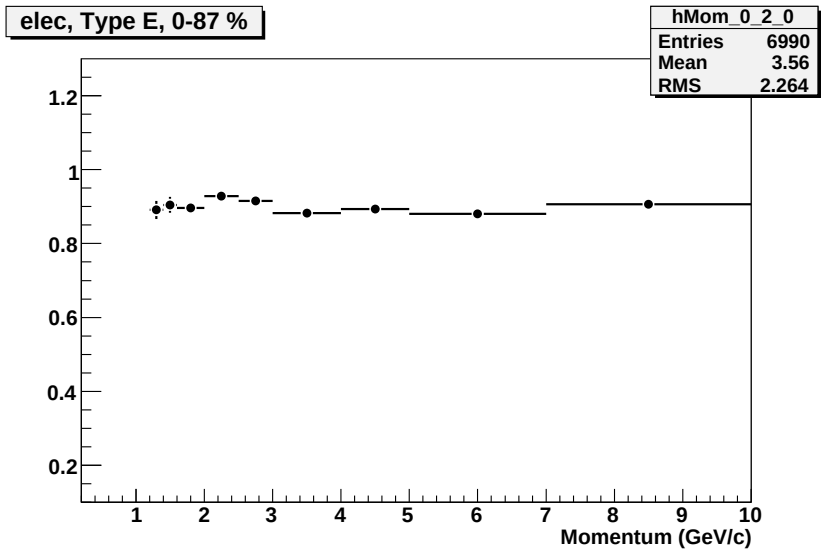

Figure 3.14: Central Arm embedding efficiency vs p_T using DC quality, EMCal and RICH cuts.

$$\epsilon_{embed}^{CA} = \frac{N_{reconstructed}^{embedded}}{N_{reconstructed}^{singletrack}} \tag{3.4}$$

Fig. 3.13(a), Fig. 3.13(b), Fig. 3.13(c) shows the centrality dependence of the embedding efficiency for 3 different sets of eID cuts (with flat p_T distribution). The embedding efficiency increases as centrality increases and the efficiency of EMCal cuts and RICH cuts has strongly dependence on centrality.

Fig. 3.14 shows the embedding efficiency vs p_T in MB data. All DC, EMCal and RICH cuts are applied. The embedding efficiency doesn't show p_T dependence within statistical errors between p_T 1 GeV/c to 6 GeV/c.

3.6.3 HBD Acceptance and Efficiency

HBD acceptance and efficiency is calculated separately from Central Arm acceptance and efficiency. Since single electrons and close electron pairs have different hbdq distribution, the HBD cut efficiencies are different for electrons from different sources. We consider three types of efficiency loss due to the HBD cut $10 < hbdq < 35$ in the analysis: the HBD cut efficiency for single electrons, the HBD cut efficiency for randomly matched tracks and the HBD cut efficiency

for electrons from photonic source. For each kind of efficiency, we simulate particles from each source and run through the GEANT simulation of the PHENIX detectors including the HBD detector. To obtain the HBD cut efficiency correction with the multiplicity dependence, we merge the HBD clusters in the simulation with the HBD clusters from real Au + Au events, then reconstruct tracks. The HBD acceptance and efficiency are calculated with Eq. 3.5 and Eq. 3.6.

$$\epsilon_{acc}^{HBD} = \frac{N_{HBDaccepted}}{N_{simulated}} \tag{3.5}$$

$$\epsilon_{eff}^{HBD} = \frac{N_{passed}}{N_{HBDaccepted}} \tag{3.6}$$

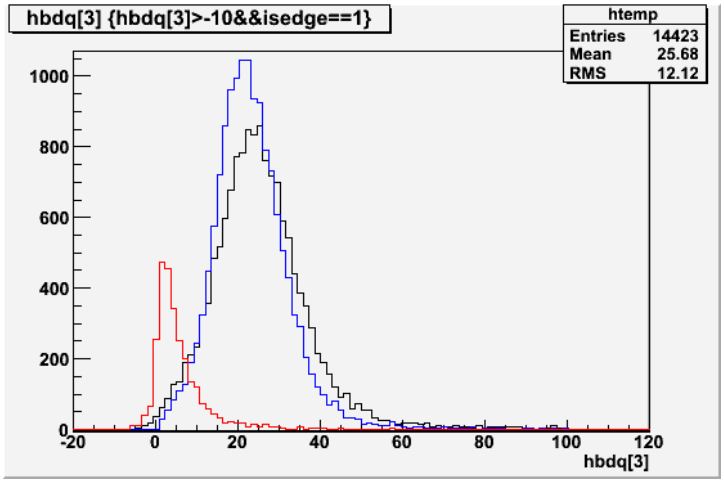

Figure 3.15: hbdq distribution. Blue line is the hbd charge of simulated single electron (MC only, not embedded). Black line is the single electron reconstructed in the embedded HBD clusters. Red line is the swapped single electron track reconstructed in embedded hbd clusters

Single electron events are used to calculate the HBD acceptance. Fig. 3.15 shows the hbdq distribution. The blue line is the hbdq of single electron. As expected, it is a Gaussian distribution centered at 20. The black line is the hbdq of the single electron reconstructed in the embedded HBD clusters. The embedded hbdq distribution is also a Gaussian distribution around 20 with wider width comparing to the hbdq distribution of single tracks. This is an effect from the neighboring fired HBD clusters in the events. The red line is the swapped hbdq

of the simulated single electron tracks reconstructed with the embedded HBD clusters. As discussed in Section 3.5, the swapped hbdq distribution represents the hbdq distribution of the randomly matched tracks.

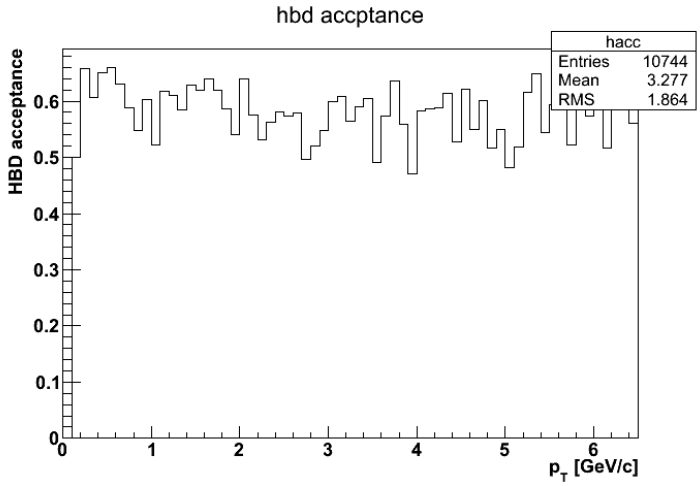

Figure 3.16: HBD acceptance vs p_T.

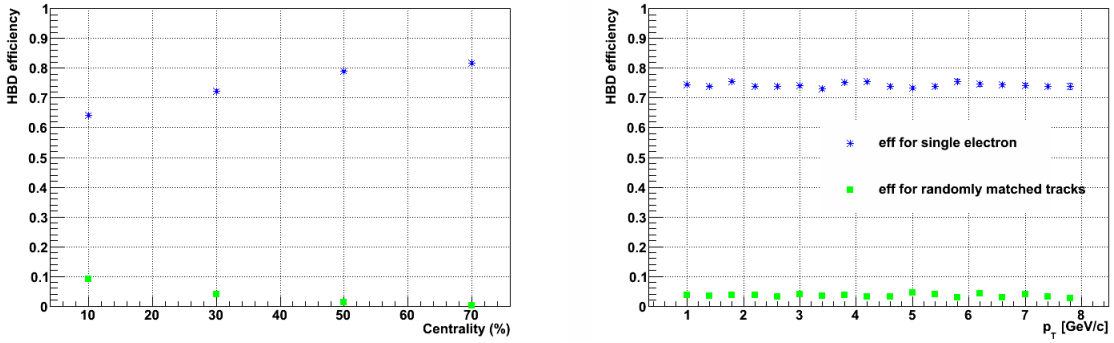

Figure 3.17: HBD cut efficiency for single electrons (blue star) and randomly matched tracks (green square) as a function of centrality (the left panel) and p_T (the right panel).

The simulation shows us that the HBD acceptance ϵ_{acc}^{HBD} is around 0.6 (Fig. 3.16). After applying the HBD cut $10 < hbdq < 35$ to the simulation, the HBD efficiency for single electrons $\epsilon_{eff}^{HBD,single}$ and the HBD efficiency for randomly matched tracks $\epsilon_{eff}^{HBD,random}$ are

shown in Fig. 3.17 in blue and green dots. Both $\epsilon_{eff}^{HBD,single}$ and $\epsilon_{eff}^{HBD,random}$ have a centrality dependence, but no obvious p_T dependence for $0.1 < p_T < 8GeV/c$. In the most central events, because of the high multiplicity, the probability for a track to randomly match with a HBD cluster is high. At the same time, the hbdq distribution of a single electron is smeared by the HBD clusters which are fired by nearby tracks. Therefore, $\epsilon_{eff}^{HBD,random}$ is the highest and $\epsilon_{eff}^{HBD,single}$ is the lowest in the central track. Although a very small amount of randomly matched tracks (most are electrons from the conversions at HBD backplane) might survive the HBD cut and HBD swapping subtraction, the remaining amount can still be estimated o Dalitz ratio (R_{CD}) in the cocktail method. More details will be discussed in Chapter 4.

Besides the HBD efficiency for single electrons, we also need to calculate the HBD efficiency for electrons from photonic sources. The decay products of photonic sources are usually electron positron pairs. As discussed in Chapter 2, the close electron pairs will be associated with merged HBD clusters with the hbdq distribution centered at 40 (double signal), while the open electron pairs will be associated with two HBD clusters separately with the hbdq distribution centered at 20. In another words, an open electron pair is equivalent to two single electrons (single signal). Obviously, our cut $10 < hbdq < 35$ have different efficiencies on these two kinds of signals. For each photonic source, the daughter electron pairs are a mixture of close and open pairs. The HBD cut efficiency is a function of the decay opening angle which is determined by the parent mass and the decay kinematics.

$\pi^0 \to \gamma + e^- + e^+$, $\eta \to \gamma + e^- + e^+$, $\eta' \to \gamma + e^- + e^+$, $\rho \to e^- + e^+$, $\omega \to e^- + e^+$, $\phi \to e^- + e^+$ decays are simulated. Similar as single electrons, HBD cut efficiencies are calculated for each photonic source. Since in the cocktail method which is going to be discussed in Chapter 4, the yield of conversion electrons from $\pi^0 \to \gamma + \gamma$ is obtained by scaling the yield from the π^0 Dalitz decay with the conversion to Dalitz ratio (R_{CD}), the efficiency for conversions electrons from $\pi^0 \to \gamma + \gamma$ is not calculated separately in this section. Fig. 3.18 shows the opening angle, centrality and p_T dependence of the efficiency. In the left panel, the efficiencies for electrons from π^0, η and η' Dalitz decays are plotted as a function of opening angle. When the opening angle is small, the electron pairs are most likely to leave double signals in the HBD, therefore our HBD cut can remove most of these small opening angle pairs. When the opening angles

are large, the electron pairs leave single signals in the HBD, therefore the HBD efficiency of large opening angle pairs is same as that of single electrons. In the middle panel, the centrality dependence of the HBD efficiency is plotted. Electrons from ρ, ω, ϕ have the same efficiency as single electrons. The reason is that, because of the large mass, these particles have large opening angle, almost all the daughter electron pairs are considered as single signals in the HBD. For electrons from π^0, η, η', as the mass of the parent meson increases, the opening angle of the electron pair also increases, then the HBD efficiency increases. The right panel is the p_T dependence of the HBD efficiency. At high p_T, electron pairs from π^0, η, η' have smaller opening angle, that is why the efficiency is lower at high p_T.

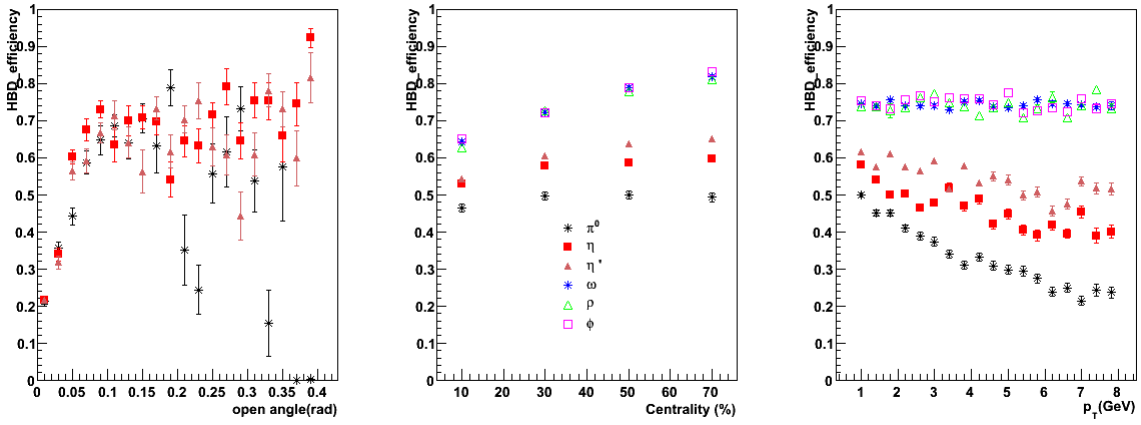

Figure 3.18: HBD cut efficiency for electrons from various photonic sources as a function of opening angle (the left panel), centrality (the middle panel) and p_T (the right panel).

The inclusive electron contains both the single electrons from the heavy flavor meson decays and the electron pairs from the photonic sources.

$$N_{inclusive} = N_{hf} + N_{photonic} = \epsilon_{eff}^{HBD,single} \times n_{hf} + \epsilon_{eff}^{HBD,photonic} \times n_{photonic} \tag{3.7}$$

$$n_{hf} = \frac{N_{inclusive}}{\epsilon_{eff}^{HBD,single}} - \frac{\epsilon_{eff}^{HBD,photonic}}{\epsilon_{eff}^{HBD,single}} \times n_{photonic} \tag{3.8}$$

Where N is the measured spectrum and n is the yield of the particle.

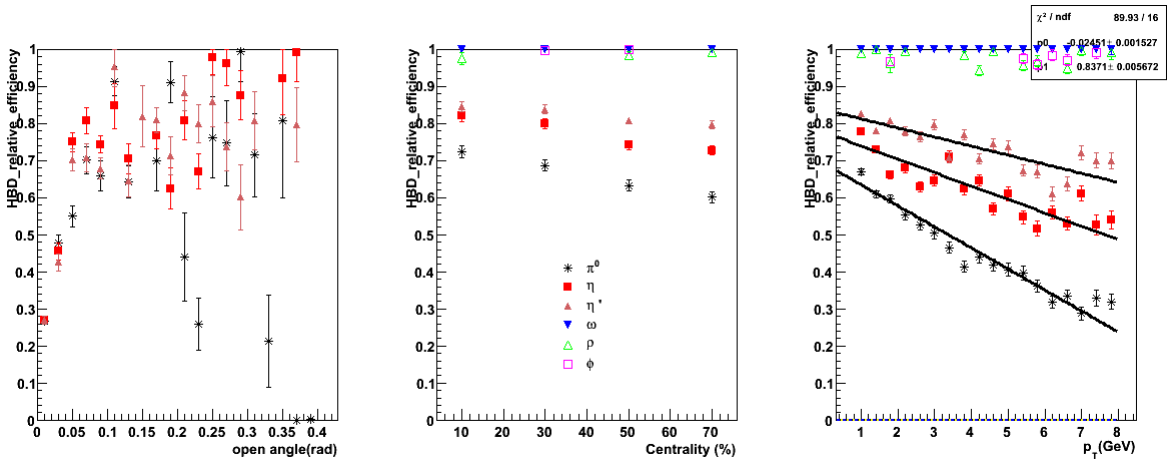

Figure 3.19: HBD cut efficiency for electrons from various photonic sources as a function of opening angle (the left panel), centrality (the left panel) and p_T (the right panel).

To obtain the heavy flavor electron invariant yield, we need to correct the measured inclusive electron spectrum with $\epsilon_{eff}^{HBD,single}$, then subtract the photonic electron invariant yield times $\frac{\epsilon_{eff}^{HBD,photonic}}{\epsilon_{eff}^{HBD,single}}$, which is the relative HBD efficiency of each photonic source comparing to the efficiency of single electrons. The photonic electron invariant yield is estimated in Chapter 4. The relative HBD efficiency is shown in Fig. 3.19.

3.6.4 Bin Width Correction

Because of the limited statistics, instead of measuring dN/dpt, we actually measure the average number of electron yield in a given p_T bin by filling a p_T histogram. However, the average p_T value in each p_T bin depends on the binning and the spectrum shape. $\langle p_T \rangle$ is not exactly at the center of the bin. Different measurement may have different binning, therefore, instead of measuring the average electron yield in a given p_T bin, we want to obtain the electron yield at a given value of p_T, for example, at the center of each p_T bin, by applying the bin width correction.

1. The electron p_T spectrum is fitted with Eq. 3.9.

$$f(p_T) = \frac{c}{(e^{-ap_T - bp_T^2} + \frac{p_T}{p_0})^n} \tag{3.9}$$

Where a, b, c, n, p_0 are fitting parameters.

2. $\langle p_T \rangle$ can be calculated by Eq. 3.10

$$\langle p_T \rangle = \frac{\int p_T f(p_T) dp_T}{\int f(p_T) dp_T} \tag{3.10}$$

3. We move the data point from the center of the bin to $\langle p_T \rangle$ and fit with Eq. 3.9 again.

4. Repeat steps 2 and 3 until the parameters of Eq. 3.9 converge.

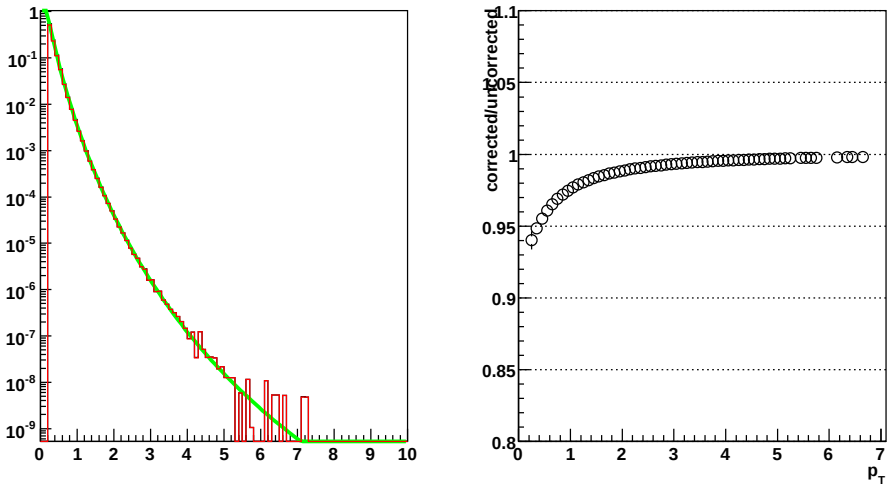

Figure 3.20: Bin width correction. Left plot is the pT spectrum before (black) and after (red) bin width correction. The Hagedorn function is showed in green. The right plot is the ratio of corrected spectrum and uncorrected spectrum as a function of p_T

The yield at the center of the p_T bin ($p_{T\,center}$) is calculated by Eq. 3.11. Fig 3.20 shows us that the correction is around 2% at p_T 1−7 GeV/c.

$$y(p_{T\,center}) = y_{data} \times \frac{f(p_{T\,center})}{f(\langle p_T \rangle)} \tag{3.11}$$

3.7 Inclusive Electron Spectrum

In summary, considering all the corrections mentioned in Section 3.6, Fig. 3.21 shows the invariant yield of inclusive electrons which contains electrons from heavy flavor meson decays and other sources. In the next chapter, we will estimate the background using the cocktail method.

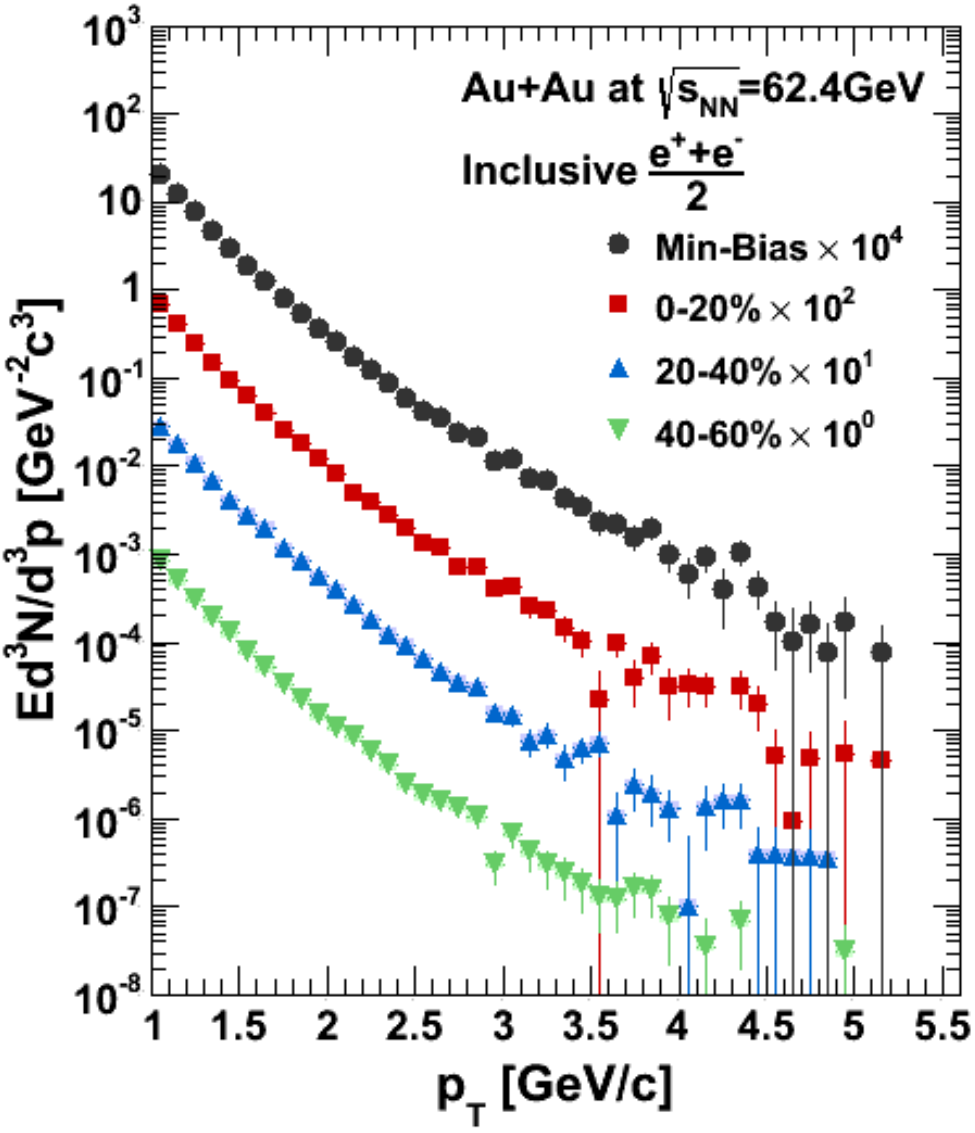

Figure 3.21: Invariant yield of inclusive electrons for various centrality bins.

3.8 Inclusive Electron v_2

Azimuthal anisotropy v_2 of inclusive electrons is measured by the reaction plane method (Eq. 3.12)

$$\frac{dN}{d\phi} = N_0(1 + 2v_2 \cos 2(\phi - \Phi_{RP})) \tag{3.12}$$

Where ϕ is the azimuthal angle of the electron track and Φ_{RP} is the azimuthal angle of the reaction plane N_0 is a normalization constant.

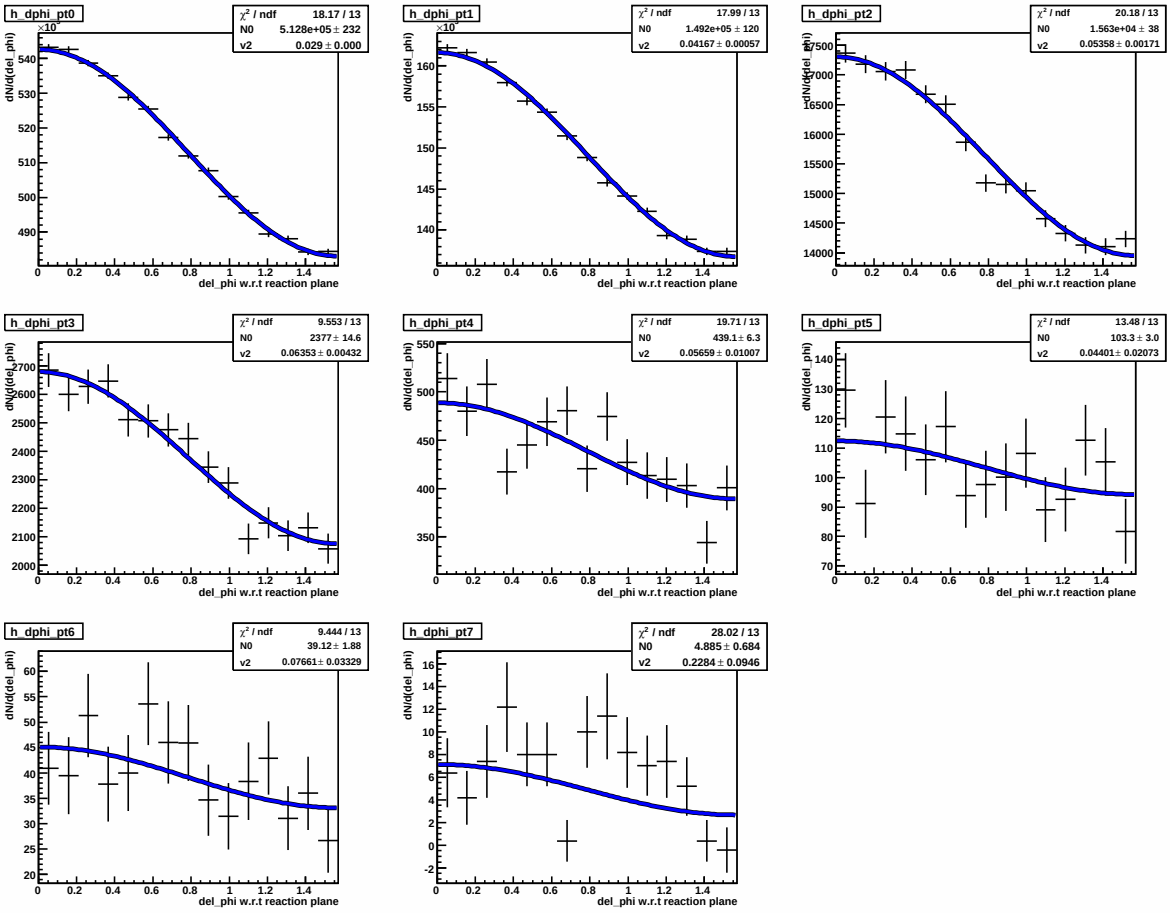

Figure 3.22: Inclusive electron yield w.r.t reaction plane for different p_T bins (MB data) and fitted with cos function.

Reaction plane is the plane formed by the centers of the colliding nuclei and the beam direction. In this analysis, the Reaction Plane Detector (RXNP), which has almost two times better reaction plane resolution comparing to the BBC resolution, is used to measure the reaction plane event by event.

To calculate v_2, the inclusive electron yield with respect to reaction plane ($\phi - \Phi_{RP}$) for selected p_T bins and centrality bins are plotted, then fitted with Eq. 3.12, as shown in Fig. 3.22).

The second coefficient in the Fourier extension which is extracted from the fitted curves of the particle yield with respect to the measured reaction plane is ${v_2}^{raw}$.

3.8.1 Reaction Plane Resolution

By correcting the ${v_2}^{raw}$ with the reaction plane resolution (Eq. 3.13), v_2 from the particle distribution with respect to the real reaction plane can be measured.

$$v_2 = \frac{v_2^{RAW}}{resolution} \equiv \frac{v_2^{RAW}}{cos(2(\Phi_{measured} - \Phi_{real})} \tag{3.13}$$

where $\Phi_{measured}$ and Φ_{real} are the measured and real reaction plane angle.

The resolution is always less than one, therefore v_2 after the correction is always larger than the raw flow coefficients.

If the event planes are constructed in two different windows (for example, the south side of the RXNP and the north side of the RXNP), or from two random sub-events, Eq. 3.14 is a well approximation of the reaction plane resolution.

$$< \cos(2(\Psi_{measured} - \Psi_{real})) > \quad \sim \quad \sqrt{< \cos(2(\Psi_{measured}^{South} - \Psi_{measured}^{North})) >} \tag{3.14}$$

where $\Psi_{South}^{measured}$,$\Psi_{North}^{measured}$ is the measured reaction plane using only south or north side of the detector.

Fig. 3.23 shows the reaction plane resolution vs centrality using RXN, outer layer of RXN only, inner layer of RXN only and MPC. The reaction plane measure by RXN has the best resolution.

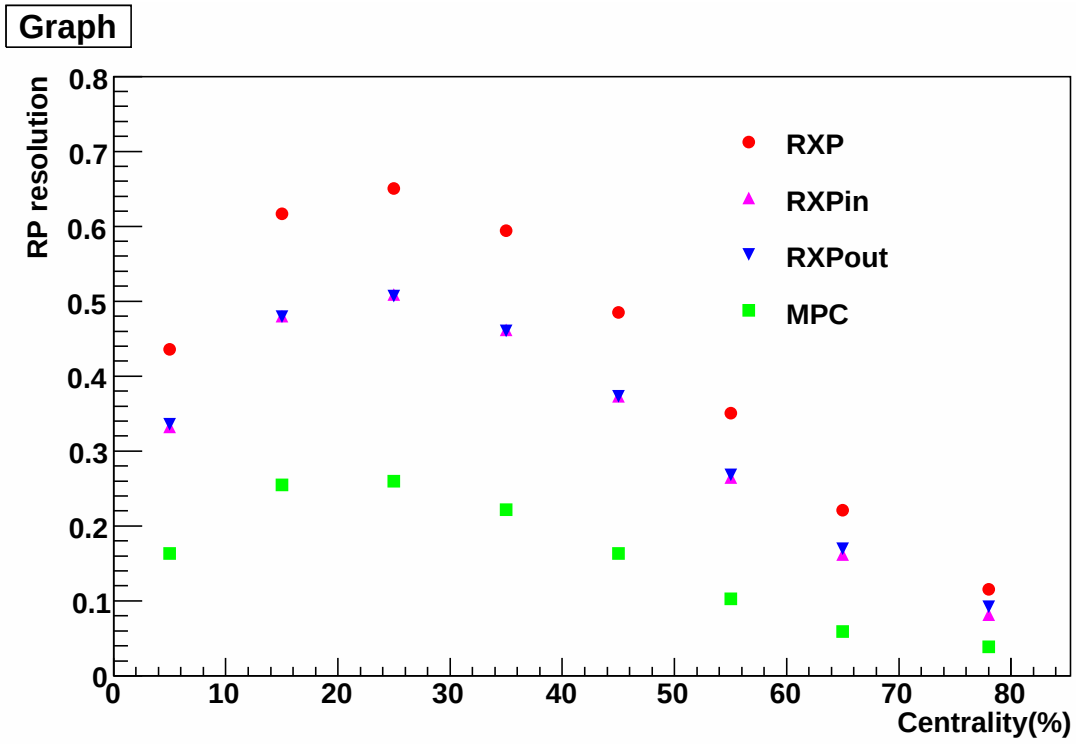

Figure 3.23: Reaction plane resolution vs centrality measured by MPC,RXNPin,RXNPout and RXNP

3.8.2 inclusive electron v_2

As we discussed in the previous sections, Fig. 3.22 shows that how the inclusive electrons flow as a function of $\phi - \Phi_{RP}$. The second parameter in the fitting function is the ${v_2}^{raw}$. After corrected by the reaction plane resolution with Eq. 3.13, the inclusive electron v_2 for different centrality bins is shown in Fig. 3.24. In the mid-centrality, the inclusive electrons have the maximum flow due to the largest asymmetry of the shape of the collision area.

The statistical error of inclusive electron v_2 is from fitting. The systematic error of the inclusive electron v_2 is mainly from the reaction plane resolution (5%). The systematic error from the electron measurement is very small because the uncertainties from scaling or normalization in the spectrum measurement do not affect the shape of the electron distribution with respect to the reaction plane. To sum up, a systematic error of 5 % is assigned to the inclusive

electron v_2.

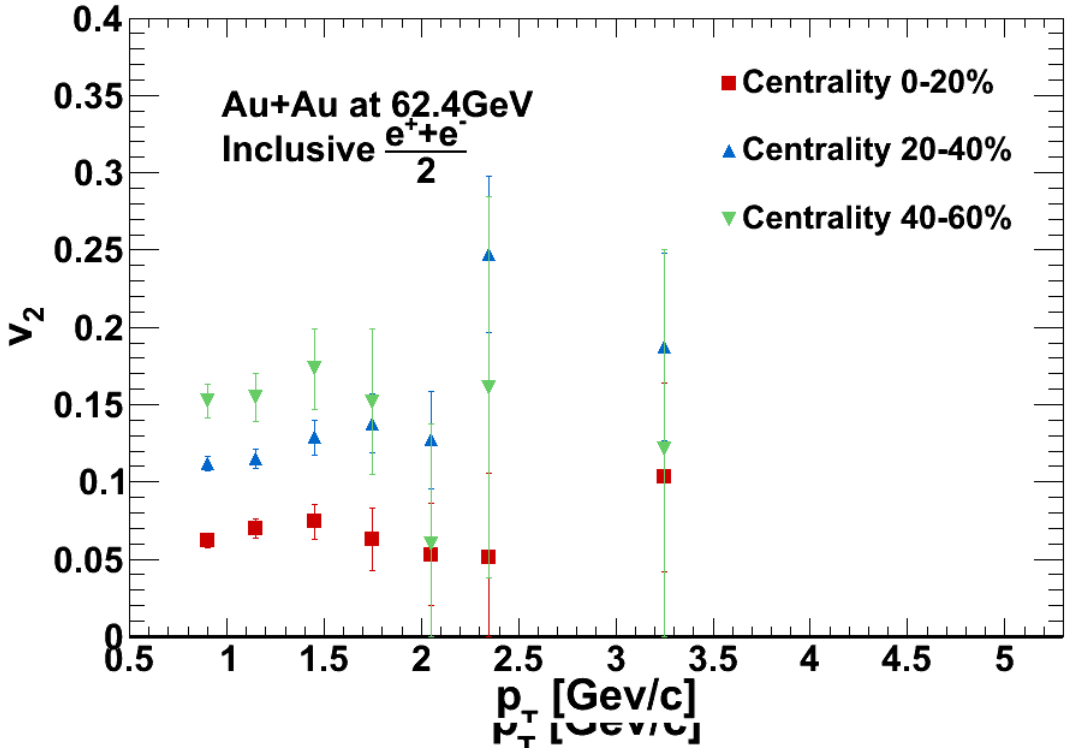

Figure 3.24: inclusive electron v_2 vs p_T for different centrality bins

CHAPTER 4. ESTIMATION OF PHOTONIC BACKGROUND

The inclusive electrons measured in PHENIX contains not only electrons from heavy flavor meson decays, but also from other sources, for instance, light meson decays, photon conversions, direct photon conversions, Ke3 decays and so on. These electrons are considered as the background in our analysis and have to be subtracted from the inclusive electrons to isolate the signal. In this chapter, we will introduce the cocktail method which estimates the electron background from the PHENIX measurement of decay sources.

4.1 Cocktail Method Overview

We use EXODUS event generator to simulate the photonic electron cocktail from different sources. The following decays are considered in EXODUS:

- $\pi^0 \to \gamma + e^- + e^+$
- $\eta \to \gamma + e^- + e^+$
- $\eta' \to \gamma + e^- + e^+$
- $\rho \to e^- + e^+$
- $\omega \to e^- + e^+$ and $\omega \to \pi^0 + e^- + e^+$
- $\phi \to e^- + e^+$ and $\phi \to \eta + e^- + e^+$
- Photon conversions
- Ke3 decays
- Conversions of direct photon

The dominant sources of photonic background come from π^0 and η Dalitz decays and conversions of photons from $\pi^0 \rightarrow \gamma + \gamma$.

In general, a realistic distribution of the invariant yield of π^0 in the same collision system is used as the EXODUS input. The spectrum of other light mesons can be obtained from the π^0 spectrum with m_T scaling. Then EXODUS can simulate the Dalitz decays of light mesons and estimate the distribution of daughter electrons. The distribution of electrons from photon conversions can be obtained by scaling the distribution of electrons from Dalitz decays by the so called conversion to Dalitz ratio (R_{CD}).

4.2 Cocktail Input

4.2.1 π^0 p_T Spectrum

PHENIX has measured the π^0 spectrum in Au + Au collisions at $\sqrt{s_{NN}} = 62.4$ GeV [31]. The π^0 spectrum can be used as the cocktail input by fitting it with a modified Hagedorn function (Eq. 4.1).

$$E\frac{d^3N}{d^3p_T} = \frac{c}{(e^{-ap_T - bp_T^2} + \frac{p_T}{p_0})^n} \tag{4.1}$$

Fig. 4.1 shows the π^0 p_T spectrum for each centrality and the ratio of the data to the fitted curve. The fitted curve represents the π^0 data very well. In Table 4.1, the parameters of Hagedorn function for various centrality bins are listed.

Table 4.1: Fit parameters for the π^0 invariant yield according to the Hagedorn function Eq. 4.1

Centrality	**c**	**a**	**b**	p_0	**n**
Min-Bias	657.07	0.32513	0.0644465	1.01473	11.1849
0-20%	1175.06	0.367545	0.0984917	0.991605	10.8928
20-40%	795.481	0.298255	0.0393908	1.09584	11.5588
40-60%	294.364	0.328543	0.05098	1.01267	10.9529

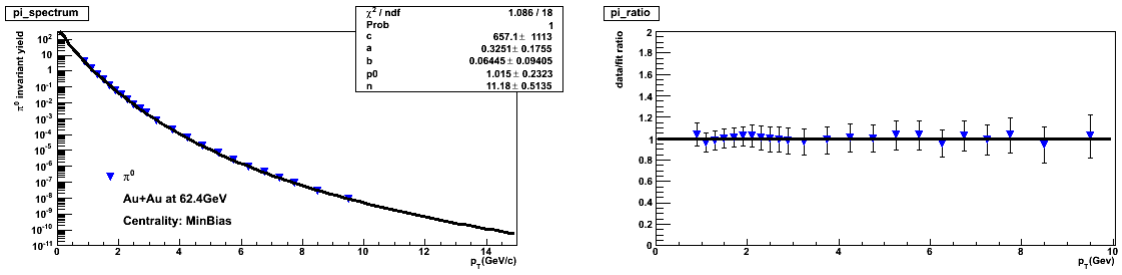

(a) MinBias

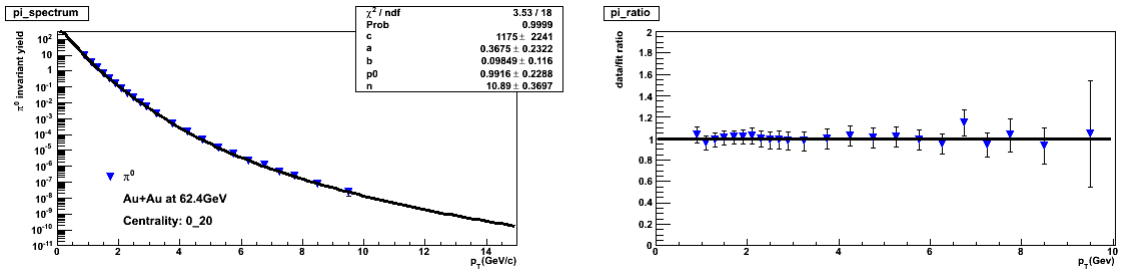

(b) Centrality 0-20%

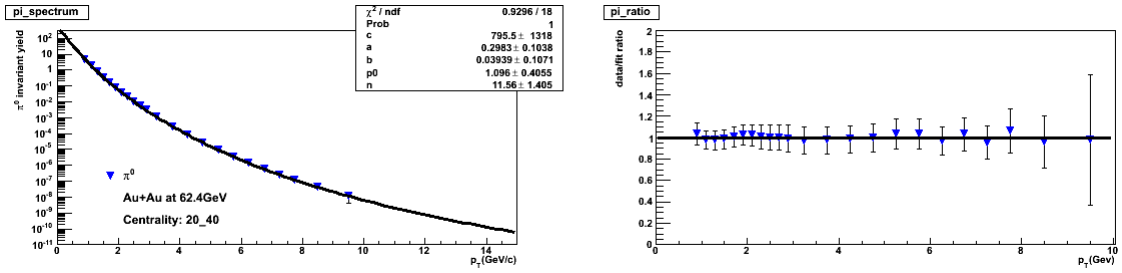

(c) Centrality20-40%

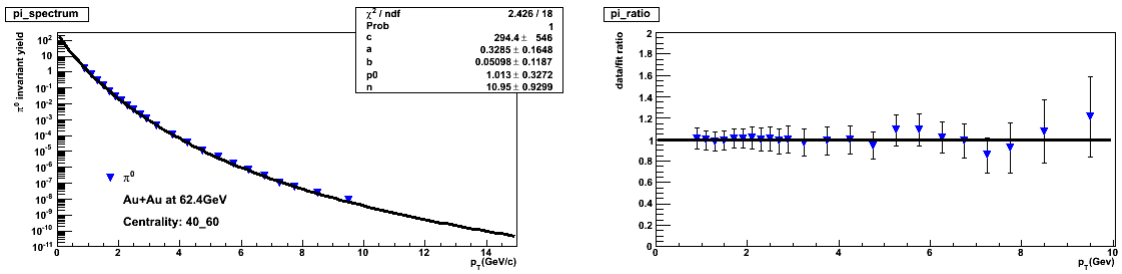

(d) Centrality 40-60%

Figure 4.1: Invariant yield of π^0 and the associated fitted curve according to Eq. 4.1 for various centrality bins (left panels), and the ratio of the π^0 data to the fitted curve (right panels)

4.2.2 Other Light Mesons

Other light mesons, for example η, η', ρ, ω, ϕ, also contribute to the electron cocktail. The contribution of η meson decays is around 10% of the total photonic background for $1 < p_T < 10 GeV/c$. The contribution of η', ρ, ω and ϕ are relatively small. The shape of other light meson's spectrum can be determined from the π^0 spectrum by m_T scaling, which means that the p_T in the Hagedorn function is replaced by m_T (Eq. 4.2), while the parametrization is same as π^0.

$$m_T = \sqrt{{p_T}^2 + {m_{meson}}^2 - {m_{\pi^0}}^2} \tag{4.2}$$

The relative normalization of other mesons to pion can be obtained from the meson to pion ratios at high p_T as listed below:

- $\eta/\pi^0 = 0.48 \pm 0.03$ [44];
- $\phi/\pi^0 = 1.00 \pm 0.30$ [45];
- $\omega/\pi^0 = 0.90 \pm 0.06$ [46];
- $\eta'/\pi^0 = 0.25 \pm 0.075$ [46];
- $\rho/\pi^0 = 0.40 \pm 0.12$ [46];

4.2.3 Photon Conversions and R_{CD}

Conversion electrons which come from the conversion of photons in the detector material is another major source of the photonic background. Photon conversions can happen in the whole detector material, including the beam pipe, the HBD detector, and all Central Arm detectors. With the eID cuts, electrons from conversions in the Central Arm detectors should already be removed. With HBD cuts and HBD swapping, the conversion electrons from the HBD back plane should also be removed already. This means, in our analysis, the conversion electron background is mainly from conversions in the beam pipe, the HBD entrance part and the CF_4 gas in the HBD detector.

Most of the parent photons are from $\pi^0 \to \gamma\gamma$. The kinematics of the daughter electron pairs is similar to the electron pairs from $\pi^0 \to \gamma + e^- + e^+$. Therefore, we can run a full GEANT simulation to determine the ratio of conversion electrons to electrons from Dalitz decays (R_{CD}), scale the spectrum of electrons from π^0 Dalitz decays, which is the output of EXODUS, with R_{CD} to obtain the spectrum of electrons from photon conversions.

The definitinon of R_{CD} is:

$$R_{CD} \equiv \frac{Yield_{conv}}{Yield_{Dalitz}} \tag{4.3}$$

Then,

$$Yield_{conv} = Yield_{Dalitz} \times R_{CD} \tag{4.4}$$

Where $Yield_{conv}$ is the yield of electrons from photon conversions in the detector material, $Yield_{Dalitz}$ is the yield of electrons from the Dalitz decays.

$\pi^0 \to \gamma + e^- + e^+$ and $\pi^0 \to \gamma + \gamma$ events are simulated with the full GEANT simulation of the PHENIX detector. The parent π^0 spectrum is weighted with the Hagedorn function of the MinBias π^0 spectrum. The same eID cuts, fiducial cuts and HBD cuts as the data analysis are applied to the simulated tracks. The HBD swapping method is also applied to the simulation. We count the number of electrons from the photon conversions per event and the number of electrons from the Dalitz decays per event to determine the R_{CD} (Eq. 4.5)

$$R_{CD}(p_T) = \frac{N_{Conv}(p_T) \times 0.98823}{N_{Dalitz}(p_T) \times 0.01174}; \tag{4.5}$$

Where $N_{Conv}(p_T)$ is the number of electrons from the photon conversions per event after applying all the cuts, $N_{Dalitz}(p_T)$ is the number of electrons from the Dalitz decays per event after applying all the cuts, 0.98823 is the branching ratio of $\pi^0 \to \gamma + \gamma$ and 0.01174 is the branching ratio of $\pi^0 \to \gamma + e^- + e^+$.

Fig. 4.2 shows the R_{CD} as a function of p_T. We fit the plot with a linear function for $1 < p_T < 8$ GeV/c. In the Run-10 analysis, with the HBD cut $10 < hbdq < 35$, the R_{CD} value increases as p_T increases, and is higher than the ratio in Run-4 (${R_{CD}}^{Run-4} = 0.403$). In Run-4, HBD was not installed. Instead, a helium bag was placed between the beam pipe and the drift chamber to minimize the material which can cause photon conversions. However,

in our case, besides the beam pipe, a large proportion of photon conversions happen at both the HBD entrance part and the CH_4 gas in the HBD. In additional, since the upper hbdq cut removes some fraction of the Dalitz decays, the denominator of the R_{CD} is smaller in Run-10. Therefore, R_{CD} of Run-10 is much larger than the Run-4 value.

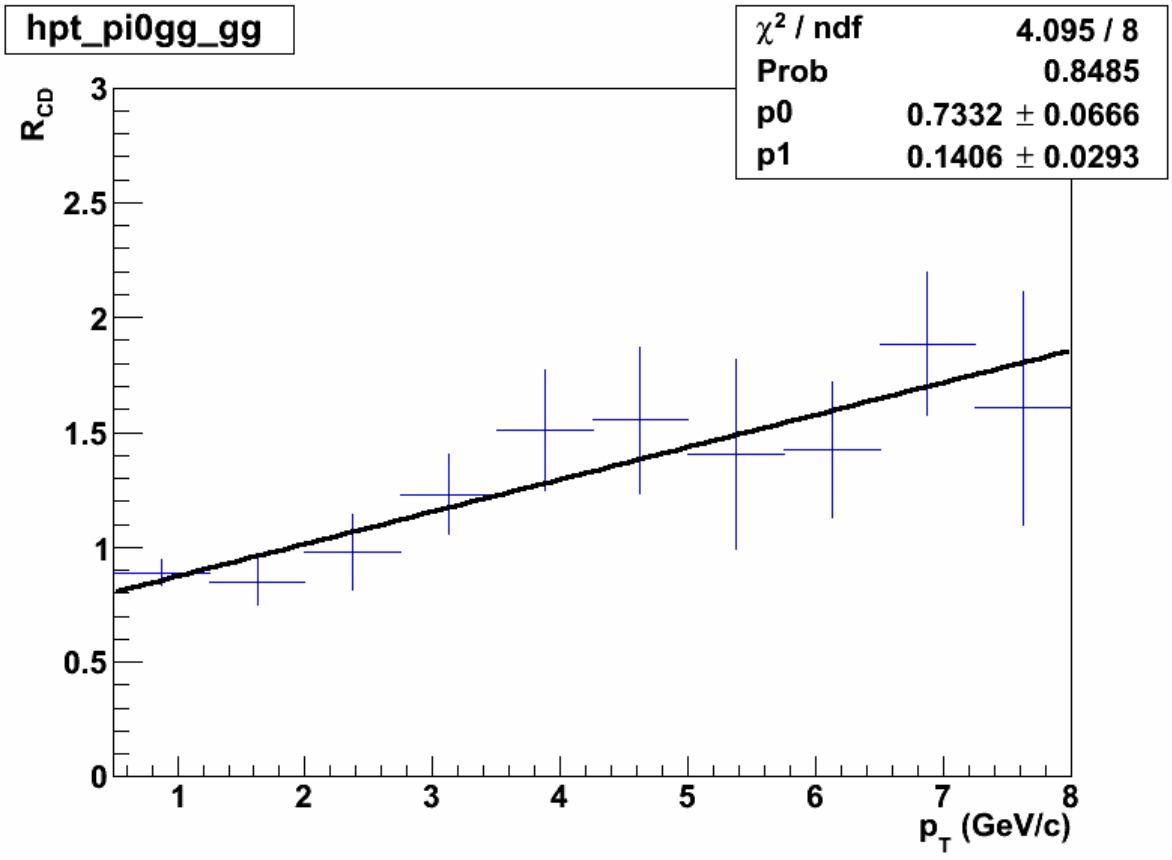

Figure 4.2: The conversion to Dalitz ratio (R_{CD}) as a function of p_T

A systematic error of 10% is assigned to the uncertainty of the amount of material in the PHENIX. In additional, we describe R_{CD} as a linear function of p_T. This simple assumption may cause systematic uncertainty in our analysis. Therefore, to be conservative, another 10% systematic error is assigned to the imperfect modelling of the R_{CD}.

4.2.4 Ke3 Decays

Ke3 decay is the three-body kaon decay including an electron as one of the decay products, for instance, $K^{\pm} \rightarrow \pi^0 e^{\pm} \nu_e$. Ke3 decays contribute 5-10% of the photonic cocktail at low p_T (p_T <1 GeV/c). But as p_T increases, the percentage of the Ke3 contribution in the total cocktail quickly decrease to 1% for $p_T > 1$ GeV/c. Since our heavy flavor electron measurement starts at ${p_T}^e = 1$ GeV/c, the kaon contribution is very small. We just approximately estimate the amount of electrons from Ke3 decays in the cocktail.

Different from Dalitz decays of light mesons, Ke3 decays happen far away from the primary collision vertex. Two things will be different for electrons from Ke3 decays compare to the electrons from collision vertex.

Firstly, because the momentum reconstruction algorithm assumes that all the tracks come from the collision vertex and travel through the full magnet field, the reconstructed p_T of the electrons from Ke3 decays is usually higher than the real p_T of the track. Therefore, most Ke3 tracks will be removed by the E/p cuts.

Secondly, if the Ke3 decay happens in the middle of the HBD detector or after the HBD detector, the daughter electrons may not be able to fire the HBD detector. HBD charge cuts can also eliminates some of the electrons from Ke3 decays.

In Run-2, a full GEANT simulation was done to determine the contribution of electrons from Ke3 decay in Au + Au Min-Bias collisions at $\sqrt{s_{NN}} = 200$ GeV, taking into account the eID cuts efficiency. The ratio of the measured kaon yield using data of Au + Au $\sqrt{s_{NN}} = 62.4$ Gev collisions to the yield using data of $\sqrt{s_{NN}} = 200$ GeV collisions is roughly 0.5 around p_T = 1 GeV/c [47]. A simple Monte Carlo simulation shows that about 1/3 of the electrons from Ke3 decays can survive from the HBD cuts. We scale the electrons yield from Ke3 decays in Au + Au collisions at $\sqrt{s_{NN}} = 200$ GeV with a factor of $0.5 \times \frac{1}{3}$ to obtain the yield at $\sqrt{s_{NN}} =$ 62.4 GeV for Min-Bias events. For other centrality bins, we scale the Ke3 background according to $< N_{coll} >$. A conservative systematic error of 50% is assigned to the Ke3 contribution.

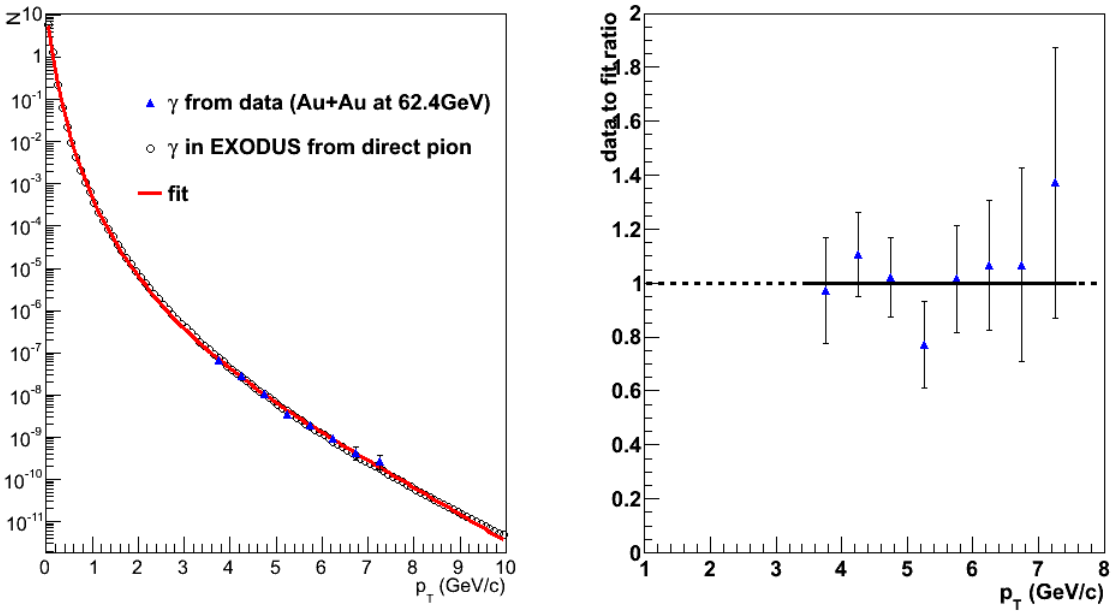

Figure 4.3: The left panel is the direct photon spectrum measured in PHENIX in Au + Au collisions at $\sqrt{s_{NN}} = 62.4$ GeV for Min Bias data (blue triangle) [48] and the photon spectrum from EXODUS (black open circle) which is fitted to the red curve. The right panel is the ratio of the measured direct photon spectrum to the red curve.

4.2.5 Direct Photon Contribution

Direct photons contribute to the cocktail background by the real direct photons converting in the material and the virtual direct photon internal conversions.

EXODUS estimates electrons from the direct photons by a artificial particle called direct π which can decay to 2γ and $\gamma + e^+ + e^-$, just like π^0. We can assume that the γ in the direct π to 2γ decays is direct photon, then the electrons from the direct π to $\gamma + e^+ + e^-$ can represent the electrons from virtual direct photon internal conversions. The direct π spectrum is tuned to match the daughter γ distribution to the direct photon yield which has been measured by PHENIX in Au + Au collisions at $\sqrt{s_{NN}} = 62.4$ GeV for Min-Bias data (Fig. 4.3) [48]. The branching ratio of direct π to 2γ decays and direct π to $\gamma + e^+ + e^-$ decays is determined by the ratio of real direct photon to the virtual direct photon. The relative branching ratio for

direct π to $\gamma + e^+ + e^-$ decays to direct π to 2γ decays increases as p_T increases, since the larger photon p_T leads to a larger phase space for the virtual photon internal conversion. Fig. 4.3 shows a good match of the measured direct photon and the simulated photon from the direct π decays in EXODUS. The electron spectrum from the modified direct π decays is the direct photon contribution in the cocktail for the MB events. For other centrality bins, we scale the electron spectrum according to the $< N_{coll} >$.

A systematic error of 20% is assigned to the electron spectrum from direct photons based on the systematic error on the measured direct photon spectrum.

4.3 Photonic Electron Cocktail

We have discussed every contribution to the photonic electron cocktail. Fig. ?? shows the completed cocktail for MB events. However, because of the HBD cut efficiency for single electrons and for photonic electrons are different, each cocktail component needs to be corrected by a factor of $\frac{\epsilon_{eff}^{HBD,photonic}}{\epsilon_{eff}^{HBD,single}}$ to obtain the actual amount of the photonic electrons in the inclusive electron invariant yield (Section 3.6.3). Fig. ?? shows the cocktail for MB events after the correction. The HBD cut significantly reduces the photonic electron background by around 35% at $p_T = 2$ GeV/c in our analysis .

Finally, the background electron cocktails for different centrality bins in the Run-10 Au + Au $\sqrt{s_{NN}} = 62.4$ GeV data are shown in Fig. 4.6.

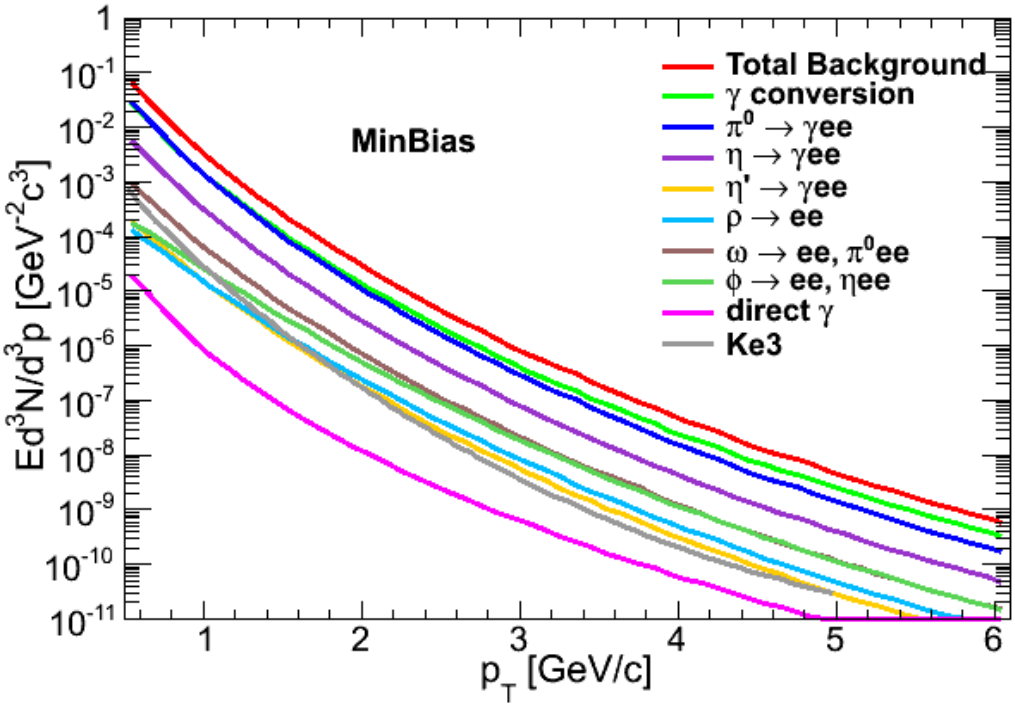

Figure 4.4: The photonic electron cocktails as a function of p_T for MB data before the HBD efficiency correction.

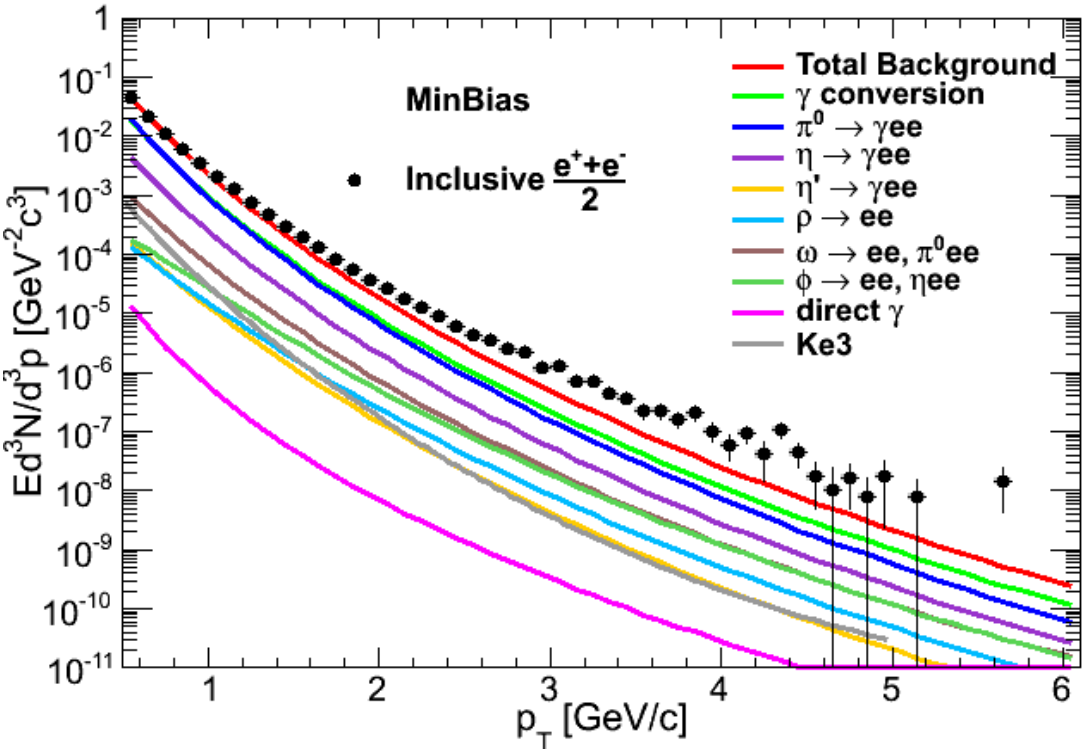

Figure 4.5: The photonic electron cocktails as a function of p_T for MB data and after the HBD efficiency correction.

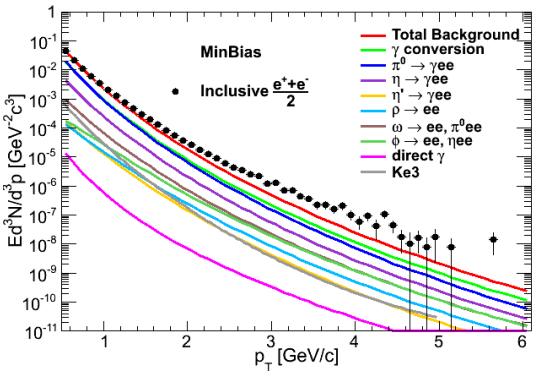

(a) MinBias

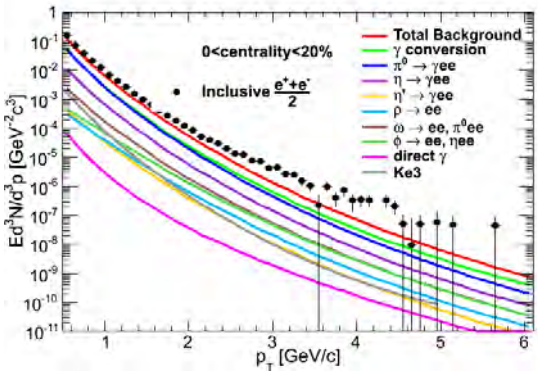

(b) Centrality 0-20%

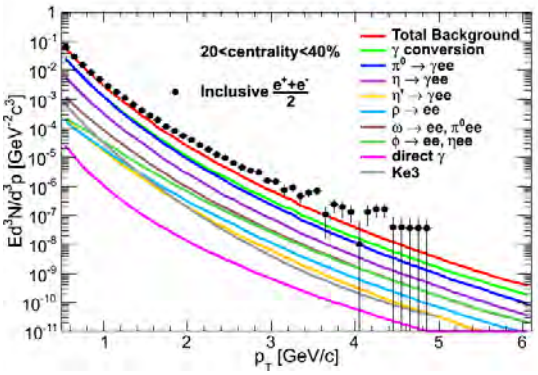

(c) Centrality 20-40%

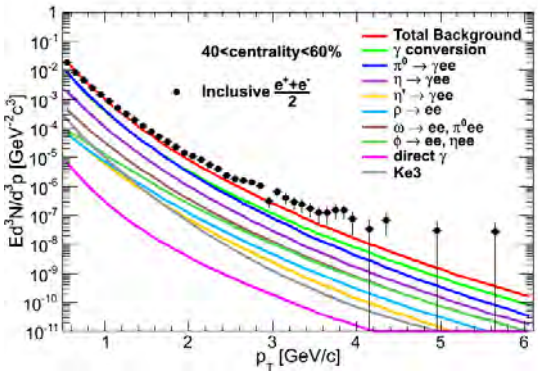

(d) Centrality 40-60%

Figure 4.6: The photonic electron cocktails as a function of p_T are obtained for four centrality bins. All photonic sources are included. The inclusive electron invariant yield is shown in black dot.

4.4 Photonic Electron v_2 Estimated by the Cocktail Method

Photonic electron v_2 can also be generated by EXODUS in the same procedure considering the particle angular distribution. The PHENIX π^0 v_2 measurement in Au + Au collisions at $\sqrt{s_{NN}}$ = 62.4 GeV using Run-10 data [49, 50] provides the information for EXODUS to generate photonic electron v_2. Fig. 4.7 shows the fit of π^0 v_2 for 0−20%, 20−40% and 40−60% centrality bins with Eq. 4.6. We include charged pion v_2 in the 0−20% centrality bin to get a better estimate of the pion v_2 at low p_T. The charged pion v_2 data is not available for 20−40% and 40−60% centrality bins. Considering our heavy flavor electron measurement starts from around ${p_T}^e$ = 1 GeV/c, unavailability of pion v_2 data at low p_T will not affect our analysis.

$$v_2 = a \times tan^{-1}(b \times p_T + c \times p_T^2) \times e^{-d \times p_T} \tag{4.6}$$

Unfortunately, there is no measurement of π^0 or $\pi^{\pm}$ v_2 for Min-Bias events in Au + Au collisions at $\sqrt{s_{NN}}$ = 62.4 GeV. Therefore, we are not able to estimate the photonic electron v_2 or extract the heavy flavor electron v_2 for Min-Bias events in our analysis.

Based on the measured π^0 v_2, the EXODUS simulates the π^0 distribution as a function of azimuth angle with respect to the reaction plane. The parent π^0 decays in EXODUS. The daughter electron distribution via the angle with respect to the reaction plane for each p_T bin is fitted with Eq. 3.12 to obtain the photonic electrons v_2.

For other light mesons, since the measurement of the v_2 of pions and kaons are the same as a function of transverse kinetic energy, we will assume the v_2 of other mesons also have the same value as a function of transverse kinetic energy. For other photonic sources (Ke3, direct photon,...), we assume their v_2 are negligible.

Fig. 4.8 shows the v_2 of photonic electron as a function of p_T for different centrality bins estimated by the EXODUS with the assumption discussed above.

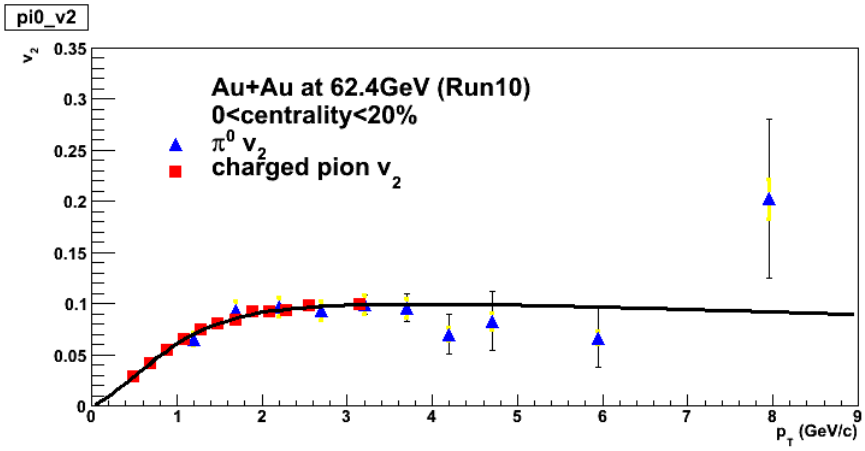

(a) Centrality 0-20%

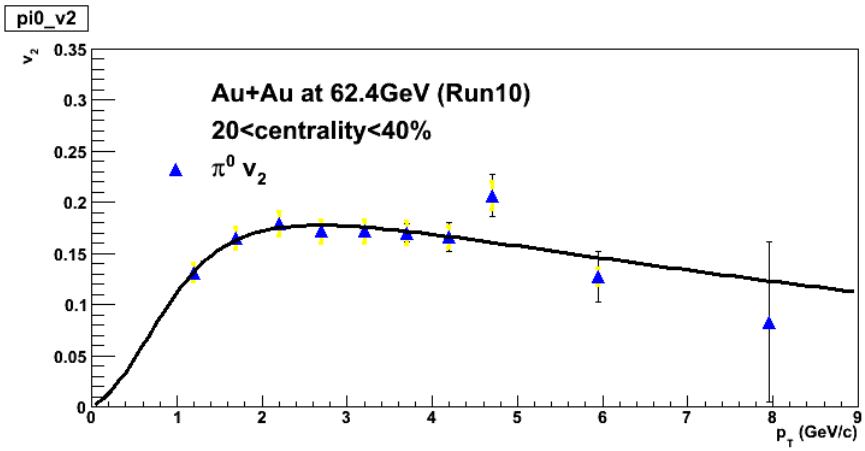

(b) Centrality 20-40%

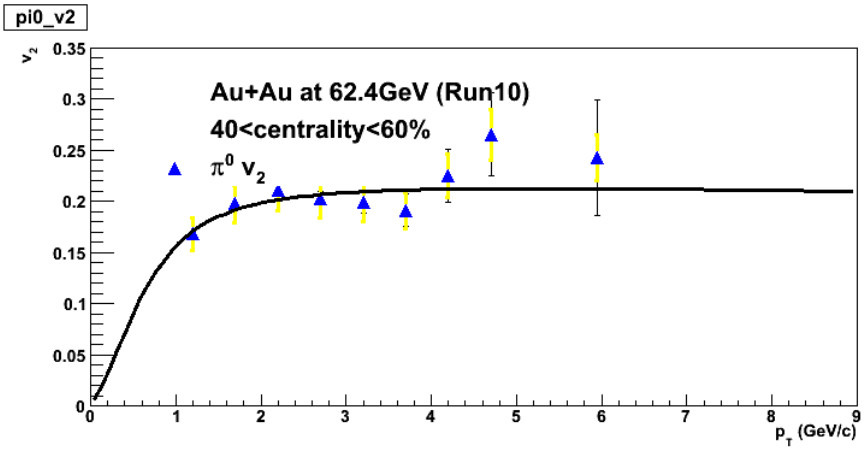

(c) Centrality 40-60%

Figure 4.7: The π^0 (or $\pi^{\pm}$) v_2 is fitted according to Eq. 4.6[49, 50].

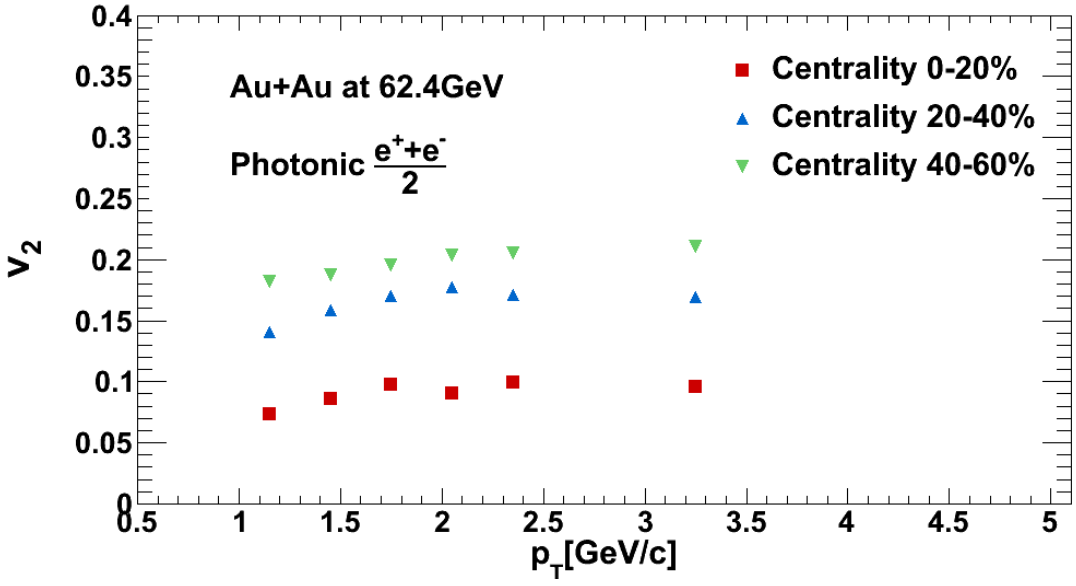

Figure 4.8: Photonic electron v_2 as a function of p_T (for 0−20%, 20−40%, 40−60% centrality bins)

CHAPTER 5. SYSTEMATIC ERROR EVALUATION

In this chapter, we will discuss how the systematic error is evaluated on the inclusive electron measurement and photonic electron background estimation.

5.1 Systematic Error Evaluation on Inclusive Electron Measurement

5.1.1 Systematic Errors from the Geometric Matching in the Simulation

It is very difficult for the PISA simulation to 100% match the real detector live/dead area. Any mismatching can cause systematic errors in the acceptance and reconstruction efficiency correction. We compare the yields in the two arms in the DC to evaluate how accurate the simulated detector geometry is. First, we integrate $dN/d\phi$ over the west arm of DC in both simulation and data. We scale the simulation and data in the west arm to make sure that they have the same integral. Then, we use the same normalization factor to scale the $dN/d\phi$ distribution in the east arm in simulation and data (Fig. 5.1). The difference between the integral of $dN/d\phi$ in the east arm in simulation and data is 2.6%. Previous PHENIX analyzers have determined the geometric matching systematic error as 4% and using integral could underestimate the difference between the simulation and data. Therefore, we assign 4 % syst. error for the geometric matching in the simulation.

5.1.2 Central Arm Electron Identification Cuts

As we discussed in Chapter 3, the efficiency of the electron cuts is obtained by a GEANT simulation of the PHENIX detector. The simulated subsystem response to electrons is not perfectly same as the reality, which brings systematic errors to our measurement when we correct the raw data with the eID efficiency obtained from the simulation. To evaluate the

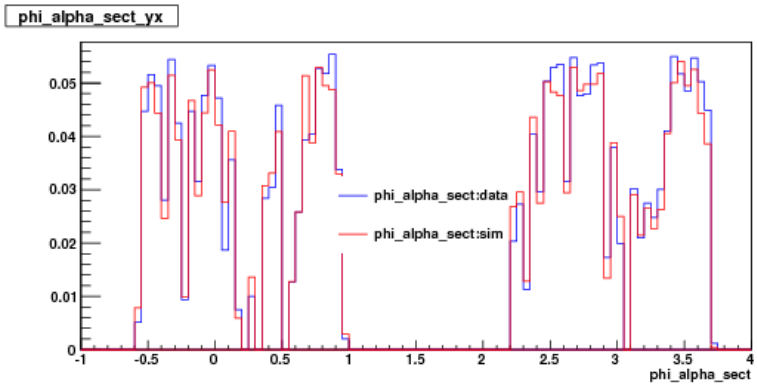

Figure 5.1: dN/dϕ distribution. Blue:real data; red: simulation

systematic uncertainty of the eID efficiency, we use 3 different sets of eID cuts (Table 5.1) and apply them independently to the data set. The procedure is as follows: the CA acceptance and efficiency factor and CA embedding efficiency factor are determined in the simulation using these 3 different sets of cuts. The raw spectrum of inclusive electron with each set of cuts is corrected with the corresponding efficiency. If the simulation can perfectly describe the efficiency loss in real data, the efficiency corrected spectrum for inclusive electron with different cuts should match each other. Otherwise the difference between the 3 spectra is a good estimation of the systematic errors in the eID efficiency evaluation. Fig. 5.2 shows that the difference between the inclusive electron yield from these 3 eID sets is around 6.7%. Therefore, a 7% systematic error is assigned to the inclusive electron spectrum due to the uncertainty of the eID efficiency.

Table 5.1: The sets of eID cuts to evaluate systematic errors on the Central Arm acc and eff correction

cut type	n0	dep	$\sqrt{emcsdphi^2 + emcsdz^2}$	prob
loose	>=3	>-3	<3	>0.02
standard	>=4	>-2	<3	>0.02
tight	>=5	>-2	<2.5	>0.1

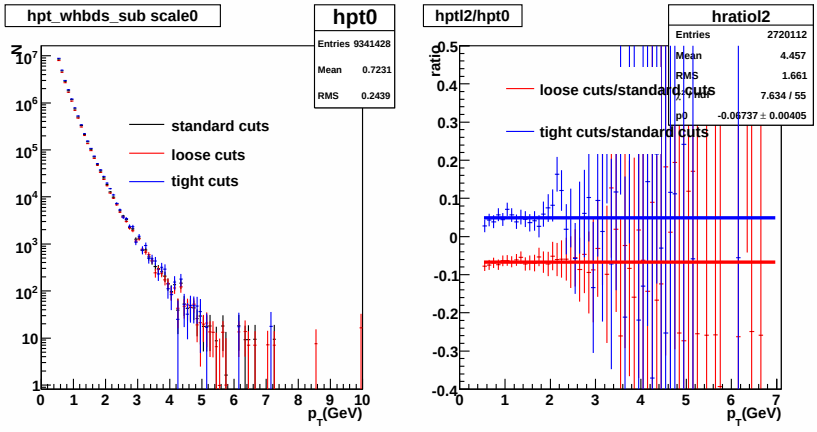

Figure 5.2: Inclusive electron spectra using different eID cuts (left) and the difference between loose/tight cuts and standard cuts (right)

5.1.3 HBD Swapping Normalization

The HBD swapping subtracts randomly matched background, including the hadron contaminations and the conversions that are generated at the HBD backplane. To make sure that the right amount of the background is subtracted from the data, the distribution of the swapped HBD charge is normalized to match the distribution of HBD charge around 0 (Fig. 3.4). The uncertainty in the normalization factor can cause systematic errors in the inclusive electron spectrum. By choosing different ranges of the HBD charge distribution to normalize the swapped distribution to the regular distribution, we obtain the inclusive electron spectrum with each normalization. The difference between the inclusive electron spectra estimate the systematic uncertainty from the HBD swapping normalization. Fig. 5.3 shows a 0.5% systematic error of HBD swapping normalization.

5.1.4 Additional Systematic Errors from HBD

An additional systematic error of 10% (Fig. 5.4) is assigned to the inclusive electron spectra due to the uncertainty in the HBD software to associate a CA track with HBD clusters. Currently, there are two independent HBD clusterizers developed in Stony Brook and Weitzmann. This analysis uses the Stony Brook version. The difference of inclusive electron yield between

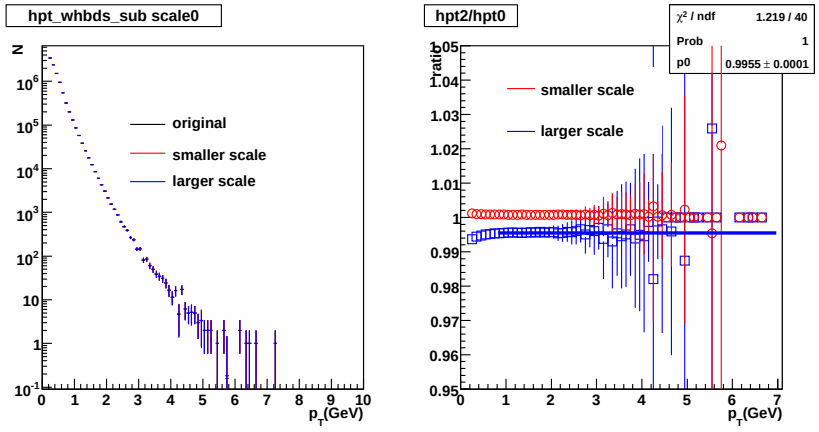

Figure 5.3: Inclusive electron spectra using different HBD swapping normalization (left) and the difference of spectra with different normalization factors.

this analysis and another independent analysis using the Weitzmann HBD clusterizer [51] with the same data set and very similar CA cuts are shown in Fig. 5.4.

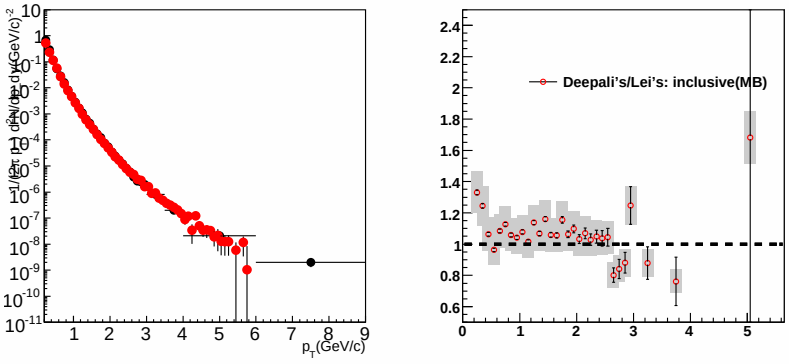

Figure 5.4: The left plots is the inclusive electron spectra in this analysis (red) and in Ref. [51] (black); The right plot is the ratio of inclusive electron spectra of Ref. [51] and this analysis)

5.1.5 Total Systematic Errors on Inclusive Electron Spectrum

The systematic errors we discussed in the previous sections are all part of the systematic errors on inclusive electron spectrum. They are independent of each other. Each contribution is added in quadrature to obtain the total systematic error (Table 5.2).

Table 5.2: Total syst. error on inclusive e spectrum

Source	Systematic error
Geometric matching in sim and data	4%
CA eID cuts efficiency	7%
HBD swapping normalization	0.5%
HBD clusterizer	10%
Total syst. error on inclusive e spectrum	14%

5.2 Systematic Error on the Photonic Cocktail

π^0 Dalitz decays and conversions of photons from $\pi^0 \rightarrow \gamma + \gamma$ are the two major sources of the photonic electrons. In addition, most of the cocktail ingredients directly or indirectly come from the measured π^0 spectrum. Hence the systematic uncertainty of the π^0 spectrum becomes the main source of the systematic errors in the cocktail method. To estimate the systematic error from π^0 measurement, we move every data point of the π^0 spectra up or down by their systematic errors, which are mainly from energy scale and particle identification efficiency correction in the π^0 measurement [31], then fit the modified spectra with the Hagedorn function and use the new parameters in EXODUS to generate new cocktails. The systematic errors are determined by the difference between the electron spectra from π^0 Dalitz decays after moving the π^0 data points up (or down) and the spectra generated with the original π^0 data. Table 5.3 and 5.3 list the new parameters of the Hagedorn function after moving the π^0 data points by the systematic errors.

Table 5.3: Fit parameters for the π^0 invariant yield with all data points moved up by the systematic uncertainties according to the Hagedorn function Eq. 4.1

Centrality	**c**	**a**	**b**	p_0	**n**
Min-Bias	899.01	0.294213	0.0733472	0.995163	11.172
0-20%	1497.1	0.342271	0.104253	0.977757	10.8929
20-40%	1076.6	0.273907	0.0498505	1.06702	11.4965
40-60%	399.524	0.298351	0.0602318	0.992423	10.935

For other light mesons, we determine the systematic error on their contribution to the cocktail by scaling the central value of the decayed electron spectrum is scaled up or down by

Table 5.4: Fit parameters for the π^0 invariant yield with all data points moved down by the systematic uncertainties according to the Hagedorn function Eq. 4.1

Centrality	**c**	**a**	**b**	p_0	**n**
Min-Bias	451.758	0.363122	0.0534743	1.03945	11.2015
0-20%	895.733	0.396392	0.0922255	1.00733	10.8914
20-40%	555.675	0.324748	0.0256087	1.13784	11.6643
40-60%	204.382	0.365561	0.0395359	1.03829	10.9754

the systematic uncertainty of the meson to pion ratio listed below:

- $\eta/\pi = 0.48 \pm 0.03$ [44];
- $\phi/\pi = 1.00 \pm 0.30$ [45];
- $\omega/\pi = 0.90 \pm 0.06$ [46];
- $\eta'/\pi = 0.25 \pm 0.075$ [46];
- $\rho/\pi = 0.40 \pm 0.12$ [46];

Table 5.5 summarizes all the assigned systematic errors in the photonic background analysis. Each contribution of the systematic uncertainties is added in quadrature. There is no evidence that the the upper and lower systematic uncertainties of the cocktail method should be different. Therefore, we also average the upper and lower uncertainties to obtain the total systematic uncertainty on the photonic electron cocktail. As shown in Fig. 5.5, the total systematic error is around $10 - 15$ %. These p_T dependent systematic errors are applied to data.

Table 5.5: Summary of the assigned systematic errors for each photonic source

Source	**Systematic error (%)**
π^0	according to the systematic uncertainty of the π^0 measurement
Other light mesons	according to the systematic uncertainty of the meson to π^0 ratio
R_{CD}	10% for the material and 10% for the fit of R_{CD}
Ke3	50%
Direct photon	20%

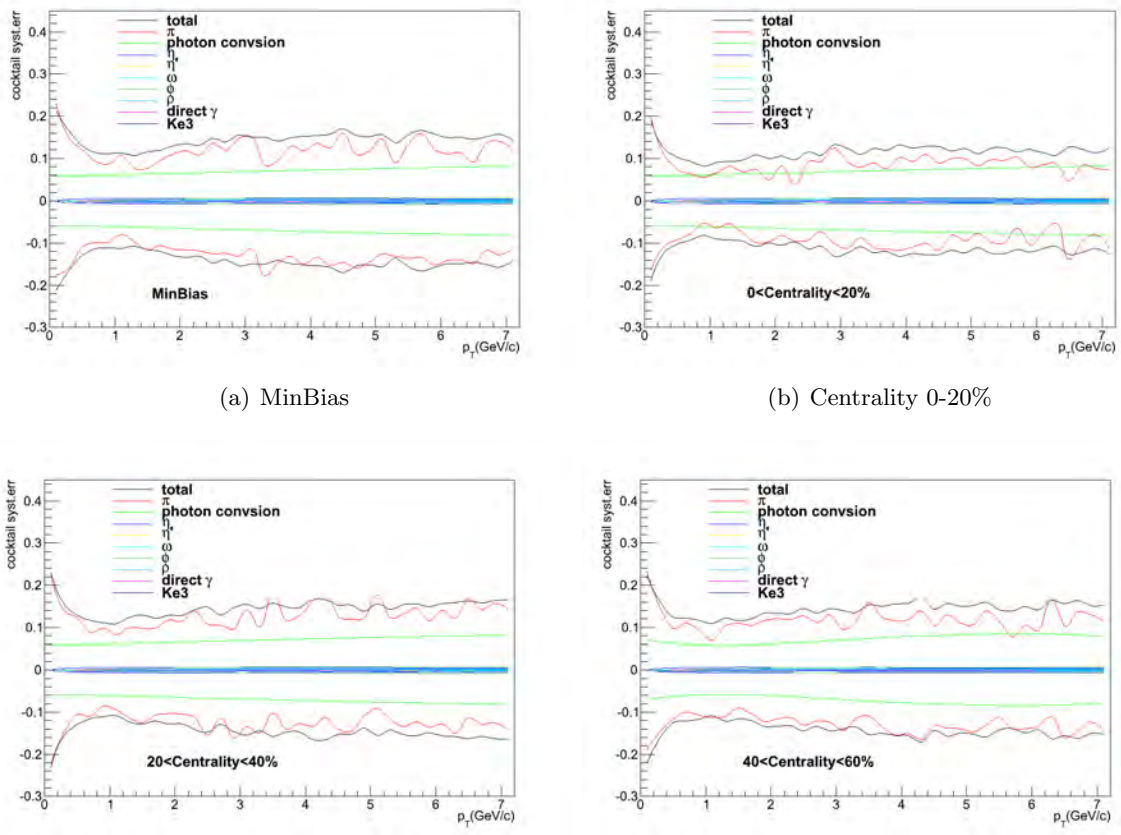

(a) MinBias

(b) Centrality 0-20%

(c) Centrality 20-40%

(d) Centrality 40-60%

Figure 5.5: Cocktail systematic errors

5.3 Systematic Error from the HBD Charge Cut

The systematic errors from the HBD detector simulation and the HBD charge cut contribute to both the inclusive electron measurement and the photonic electron background estimation. This systematic error comes from the assumption that the simulation can accurately reproduce the HBD response in reality. In order to determine the systematic error from the HBD cut, similar to how the systematic error of CA eID cuts is studied, we use 3 different sets of HBD cuts (Table 5.6) to to study the difference in the heavy flavor yield with each set of HBD cuts. The left panel in Fig. 5.6 shows the heavy flavor electron invariant yield with these 3 sets of HBD cuts. The right panel in Fig. 5.6 shows the ratio of the yield with loose (or tight) HBD

Table 5.6: The sets of HBD cuts to evaluate systematic errors from the HBD charge cuts

HBD cuts type	
loose	$7 < hbdq < 45$
standard	$10 < hbdq < 35$
tight	$10 < hbdq < 30$

cuts to the yield with standard cuts. The heavy flavor electron yields with different HBD cuts are relatively stable and the difference is within 10%. Based on Fig. 5.6, we assign a systematic error of 10% on the heavy flavor electron yield for ${p_T}^e < 1.5 GeV/c$ and a systematic error of 5% on the heavy flavor electron yield for $1.5 < {p_T}^e < 6 GeV/c$.

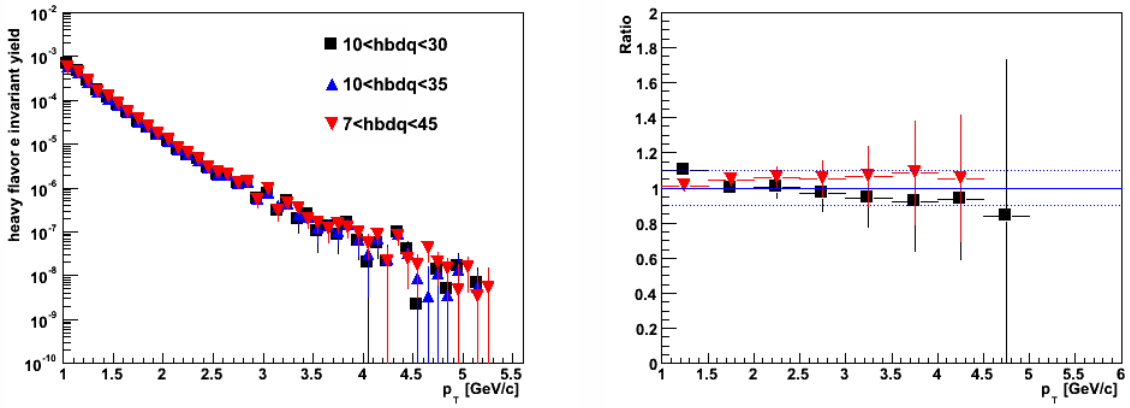

Figure 5.6: The left panel is the heavy flavor electron invariant yield with loose (black), standard (blue) and tight (red) HBD cuts. The right panel shows the ratio of the heavy flavor electron yield with loose (or tight) HBD cuts to the yield with standard cuts in black squre (or red triangle).

5.4 Systematic Error on v_2

A systematic error of 5% is assigned to the inclusive electron v_2 due to the reaction plane resolution. Similarly, a systematic error of 5% is assigned to the v_2 of photonic electron due to the reaction plane resolution. Because v_2 of both inclusive electron and π^0 are calculated from

the same reaction plane, this systematic error is correlated for the inclusive electron v_2 and the photonic electron v_2.

In addition, in the Run-4 Au + Au $\sqrt{s_{_{NN}}} = 200$ GeV analysis, it was found that a systematic uncertainty of 4% is caused by the uncertainty of the relative ratio of different photonic electron sources [9, 10]. Because the procedure to get the photonic v_2 and the relative ratio of each photonic source are similar between our analysis and the Run-4 analysis, we also assign a systematic error of 4% to the photonic v_2 due to the mixture of different sources. This systematic error of 4% is independent to the systematic error fromhbd the reaction plane resolution.

CHAPTER 6. HEAVY FLAVOR ELECTRON RESULTS AND DISCUSSION

6.1 Heavy Flavor Electron Invariant Yield

To extract the invariant yield of heavy flavor electrons, the photonic electron background is subtracted from the invariant yield of inclusive electrons for each centrality bin. Fig. 6.1 shows the invariant yield of heavy flavor electrons as a function of p_T in 4 different centrality bins. The error bars represent the statistical errors in the heavy flavor electron measurement, while the boxes display the systematic errors. The systematic errors on the heavy flavor electron yield is calculated by adding the systematic errors on inclusive electron yield and the systematic errors on photonic electron cocktail in quadrature.

Fig. 6.2 shows the signal to background ratio, which is also known as the non-photonic (heavy flavor electrons) to photonic ratio R_{np} (Eq. 6.1), in MB events. R_{np} increases with p_T. At low p_T, the inclusive electrons are almost all from the photonic sources. At high p_T, electrons from heavy flavor meson decays start to dominate the inclusive electron yield.

$$R_{np} = \frac{N_{hf}}{N_{photonic}} \tag{6.1}$$

Where N_{hf} is the yield of heavy flavor electrons, $N_{photonic}$ is the yield of photonic electrons.

By dividing the invariant yield of the heavy flavor electrons by $< N_{coll} >$, we are able to study the invariant yield of the heavy flavor electrons per binary collision for different centrality bins. Fig. 6.3 compares the invariant yield of the heavy flavor electrons per binary collision in 0-20%, 20-40%, 40-60% centrality bins and MB data in Au + Au collisions at $\sqrt{s_{NN}} = 62.4$ GeV side by side. The invariant cross section of heavy flavor electrons in p + p collisions at $\sqrt{s_{NN}} = 62.2$ GeV in the ISR experiment [52] is scaled by $\sigma_{pp} = 37mb$ and plotted on the 5th

panel of Fig. 6.3. The FONNL prediction [53] in the red curve is also shown in each panel. In Au + Au collisions at $\sqrt{s_{NN}}$ = 62.4 GeV, the yield of heavy flavor electron per binary collision is higher than the ISR results in p + p collisions, while the ISR p + p results are consistent with the higher limit of the FONNL prediction.

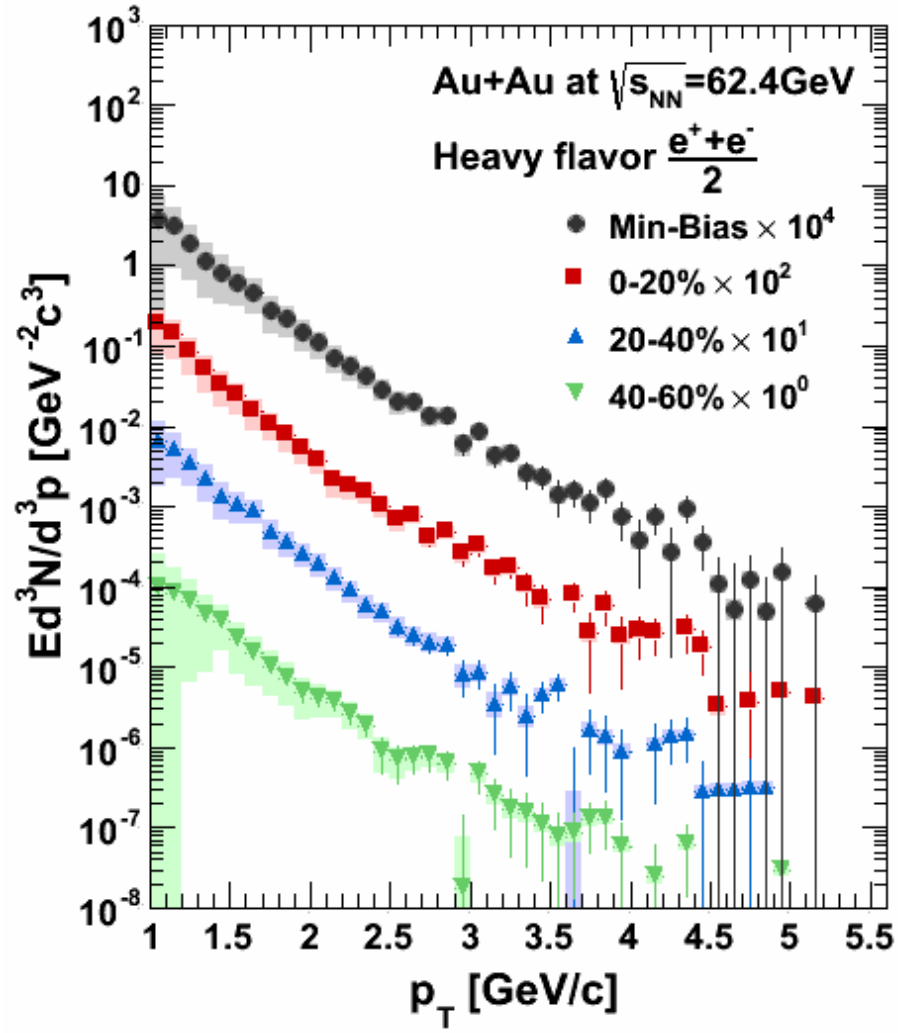

Figure 6.1: (Color online) Invariant yield of heavy flavor electrons measured in Au + Au collisions at $\sqrt{s_{NN}}$ = 62.4 GeV for different centrality bins. The yields are scaled by powers of 10 for clarity. The statistical (systematic)uncertainties are showed in the uncertainty bars (boxes).

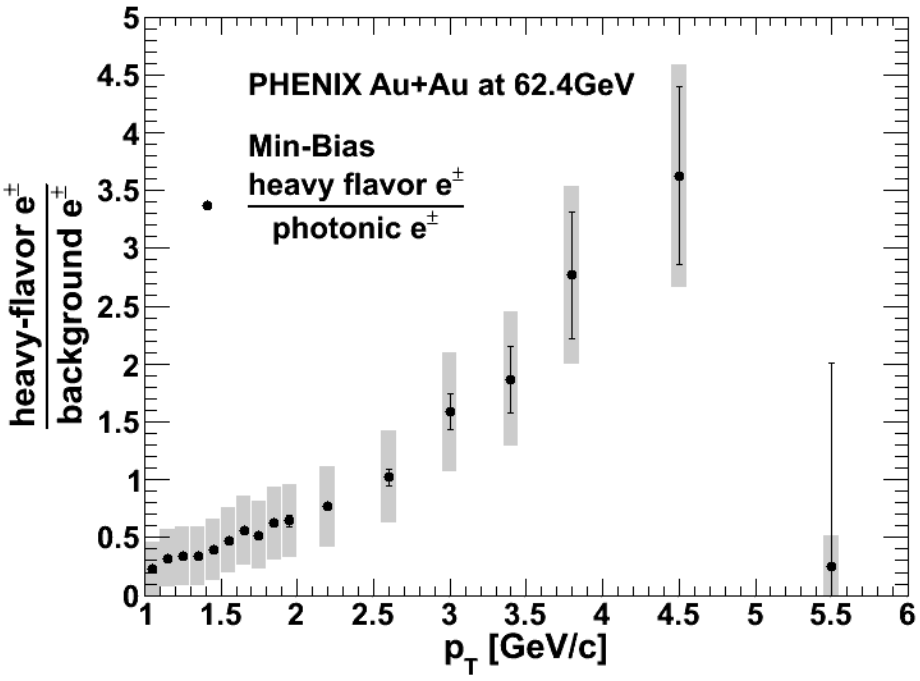

Figure 6.2: (Color online) Ratio of the heavy flavor electrons (signal) to photonic electrons (background) in Au + Au collisions at $\sqrt{s_{NN}} = 62.4$ GeV for Min-Bias events in this analysis.

To study the modification of the yield of the heavy flavor electrons in Au + Au collisions at $\sqrt{s_{NN}} = 62.4$ GeV, the invariant yield per binary collision of heavy flavor electrons is integrated to three p_T bins as shown in Fig. 6.4. As a comparison, the same integrals for π^0 are also calculated (data from Ref.[31]). In Au + Au collisions at $\sqrt{s_{NN}} = 62.4$ GeV, π^0 shows a larger suppression from the peripheral collisions to the central collisions in all the three p_T bins, which may because of the energy loss of light quarks when interacting with the medium. However, the modification pattern for heavy flavor electrons in Au + Au collisions at this low energy is different from π^0. In fact, at low p_T ($1.5 < p_T < 2.5 GeV/c$), an enhancement of the heavy flavor electron yield is observed in the 20-40% and 40-60% centrality bins. Only at high p_T ($3.5 < p_T < 5 GeV/c$), are there hints of suppression in the heavy flavor electron yield in central events. The possibility of two mechanisms being at play is discussed in the next section. Initial, Cronin-like scattering could increase the yield of heavy-flavor at low to moderate p_T and as the collisions become more central, energy loss at high p_T would compete to suppress the spectra.

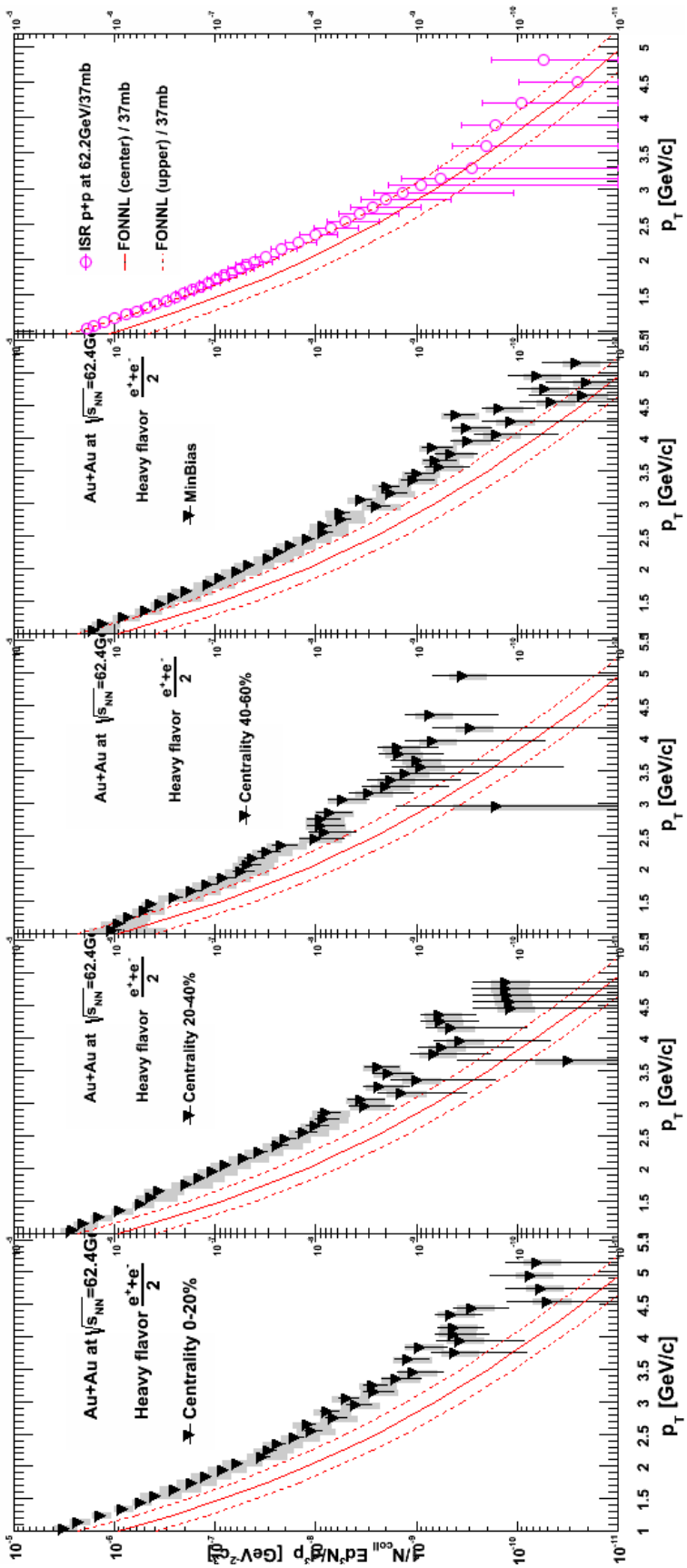

Figure 6.3: (Color online) Invariant yield of heavy flavor electrons per binary collision in Au + Au collisions at $\sqrt{s_{NN}}$ = 62.4 GeV for different centrality bins and in p + p collisions at $\sqrt{s_{NN}}$ = 62.2 GeV measured in ISR experiment (right 1^{st} panel) [52]. FONNL center value (red solid line) and upper, lower limits (red dash lines) [53] are plotted in each panel as a comparison. The ISR p + p result is consistent with the FONNL upper limit.

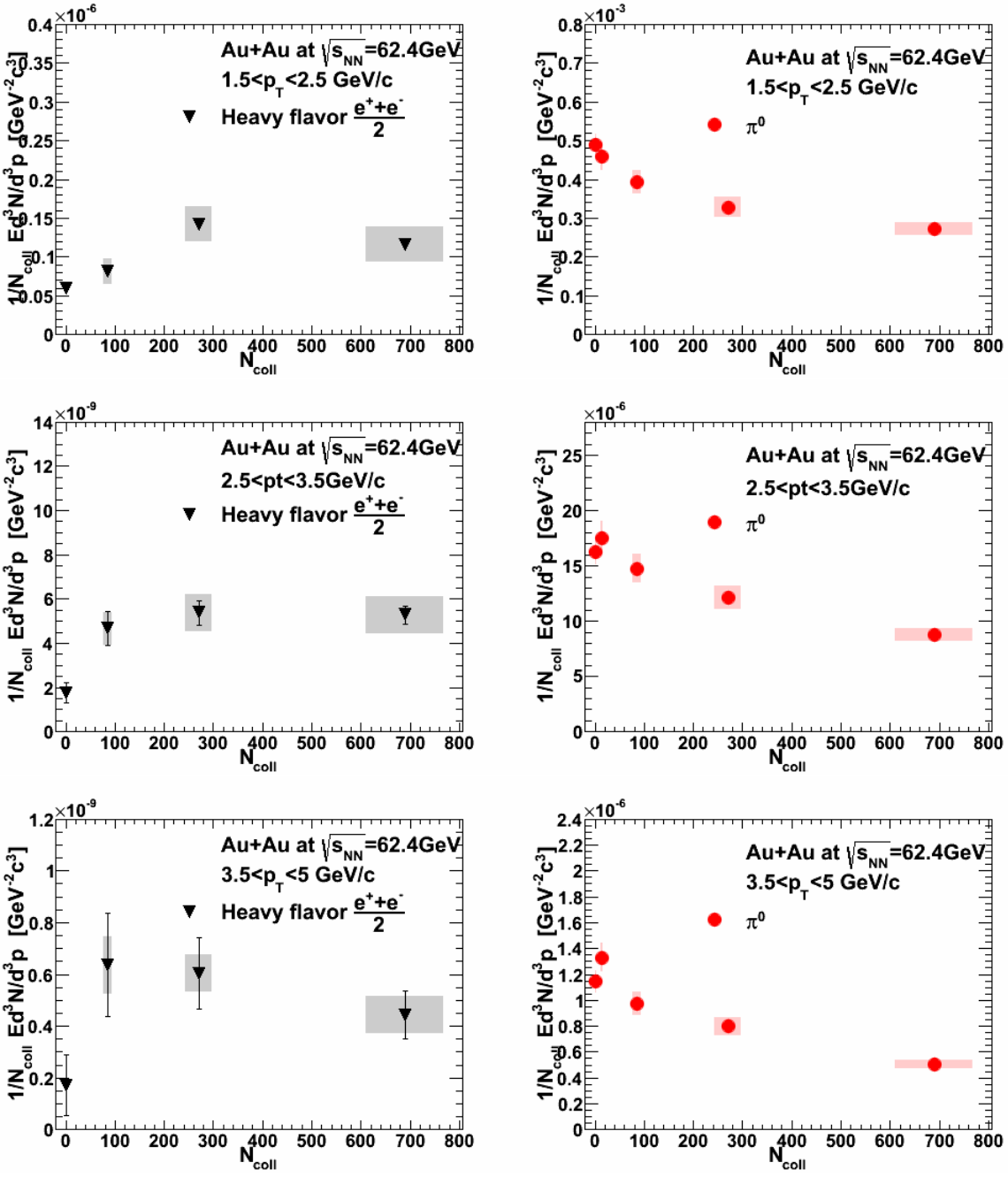

Figure 6.4: (Color online) Integrated invariant yield per binary collision vs $N_{\rm coll}$ for heavy flavor electrons (π^0) in the $p_T{}^e$ range $1.5 < p_T < 2.5$ GeV/c (upper two panels) and $3 < p_T < 5$ GeV/c (lower two panels) in Au + Au collisions at $\sqrt{s_{NN}} = 62.4$ GeV. π^0 shows a clear suppression for central events with large $N_{\rm coll}$ (right panels). Heavy flavor electrons (left panels) show different suppression patterns for low p_T and high p_T.

Another method to study the change of the heavy flavor electron yield from peripheral to central collisions is to calculate $R_{\rm CP}$. $R_{\rm CP}$ is given by Eq. 6.2. In our analysis, the yield from 0-20% centrality bin and 40-60% centrality bin are used for $R_{\rm CP}$.

$$R_{\rm CP} = \frac{< N_{coll}^{peripheral} > \times dN^{e}_{AuAu,central}/dp_T}{< N_{coll}^{central} > \times dN^{e}_{AuAu,peripheral}/dp_T} \tag{6.2}$$

Fig. 6.5 shows enhancement in $R_{\rm CP}$ for heavy flavor electrons in 0-20% centrality events compared to 40-60% centrality events for $1 < p_T < 3GeV/c$, and possible suppression at high p_T ($p_T > 3GeV/c$).

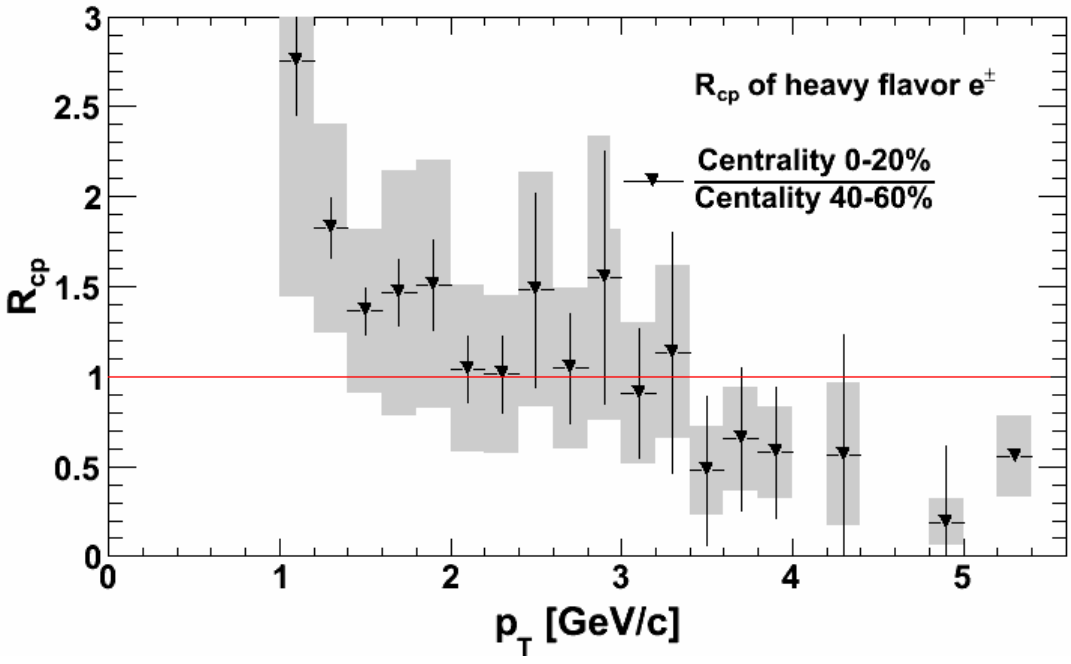

Figure 6.5: (Color online) Heavy flavor electron $R_{\rm CP}$ between centrality 0-20% and 40-60% in Au + Au collisions at $\sqrt{s_{_{NN}}} = 62.4$ GeV.

6.2 Heavy Flavor Electron v_2

Heavy flavor electron v_2 can be calculated from inclusive electron v_2, photonic electron v_2 and R_{np}. The following steps show how the equation for heavy flavor electron v_2 is derived.

First, the inclusive electron yield with respect to the reaction plane angle is the sum of the heavy flavor electron yield and photonic electron yield:

$$\frac{dN^{inc}}{d\phi} = \frac{dN^{hf}}{d\phi} + \frac{dN^{pho}}{d\phi} \tag{6.3}$$

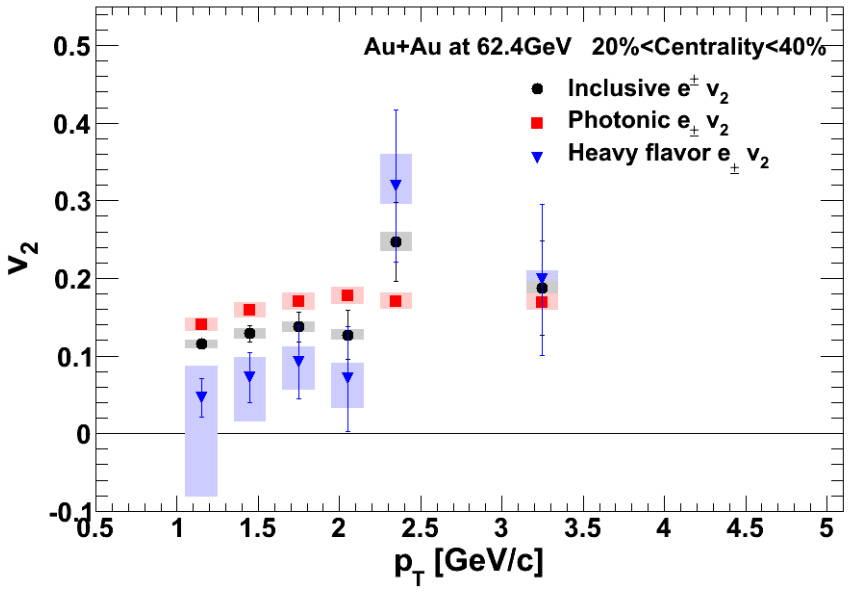

Figure 6.6: (Color online) Inclusive (black) , photonic (red) and heavy flavor (blue) electron v_2 in Au + Au collisions at $\sqrt{s_{NN}}$ = 62.4 GeV for centrality 20-40% events.

From the definition of v_2 (Eq. 3.12), it is easy to obtain:

$$N_0^{inc}(1+2v_2^{inc}\cos(2(\phi-\Phi_{RP}))) = N_0^{hf}(1+2v_2^{hf}\cos(2(\phi-\Phi_{RP})))+N_0^{pho}(1+2v_2^{pho}\cos(2(\phi-\Phi_{RP}))) \tag{6.4}$$

It can be simplified to:

$$v_2^{hf} = \frac{N_0^{inc}v_2^{inc} - N_0^{pho}v_2^{pho}}{N_0^{hf}} \tag{6.5}$$

Then, we can obtain:

$$v_2^{hf} = v_2^{inc}(1+\frac{1}{R_{np}}) - v_2^{pho}\frac{1}{R_{np}}, \tag{6.6}$$

Where,

$$R_{np} = \frac{N_{hf}}{N_{photonic}} \tag{6.7}$$

In additional, the error on the heavy flavor electron v_2 is calculated with Eq. 6.8

$$(\triangle v_2^{hf})^2 = (\triangle v_2^{inc})^2(1 + \frac{1}{R_{np}})^2 + (\triangle v_2^{pho})^2 \frac{1}{{R_{np}}^2} + (\sum_{n=1}^{\infty} \frac{(- \triangle R_{np})^n}{{R_{np}}^{n+1}})^2 (v_2^{inc} - v_2^{pho})^2 \tag{6.8}$$

Where $\triangle v_2^{inc}$ is the error on the inclusive electron v_2, $\triangle v_2^{pho}$ is the error on the photonic electron v_2 and $\triangle R_{np}$ is the error on the R_{np}.

Fig. 6.6 shows the v_2 for inclusive, photonic and heavy flavor electrons in 20-40% centrality bin as an example of how v_2 of heavy flavor electron is calculated. Fig. 6.7 shows the v_2 of heavy flavor electrons in Au + Au collisions at $\sqrt{s_{NN}}$ = 62.4 GeV in 0-20%, 20-40% and 40-60% centrality bins. In 0-20% centrality bin, v_2 of heavy flavor electrons is small because the overlap of the collided nuclei in geometry is not very asymmetric, the flow effect is suppose to be small in central collisions. In 20-40% centrality bin, an none zero v_2 of heavy flavor electrons is observed for $p_T > 1.5$ GeV/c which may indicate that the heavy quarks flow at this low collision energy in Au + Au collisions. In 40-60% centrality bin, the error bar of the v_2 of heavy flavor electrons is large due to small statistics, so that we can not draw a clear conclusion in this centrality bin.

To study the elliptic flow as a function of centrality, we first scale v_2 with the initial geometry eccentricity ϵ. The eccentricity ϵ, represents the ellipticity of the participant nucleons in the collision, is defined as:

$$\epsilon = \frac{\langle y^2 \rangle - \langle x^2 \rangle}{\langle y^2 \rangle + \langle x^2 \rangle} \tag{6.9}$$

Where x and y are the position of the nucleons that participant the collision. ϵ can be calculated in the Glauber Monte Carlo calculation [54]. Table 6.1 shows the ϵ in Au + Au at $\sqrt{s_{NN}}$ = 62.4 GeV for various centrality bins.

By scaling v_2 with ϵ, the centrality, or ellipticity dependence does no longer exist in v_2. Fig. 6.8 plots heavy flavor electrons and π^0 v_2 [49] scaled by the eccentricity as a function of

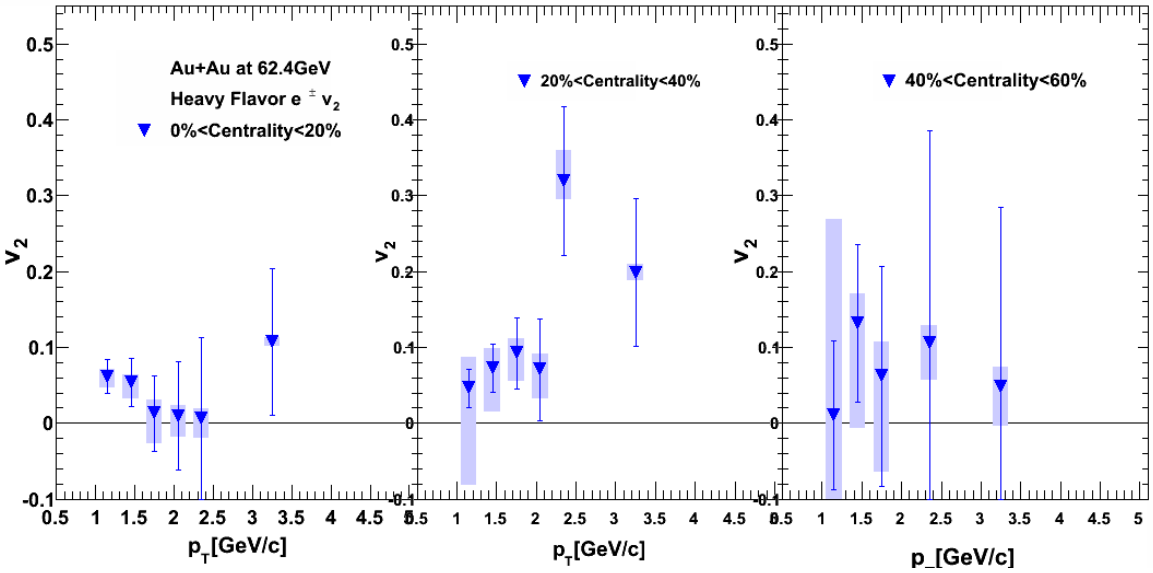

Figure 6.7: (Color online) Heavy flavor electron v_2 in Au + Au collisions at $\sqrt{s_{NN}}$ = 62.4 GeV for 0-20% (left), 20-40% (middle) and 40-60% (right) centrality bins.

$N_{\rm coll}$ in Au + Au collisions at $\sqrt{s_{NN}}$ = 62.4 GeV for 1.0<p_T <1.3 GeV/c and 1.3<p_T <2.5 GeV/c. The heavy flavor v_2, in general, is smaller than the π^0 v_2, which may indicate that D mesons are close to thermalization but not completely thermalized in the medium, or D mesons freeze out earlier in the medium comparing to light mesons.

The v_2 of heavy flavor electrons and π^0 for $1.3 < p_T < 2.5 GeV/c$ in Au + Au collisions as a function of collision energy is compared in Fig. 6.9 for 0<centrality<20% and

Table 6.1: Eccentricity ϵ in Au + Au collisions at $\sqrt{s_{NN}}$ = 62.4 GeV

Centrality (%)	**Participant ϵ**	**Systematic errors**
0-10	0.107	0.023
10-20	0.207	0.022
20-30	0.292	0.020
30-40	0.365	0.018
40-50	0.431	0.013
50-60	0.498	0.010
60-70	0.573	0.008
70-80	0.678	0.011
80-90	0.740	0.022

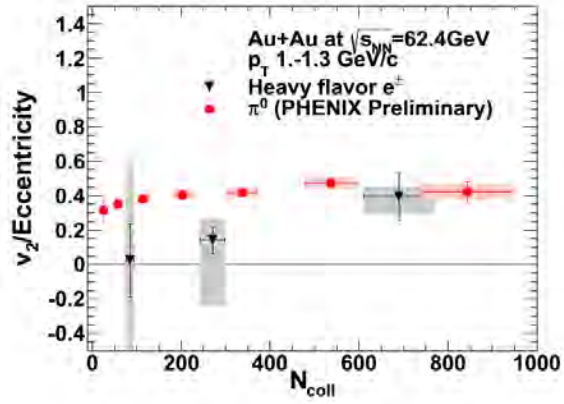

(a) 1.0<p_T <1.3 GeV/c

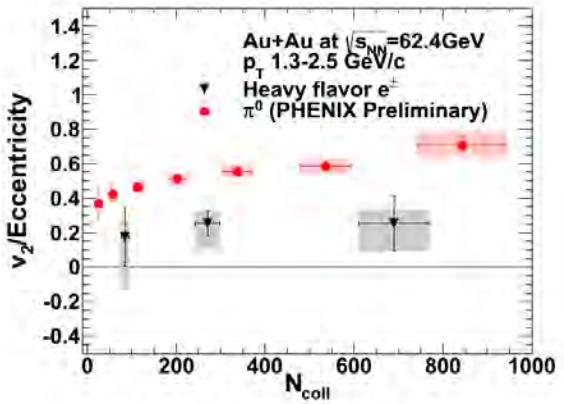

(b) 1.3<p_T <2.5 GeV/c

Figure 6.8: (Color online) Heavy flavor electrons and π^0 v_2 scaled by the eccentricity as a function of $N_{\rm coll}$ in Au + Au collisions at $\sqrt{s_{NN}}$ = 62.4 GeV for two p_T ranges.

20<centrality<40% events. The plots shows that both heavy quarks and light quarks flow in Au + Au at $\sqrt{s_{NN}}$ = 62.4 GeV and 200 GeV. However, the flow of heavy flavor electrons is smaller than π^0 at both collision energies. When the collision energy goes from 200 GeV to 62.4 GeV, the flow of heavy flavor electrons remains consistent or becomes smaller, while the flow of π^0 is almost consistent for these two energies, which indicates that the effects of flow and energy loss are different for heavy quarks and light quarks. In summary, the interaction between heavy quarks and the medium at 62.4 GeV is similar to or smaller than the interaction at 200 GeV.

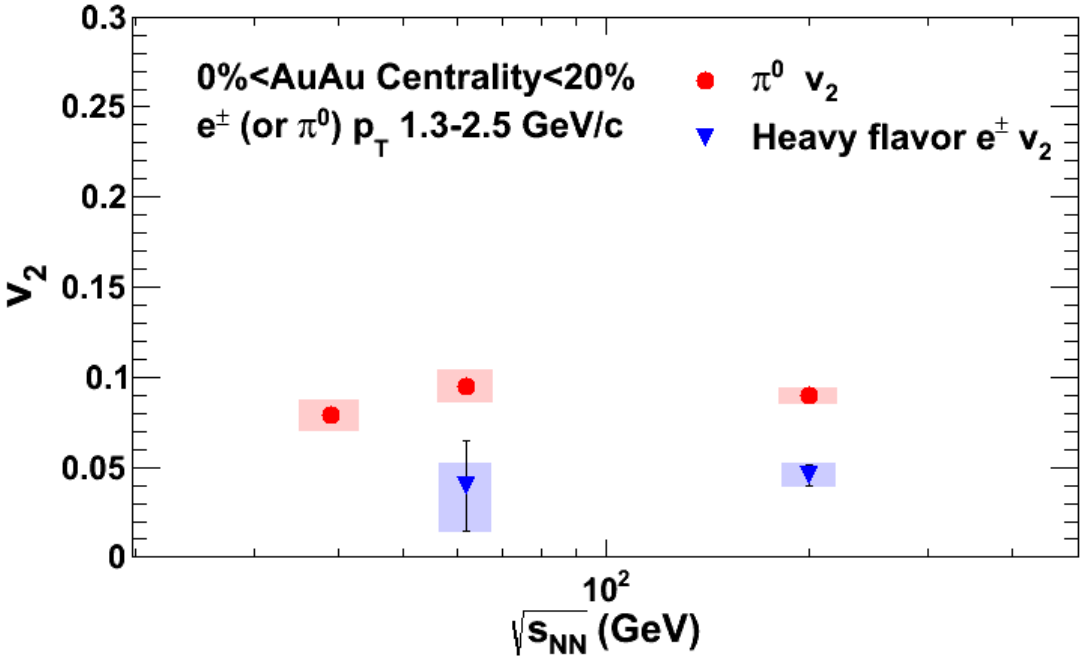

(a) 0<centrality<20%

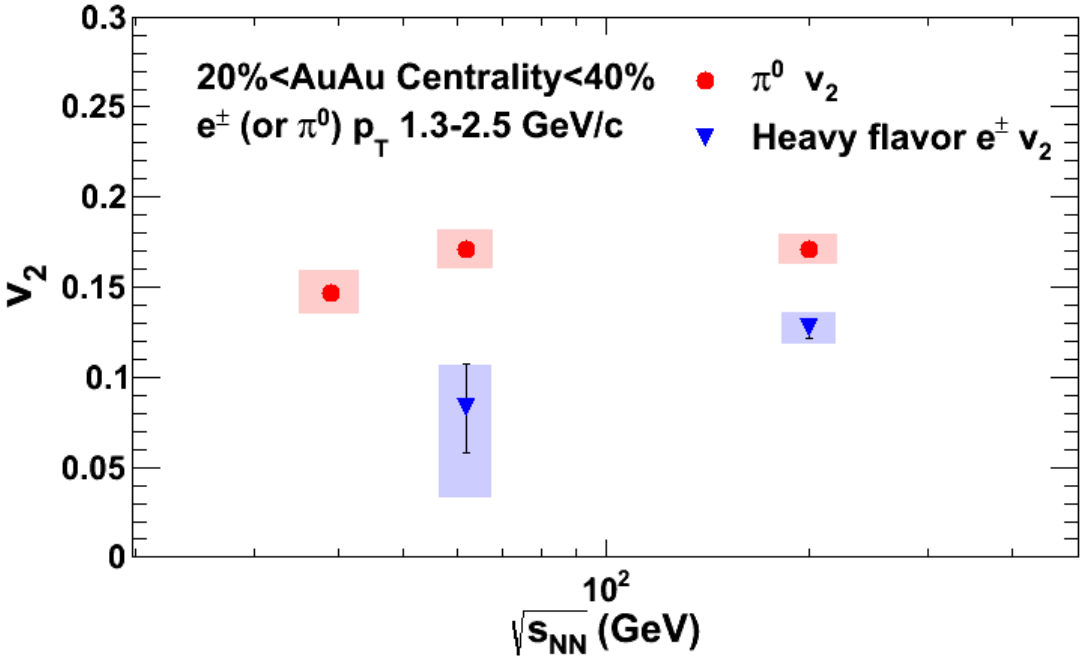

(b) 20<centrality<40%

Figure 6.9: (Color online) v_2 of heavy flavor electrons and π^0 in the p_T range $1.3 < p_T < 2.5$ GeV/c in Au + Au collisions as a function of collision energy.

6.3 Discussion

In this section, we try to interpret our results with Cronin effect, blast wave and the energy loss model.

6.3.1 Comparison to the Energy Loss Based Model

Fig. 6.10 shows the comparison between our results and the theoretical curves calculated in a energy loss based model [55]. The theoretical predictions are calculated in the framework of a modified Langevin equation [56] coupled to a (2+1)-dimensional viscous hydrodynamic model [57]. The classical Langevin approach is improved such that both quasi-elastic scattering and medium-induced gluon radiation are incorporated for heavy quark energy loss inside the QGP medium. Before their Langevin evolution, heavy quarks are initialized with a leading order perturbative QCD calculation [58] coupled to the nucleus parton distribution function provided by Ref. [59]; and after traversing the QGP, they hadronize into heavy mesons according to a hybrid model of instantaneous coalescence [60] plus Pythia 6.4 [61] fragmentation. Two initial conditions, MC-Glauber [62] and KLN-CGC [63], for the hydrodynamic model are compared here and the corresponding impact on the final state heavy flavor spectra is displayed.

As shown in Fig. 6.10(b), given the large uncertainties in the $R_{\rm CP}$, the measured value is consistent with the theoretical prediction for $3 < p_T < 5 GeV/c$. At $p_T < 2$ GeV/c, the theory does not reproduce the data hence this suggests the presence of another mechanism, e.g. multiple initial scattering or thermal expansion of the medium. Considering collisional and radiational energy loss, the v_2 predictions in the model show non-zero flows for electrons from heavy flavor mesons (Fig. 6.10(b)), which are mainly D mesons at $p_T < 5$ GeV. However, the prediction of this energy loss model is systematically lower than the measured v_2. It is not clear what the short-coming is. Possibilities might include the charm-to-bottom ratio in its initial production and the properties of the QGP profiles [64]. The future measurement of heavy flavor v_2 in d + Au may help to constrain the initial state. With the Silicon Vertex Tracker (VTX), a new upgrade of the PHENIX detector system, it is possible to measure v_2 of D meson and v_2 of B meson separately, which will help to constrain the charm-to-bottom ratio in theory model

and provide better agreement between theoretical calculations and experimental observations.

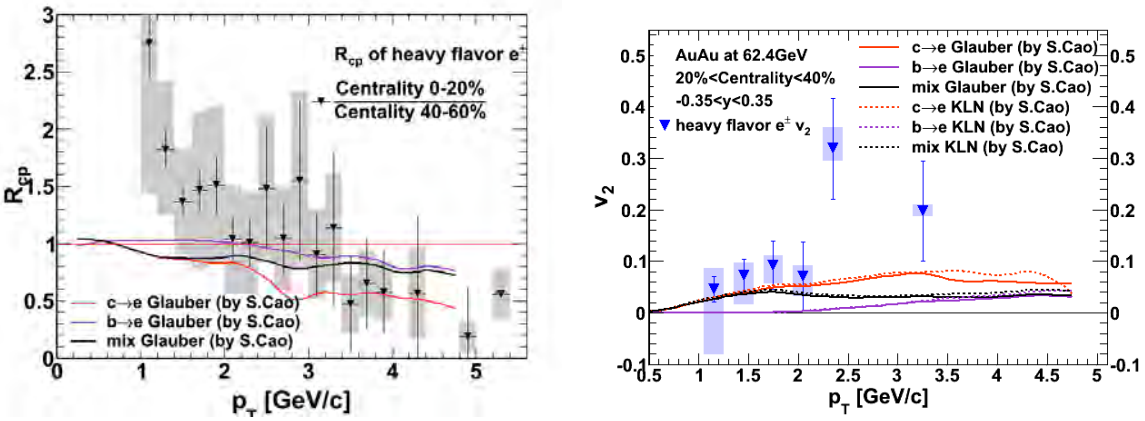

(a) $R_{\rm CP}$ (b) v_2

Figure 6.10: (Color online) Heavy flavor electron (a) $R_{\rm CP}$ and (b) v_2 in Au + Au collisions at $\sqrt{s_{NN}}$ = 62.4 GeV (blue triangle) compare with multiple theory curves.

6.3.2 Data Systematics

The enhancement observed in the integrated yield per binary collision (Fig. 6.4) and $R_{\rm CP}$ (Fig. 6.5) of heavy flavor electrons in Au + Au collisions at $\sqrt{s_{NN}}$ = 62.4 GeV cannot be explained by the energy loss theory only. Recently, measurements of heavy flavor electron yield in d + Au [20] and Cu + Cu [65] collisions at $\sqrt{s_{NN}}$ = 200 GeV indicate that Cronin effect in the initial state causes an enhancement at the low to moderate p_T. Fig. 6.11 shows the integrated invariant yield per binary collision of heavy flavor electrons in three p_T bins for Au + Au and d + Au collisions at $\sqrt{s_{NN}}$ = 200 GeV. The data from Ref. [10] and [20] are used to make these plots. In all three p_T ranges, from p + p to d + Au to Au + Au collisions, as $N_{\rm coll}$ increases, the energy loss suppression seems to compete with the Cronin enhancement and makes a peak in the yield of the heavy flavor electrons per $N_{\rm coll}$ at $N_{\rm coll}$ around 10-20.

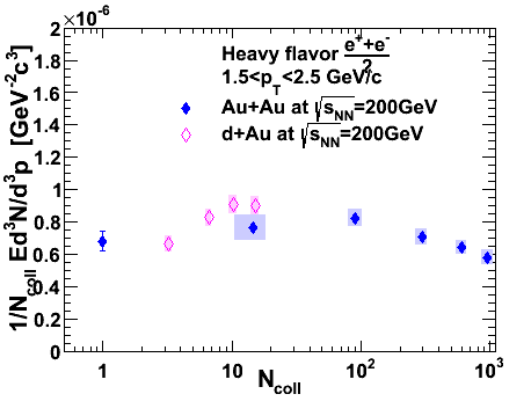

(a) p_T 1.5-2.5 GeV/C

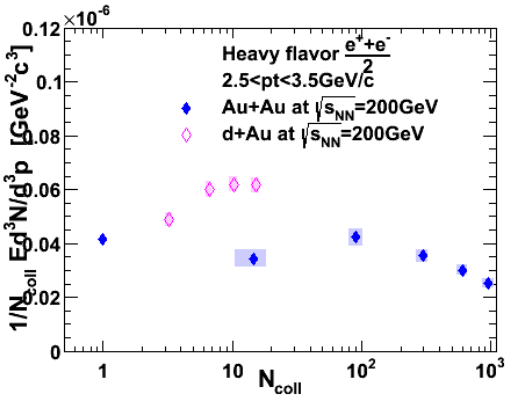

(b) p_T 2.5-3.5 GeV/C

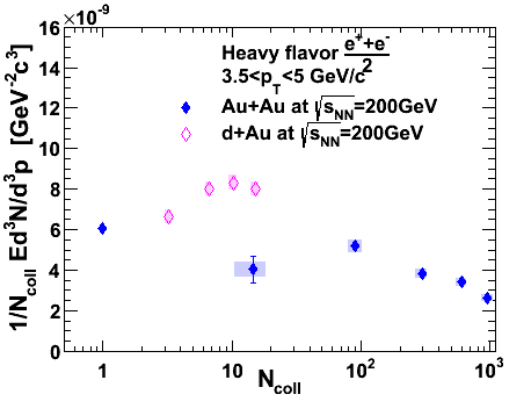

(c) p_T 3.5-5 GeV/C

Figure 6.11: (Color online) Integrated invariant yield per binary collision vs $N_{\rm coll}$ for heavy flavor electrons in the ${p_T}^e$ range $1.5 < p_T < 2.5$ GeV/c (upper two panels) and $3 < p_T < 5$ GeV/c (lower two panels) in Au + Au (in blue dots) and d + Au (in pink dots) collisions at $\sqrt{s_{NN}} = 200$ GeV.

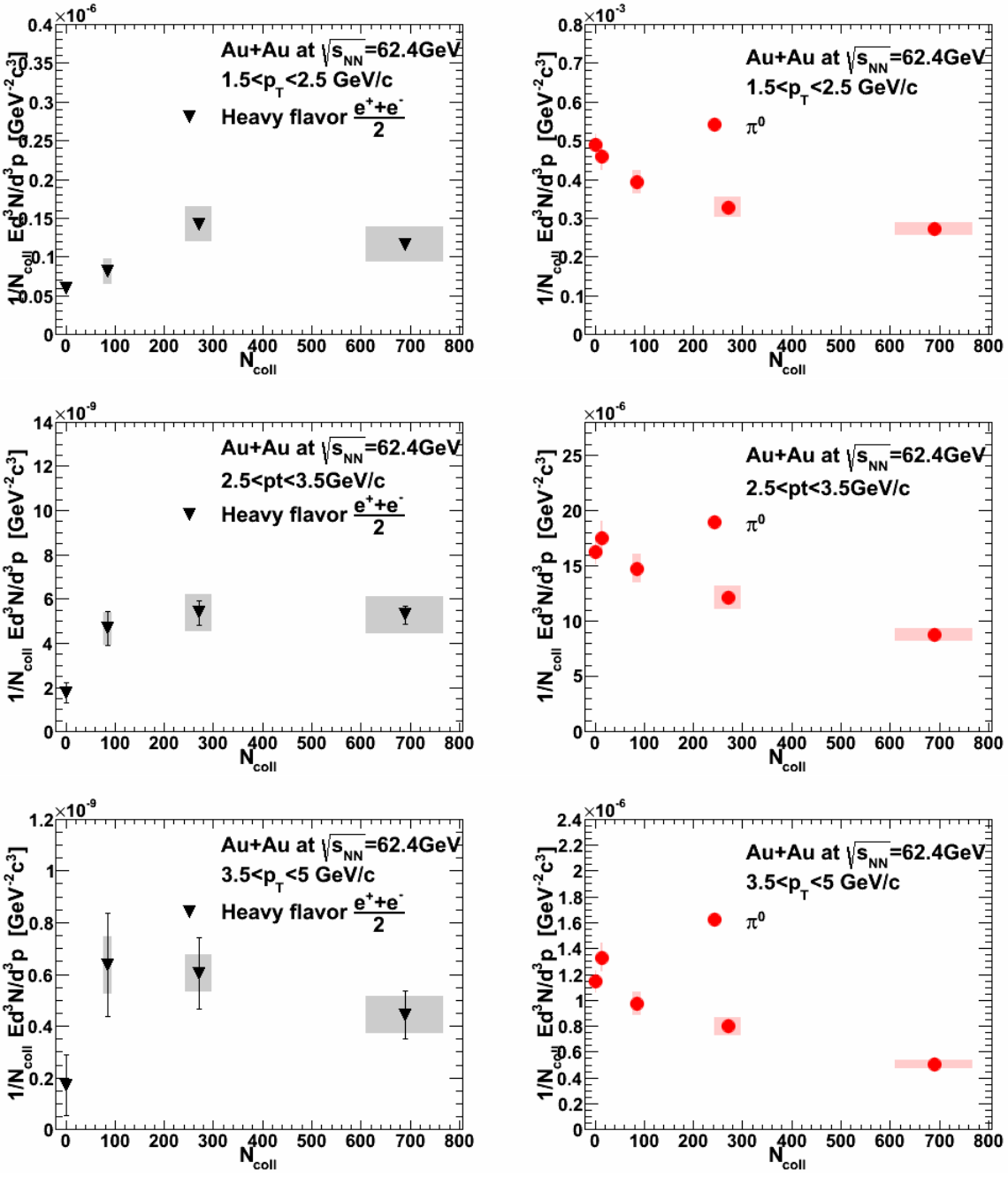

Figure 6.12: (Color online) Integrated invariant yield per binary collision vs $N_{\rm coll}$ for heavy flavor electrons (π^0) in the $p_T{}^e$ range $1.5 < p_T < 2.5$ GeV/c (upper two panels) and $3 < p_T < 5$ GeV/c (lower two panels) in Au + Au collisions at $\sqrt{s_{NN}} = 62.4$ GeV. π^0 shows a clear suppression for central events with large $N_{\rm coll}$ (right panels). Heavy flavor electrons (left panels) show different suppression patterns for low p_T and high p_T.

These trends are repeated at 62 GeV but the relative interplay between Cronin effect and energy loss could be different. In the Au + Au collisions at $\sqrt{s_{NN}}$ = 62.4 Gev, the energy density of the QGP is expected to be smaller than the density at $\sqrt{s_{NN}}$ = 200 GeV. Heavy quarks interacting with a less-dense medium may lose less energy at 62.4 GeV. Therefore, the suppression of the heavy quarks may be smaller compared to 200 GeV. On the other hand, the Cronin effect is believed to come from the initial state and caused by the boost of the parton transverse momentum in the multiple scattering before the hard-scattering. The Cronin enhancement is relatively more important when the high-Q^2 transfers are rarer, therefore, it increases as the collision energy decreases (Fig. 1.7). Hence, at $\sqrt{s_{NN}}$ = 62.4 GeV, the Cronin effect in the heavy flavor electron yield is expected to be larger than the Cronin effect at $\sqrt{s_{NN}}$ = 200 GeV. The enhancement we observed in the heavy flavor electron yield at 62.4 GeV is likely the result of the competition between the Cronin effect and energy loss. In the most central collisions, energy loss apparently begins to be the largest effect leading to a relatively flatter suppression pattern in the yield at high p_T at 62.4 GeV. For convenience, the integrated yield per binary collision in the Au + Au collisions at $\sqrt{s_{NN}}$ = 62.4 Gev is plotted again in Fig. 6.12 as a comparison to Fig. 6.11.

Other than the Cronin effect, the radial expansion of the medium can boost the low p_T particles to a higher p_T value and modify the p_T spectrum. Because this effect increases with the particle mass and the flow velocity [21] [22], the p_T of heavy flavor mesons with large mess is shifted more than light mesons. In additional, in Au + Au collisions at $\sqrt{s_{NN}}$ = 62.4 GeV, the heavy flavor electron spectrum is much steeper compare to 200 GeV. The particles boosted from the low p_T by the radial expansion may cause an enhancement at a fixed p_T in the 62.4 GeV system. This possibility is unlikely to explain the enhancement observed in d+Au and peripheral collisions. However it could provide a simple description of the p_T spectra in central collisions where it seems that heavy particles are losing energy in the medium. In effect, we are making the hypothesis that in central collisions the heavy flavor quarks lose sufficient energy to be in local equilibrium with the expanding medium.

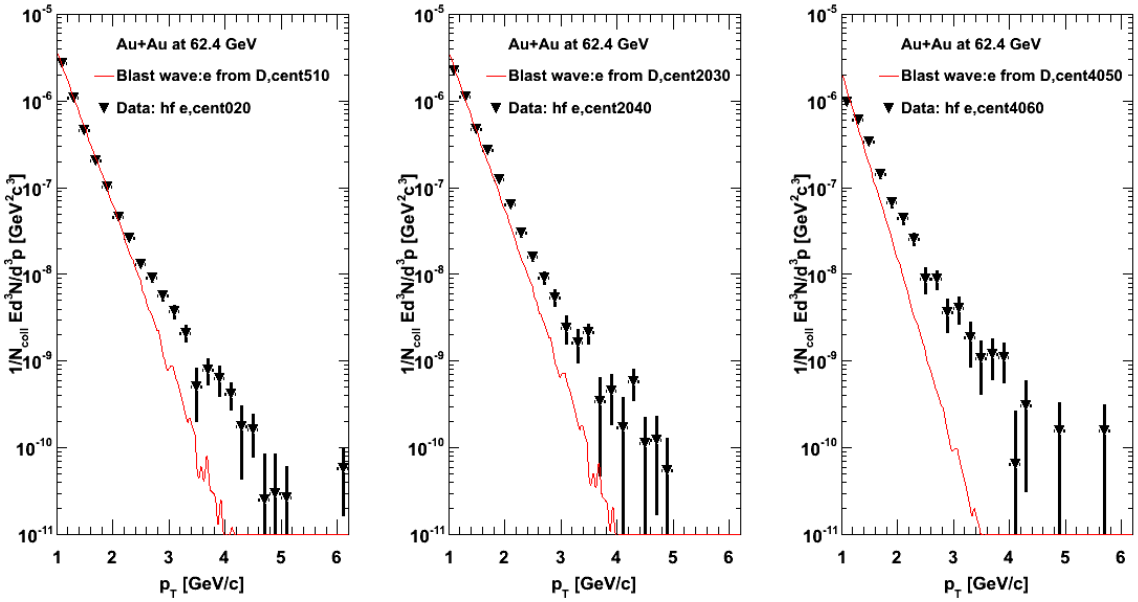

(a) Centrality: 0-20% (b) Centrality: 20-40% (c) Centrality: 40-60%

Figure 6.13: (Color online) the comparison between the shapes of p_T spectra from the data (black triangles) and from the electrons produced from the D mesons with a blast wave shape spectrum (red lines) for three centrality bins. The blast wave simulation is normalized to the data in the p_T range 1-2 GeV.

To test our hypothesis, assuming that the heavy quarks achieve local equilibrium in the collision in a hydrodynamic model, we decay D mesons with a blast wave shape [25] invariant yield to electrons in the simulation. The parameters of the blast wave function are the freeze-out temperature T_0 and the maximum velocity of the radial flow β_{max} (at the surface of the blast wave) determined from light quarks from Ref. [24]. Fig. 6.13 shows the comparison between the shapes of p_T spectra and from the electrons produced from the D mesons with a blast wave shape spectrum for three centrality bins. The blast wave simulation is normalized to the data in the p_T range 1-2 GeV. In the most central bin, at $p_T < 2$ GeV/c, the slope of the yield from the simulation matches well with the data. This may indicate that the low p_T ($p_T < 2$ GeV/c) D mesons are thermalized or close to thermalization in the medium created in the Au + Au collisions at 62.4GeV. Hence, in the central Au + Au collisions at $\sqrt{s_{NN}} = 62.4$ GeV, the radial boost of the low p_T D mesons, because of the bulk medium, may be large enough to cause the

observable enhancement in the yield of heavy flavor electrons. For other centrality bins, the shapes of the electron spectra from the simulation do not match with the data, which may indicate, either the D mesons are not fully thermalized and other effects (for example, Cronin effect) are still driving the observed p_T spectra. However, this is a very simple study which only compare the p_T shape of the electrons from the data and from the simple simulation. More work needs to be done to draw a strong conclusion. To further test if the D mesons are thermalized in the medium, electron hadron correlation study at this low energy may provide more information. Correlations are typically present since the heavy particles are produced in hard-scattering and are accompanied by hadrons in jets. For instance, if the equilibrium is achieved, no small angle correlation should be observed.

The v_2 of heavy flavor electrons at 62.4 GeV are also compared with π^0 results at 62.4 GeV [49] and heavy flavor electron results at 200 GeV [10]. In 0 < centrality < 20%, 6.14(a) shows that the v_2 of heavy flavor electrons at 62.4 GeV, the v_2 of π^0 at 62.4 GeV are consistent at p_T 1-1.5 GeV/c, which is consistent with Fig. 6.8. This is another possible evidence that the low p_T heavy quarks achieves local equilibrium or is close to local equilibrium in the medium in the central Au + Au collisions at $\sqrt{s_{NN}}$ = 62.4 GeV.

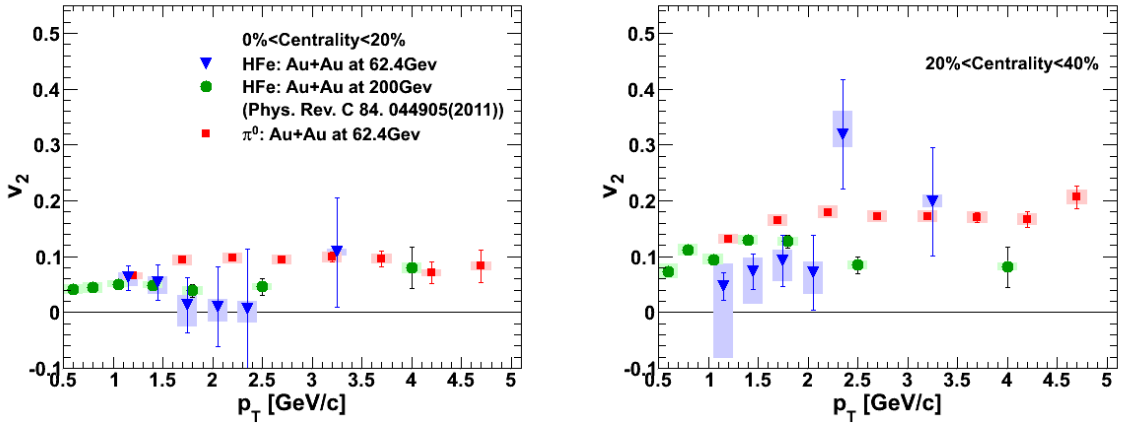

(a) Centrality: 0-20%

(b) Centrality: 20-40%

Figure 6.14: (Color online) Heavy flavor electron v_2 in Au + Au collisions at $\sqrt{s_{NN}}$ = 62.4 GeV (blue triangle) compare with heavy flavor electron v_2 in Au + Au collisions at $\sqrt{s_{NN}}$ = 200 GeV (green dots) and π^0 v_2 in in Au + Au collisions at $\sqrt{s_{NN}}$ = 62.4 GeV in two centrality bins: 0-20% and 20-40%.

CHAPTER 7. HEAVY FLAVOR ANALYSIS USING THE SILICON VERTEX TRACKER IN PHENIX

The Silicon Vertex Tracker (VTX), an important upgrade of the PHENIX experiment, is installed in Run-11. Before VTX was installed, the PHENIX experiment made many interesting discoveries of the suppression and flow of heavy quarks through the indirect measurement of electrons from heavy flavor meson decays. In these measurements, electrons from D meson decays and electrons from B meson decays are mixed together. However, because bottom quarks have much larger mass than charm quarks, it is possible that bottom and charm interact with the QGP differently. It is necessary to measure charm and bottom separately in the experiment to understand the properties of the QGP. The separation of charm and bottom requires an accurate measurement of the secondary decay vertex or the distance of closest approach (DCA), which is a big challenge in PHENIX before the installation of the VTX detector.

The main goal of the VTX detector is to separate electrons from D mesons decays and electrons from B meson decays by reconstructing the secondary decay vertex and measuring the DCA with fine resolution ($< 100\mu m$). This is an ongoing challenged measurement, even with the help of VTX. In this chapter, we will introduce the design of the VTX detector and some early work of using VTX to veto conversion electrons and measure heavy flavor electrons.

7.1 Detector Design

The VTX detector contains four layers. The inner two layers, located at radial distance of 2.5 cm and 5 cm, are silicon pixel detectors. The outer two layers, sit at radial distance of 11.7 cm and 16.6 cm, are silicon stripixel detectors. Fig. 7.1 shows a picture of the VTX installed

in the PHENIX IR and a schematic view of the pixel and stripixel layers in the VTX.

The pixel detectors use the technology developed by ALICE experiment. Each silicon sensor module is consist of 32 $\times$ 256 $\times$ 4 pixels and bump bonded to four readout chips. The active area of each pixel is 50 $\times$ 425 μm^2. Two sensors, which are bonded on to a kapton aluminum readout bus with a carbon fiber support stave, form a half ladder. One full ladder is made of two half ladders. The first pixel layer contains 10 ladders and the second layer contains 20. Fig. 7.2 shows the schematic view of the sensor module, readout bus and ladder in the pixel layer.

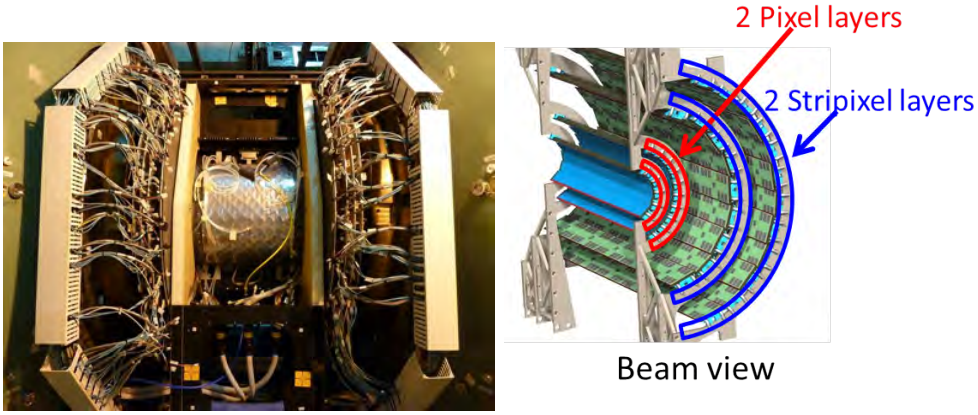

Figure 7.1: Picture of the VTX detector installed in PHENIX (left) and schematic view the 4 layers of the VTX detector (right)

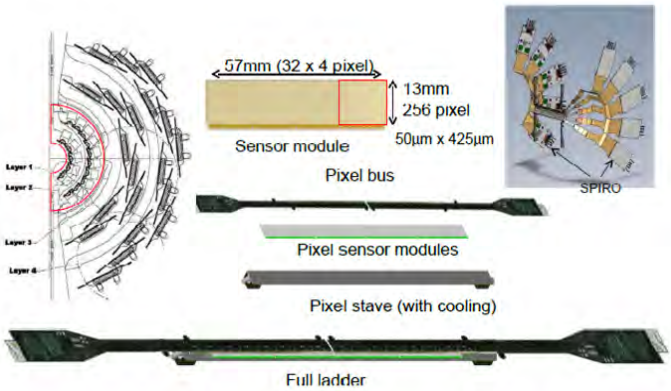

Figure 7.2: Schematic view the sensor module, readout bus and ladder in the pixel layer [66]

The sensor used in the stripixel detector is developed by the BNL Instrumentation Division. Each $80\mu m \times 1000\mu m$ pixel element has two serpertine-shaped metal strips [67] which collect charge from the ionization of the charged particle when transversing the silicon (Fig. 7.3). The X-strips connect the serpentines in a straight line, while the U-strips connect the serpentines at a 4.6 degree angle. The X and U strips provide two-dimensional readout from one side of the sensor. Each sensor with 1536 channels, is bonded with 12 svx4 readout chips and 1 sensor readout card (ROC) to form a module. 5 (or 6) modules are attached with the readout bus cable on a carbon composite stave to form a stripixel ladder in the 3rd (or 4th) VTX layer. The first stripixel layer contains 16 ladders and the second layer contains 24.

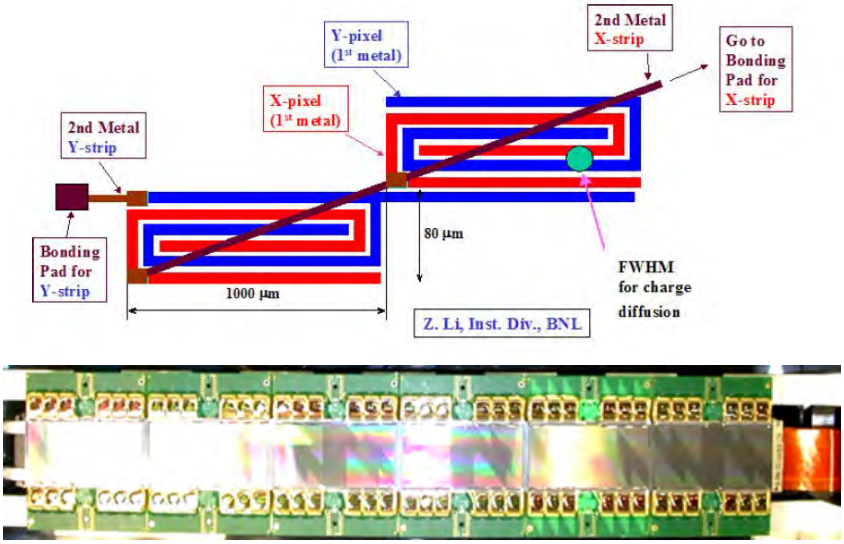

Figure 7.3: Schematic view the serpentine shaped structure in the stripixel detector and a picture of a stripixel ladder (contains 6 modules) in the lab [67]

The VTX detector is installed in PHENIX since Run-11. It successfully collected large amount of data in the Au + Au and p + p 200GeV collisions in Run-11 and Run-12. With the large coverage: $|\eta|$ <1.2, $\sim 2\pi$ in azimuth [67, 68], and fine spacial resolution ($\sim 77\mu m$), VTX provides the capability to measure the distance of closest approach to separate charm and bottom components of heavy flavor spectra.

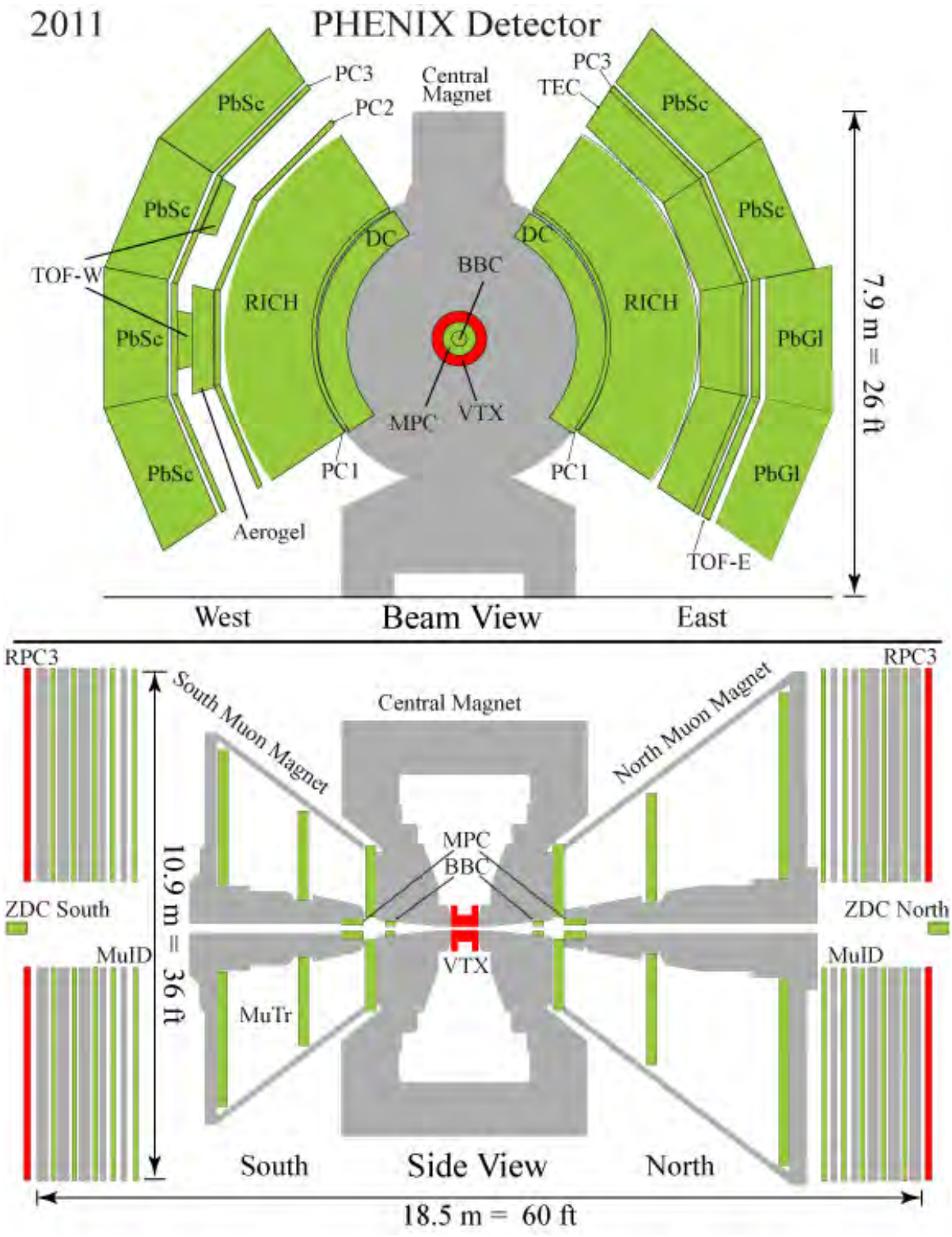

Figure 7.4: The PHENIX detector system in Run-11 from the beam view and the side view. The VTX detector is installed around the beam pipe.

7.2 Heavy Flavor Electron Measurement Using VTX Detector

Using VTX detector to measure D mesons and B mesons separately is an ongoing high priority task in PHENIX. Accurately measuring heavy flavor electrons is the first step of the bottom charm separation. In this section, we will introduce the distance of closest approach (DCA) and one important technique to identify and reject conversion electrons using VTX detector. This analysis uses the Au + Au $\sqrt{s_{NN}}$ = 200 GeV data set taken in Run-11.

In this section, the 4 VTX layers from the inner most layer to the outer most layer are referred to as B0, B1, B2, and B3.

7.2.1 The Distance of Closest Approach (DCA) Measurement

The VTX provides the ability to separate D and B mesons by the DCA measurement. DCA is the shortest distance from a reconstructed track to the primary collision vertex (Fig 7.5). B mesons have longer life time compare to D mesons, therefore the DCA distribution of electrons from B meson decays has wider width compare to the distribution of electrons from D meson decays. The bottom to charm ratio can be obtained by fitting the electron DCA.

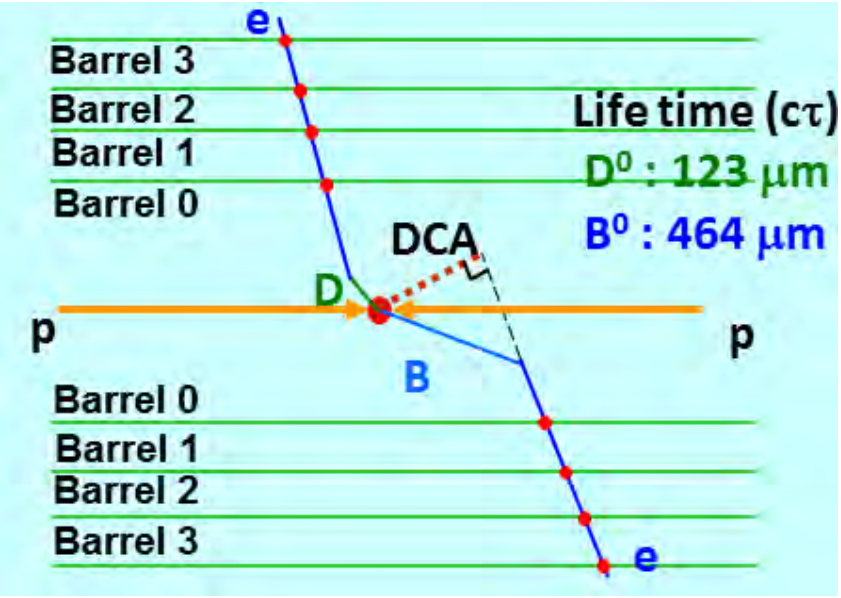

Figure 7.5: A schematic draw of how DCA is measured.

7.2.2 Conversion Veto Method and Conversion Veto Efficiency

In Chapter 3, we introduced the cocktail method to estimate the remaining photonic electron background in the inclusive electron spectrum. With VTX detector installed in PHENIX, a lot of electrons from the photon conversions are generated in the VTX material, which is more than 10 times of that of Dalitz decays. These amount of background is difficult to be subtracted completely by the cocktail method. Instead, we need to use VTX detector itself to eliminate the photonic background.

Most of the conversions happen in the outer layers, and do not leave a hit on the inner layer. By requiring a hit on B0 layer, most of the conversions can be eliminated. However, considering the high particle density in Au + Au collisions, some of these conversion generated on the outer layers can associate with a random hit on inner layers randomly and be reconstructed as a track in the software. These outer layer conversion with a randomly associated B0 hit can not be removed by our cuts. These tracks tend to be reconstructed with a large DCA and wash out the B meson signal at large DCA.

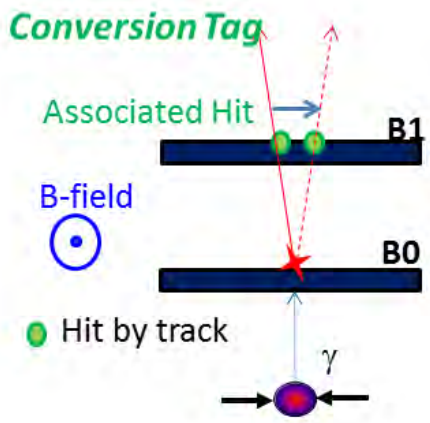

Figure 7.6: Conversion happened at B0 layer leaves two close-by hits in B1.

To reject the conversion background, the conversion veto method is used. Since electron pairs from photon conversions have small opening angle, there is a big chance that the pair leaves two close-by hits in a VTX layer (Fig. 7.6). Thus, we can veto the conversion electrons by requiring that there is no other hits in a narrow window around the location of the target

hit.

Figure 7.7 shows hit distributions near a hit of electron tracks or hadron tracks in four VTX layers . The sharp peak at $\delta\phi$ is the target hit itself. Hadrons are not supposed to have an associated hit, therefore, the almost flat distribution of hadrons is an estimation of the random association. Because of conversion, there are more hits around the electron tracks compare with hadron tracks. The electron distribution is asymmetric in the positive and negative direction because the partner electrons have the opposite charge of the target electron and are bended by the magnetic field to a certain direction.

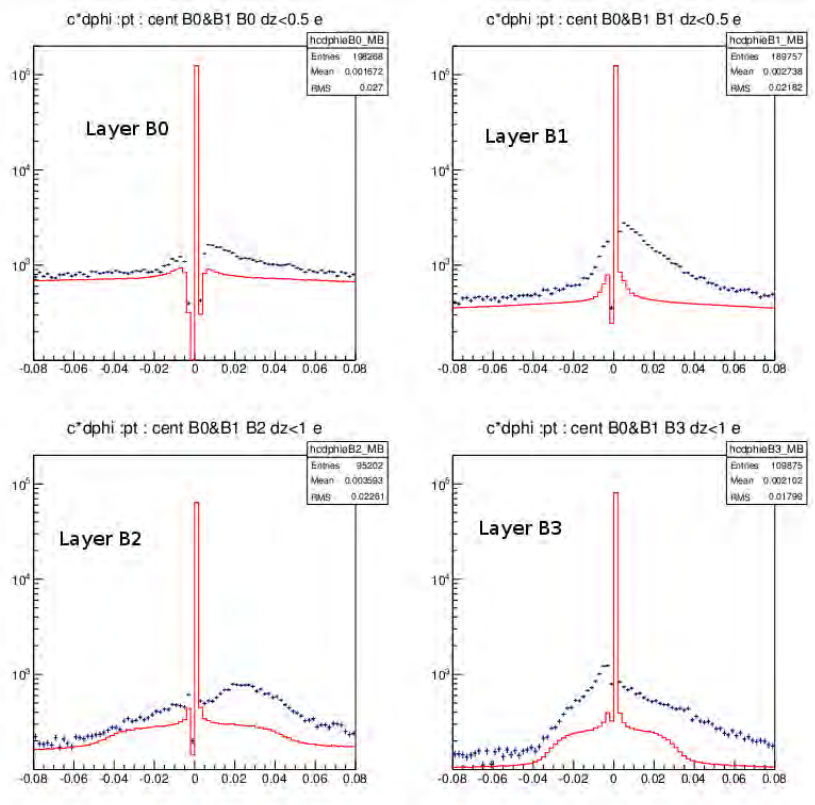

Figure 7.7: Data: hit distributions around a hit of electron tracks and hadron tracks in each of VTX layers [69]

Table 7.1 shows the conversion veto window, which mean if another hit stays inside the window around the hit associated with a electron track, the electron tracks will be rejected as conversion background.

Table 7.1: VETO window

VTX Layer	**Cuts**
B0	$\|dz\| < 0.5mm \&\& -0.02 < \delta\phi < 0.04$
B1	$\|dz\| < 0.5mm \&\& -0.02 < \delta\phi < 0.06$
B2	$\|dz\| < 1.0mm \&\& -0.04 < \delta\phi < 0.08$
B3	$\|dz\| < 1.0mm \&\& -0.02 < \delta\phi < 0.08$

In order to obtain the conversion tagging efficiency, single π^0 events are simulated and run through the whole PISA and reconstruction chain. Fig. 7.8 shows the decay vertex radius. We can clearly see the conversion from the beam pipe and the 4 VTX layers.

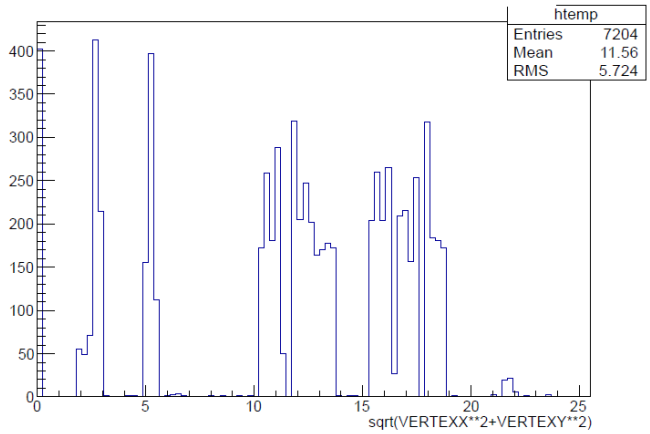

Figure 7.8: vertex radius of the electrons in the single π^0 simulation

To tag conversion electrons, for each VTX hit associated with a CNT track, the distance between the target hit and the close-by VTX hits in ϕ direction is plotted. Fig. 7.9, 7.10, 7.11, 7.12 show the dϕ distribution in the certain p_T range. The veto area in Table 7.1 can cover most of the conversion area. Also, these plots show a good matching between the simulation and the p + p data.

Fig. 7.13 shows the veto efficiency of Dalitz decay and B0 conversions, also the over all veto efficiency. At 1.5 GeV/c, more than 40% of the Dalitz decay and around 75 % of the B0 conversions can be removed by the veto method.

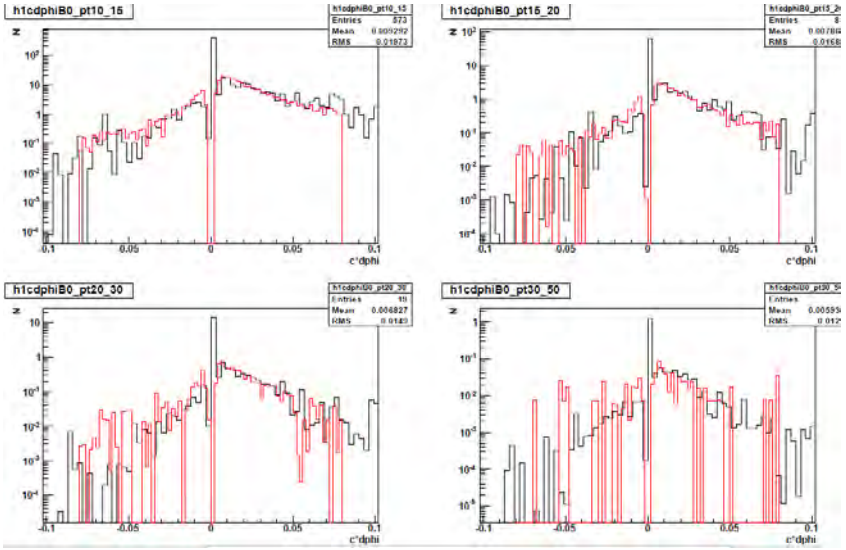

Figure 7.9: cdϕ distribution of the close by VTX hits in layer B0. Black is simulation and red is p + p data. abs(dz)< 0.05 cm cut is applied. 4 p_T bins are 1−1.5 GeV/c, 1.5−2 GeV, 2−3 GeV, 3−5 GeV

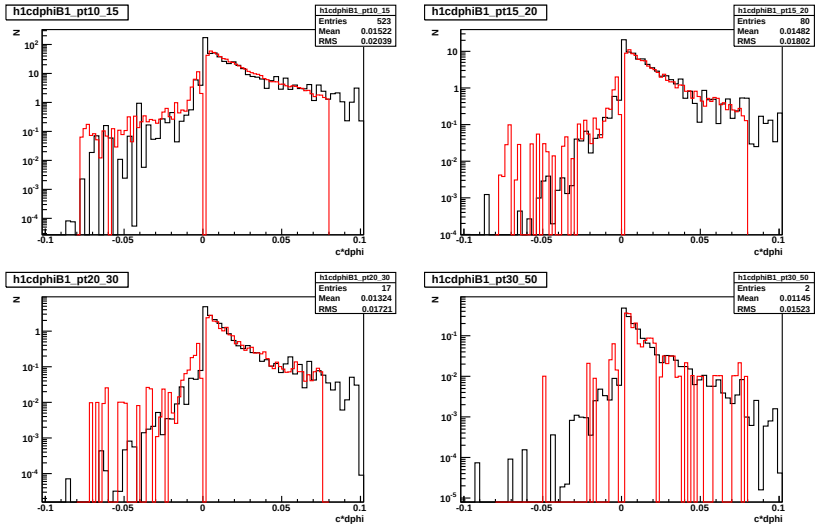

Figure 7.10: cdϕ distribution of the close by VTX hits in layer B0. Black is simulation and red is p + p data. abs(dz)< 0.05 cm cut is applied. 4 p_T bins are 1−1.5 GeV/c, 1.5−2 GeV, 2−3 GeV, 3−5 GeV

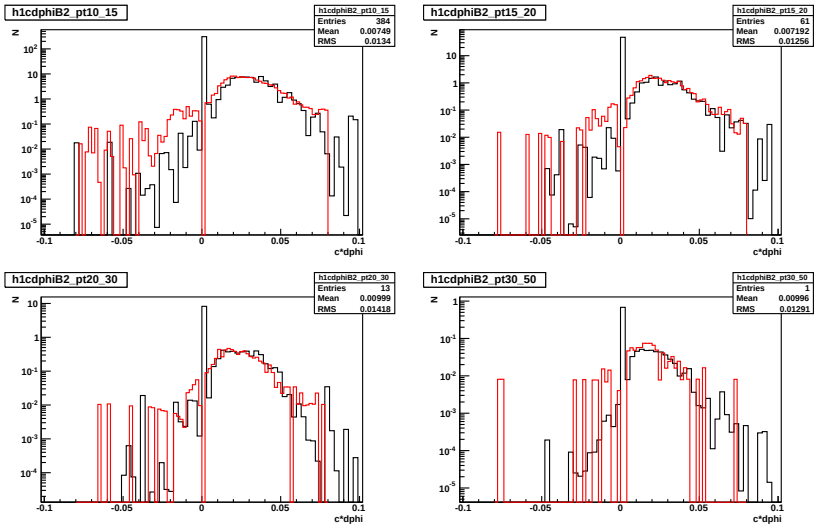

Figure 7.11: cdϕ distribution of the close by VTX hits in layer B2. Black is simulation and red is p + p data. abs(dz) $<$ 0.1cm cut is applied. 4 p_T bins are 1$-$1.5GeV, 1.5$-$2 GeV,2$-$3 GeV, 3$-$5 GeV

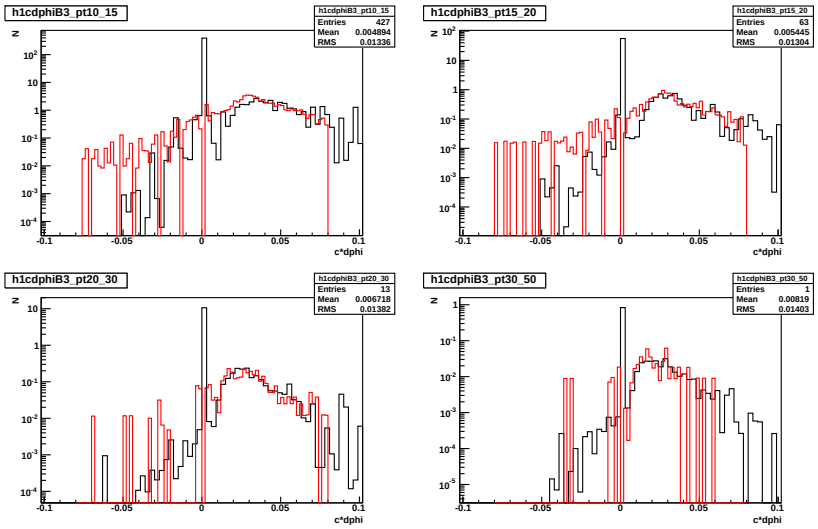

Figure 7.12: c*dϕ distribution of the close by VTX hits in layer B3. Black is simulation and red is p + p data. abs(dz)¡0.1cm cut is applied. 4 p_T bins are 1-1.5GeV, 1.5-2GeV,2-3GeV, 3-5GeV

Layer by layer veto efficiency is also studied for Dalitz decays and conversions at B0(Fig. 7.14) This analysis shows that the veto method can effectively remove the photonic electrons and increase the heavy flavor to photonic ratio R_{np}.

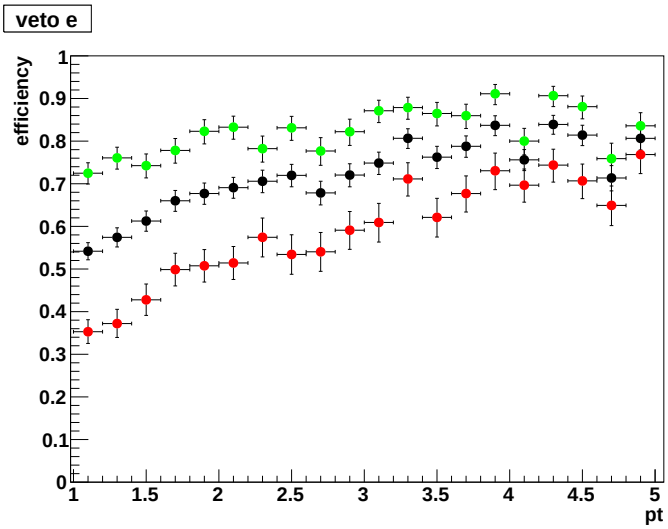

Figure 7.13: veto efficiency vs p_T (Red: Dalitz, green: conversions at B0, black: overall)

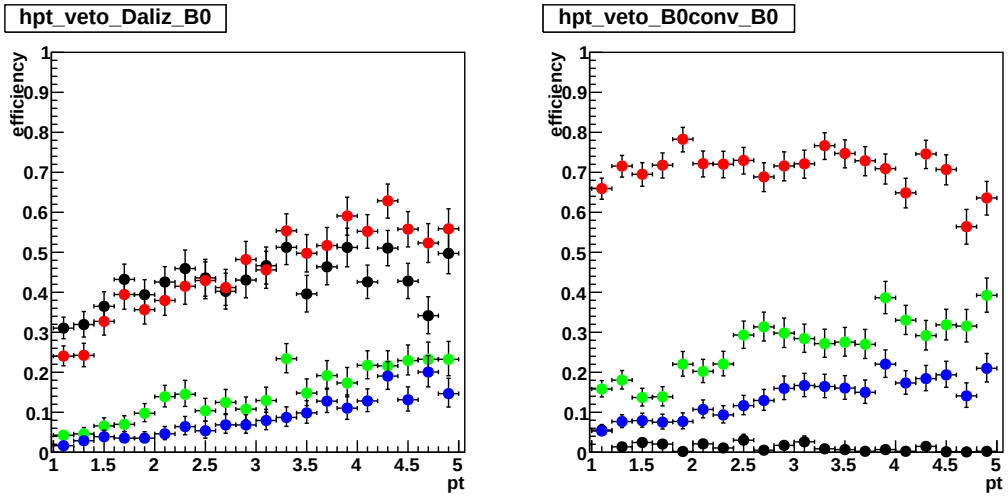

Figure 7.14: Layer by layer veto efficiency vs p_T for Dalitz decay (left plot) and conversions at B0 (right plot). Black:B0, red:B1, green:B2, blue:B3

7.2.3 Heavy Flavor Electron Fraction

The heavy flavor electron fraction R_{HF} or the nonphotonic to photonic ratio R_{np} is critical to extract heavy flavor electrons from the inclusive electrons. R_{HF} and R_{np} can be obtained by the conversion veto method.

We assume that the total number of inclusive electron tracks before applying any veto cuts is N_e^{total}, the number of tracks after applying veto cuts is N_e^{NotV}, the tracks removed by veto cuts is N_e^V. N_e^{total} has the photonic part (N_P) and the heavy flavor part (N_{HF}), and the photonic part is mainly from Dalitz decays and photon conversions. When we apply veto cuts, the photonic electrons N_P will be tagged by the veto efficiency (ϵ_V). However, because of the high multiplicity, the N_{HF} and left part of the N_P can randomly associate with a nearby hit and be removed by veto cuts with efficiency ϵ_R. Then, we have the following equation:

$$N_e^{total} = N_{HF} + N_P \tag{7.1}$$

$$N_e^V = N_{HF} \times \epsilon_R + N_P \times \epsilon_V + N_P \times (1 - \epsilon_V) \times \epsilon_R \tag{7.2}$$

$$N_e^{NotV} = N_{HF} \times (1 - \epsilon_R) + N_P \times (1 - \epsilon_V) \times (1 - \epsilon_R) \tag{7.3}$$

ϵ_V is obtained by the single π^0 simulation (Fig. 7.13). The ratio between the veto rejected hadron spectrum and the total hadron spectrum before any veto cuts is a good estimation of the random veto efficiency ϵ_R . We can solve the equations and calculated N_{HF} and N_P, which are the heavy flavor and photonic e spectra before applying the veto cuts. Fig. 7.15 shows the heavy flavor and photonic invariant yield in MB data compare to Run-4 results. The ratio of the Run-11 yield to the Run-4 yield is flat.

In data analysis, veto cuts for all 4 layers are applied. $N_{HF}^{AfterVeto}$ and $N_P^{AfterVeto}$ are different from N_{HF} and N_P:

$$N_{HF}^{AfterVeto} = N_{HF} \times (1 - \epsilon_R) \tag{7.4}$$

$$N_P^{AfterVeto} = N_P \times (1 - \epsilon_V) \times (1 - \epsilon_R) \tag{7.5}$$

$$\tag{7.6}$$

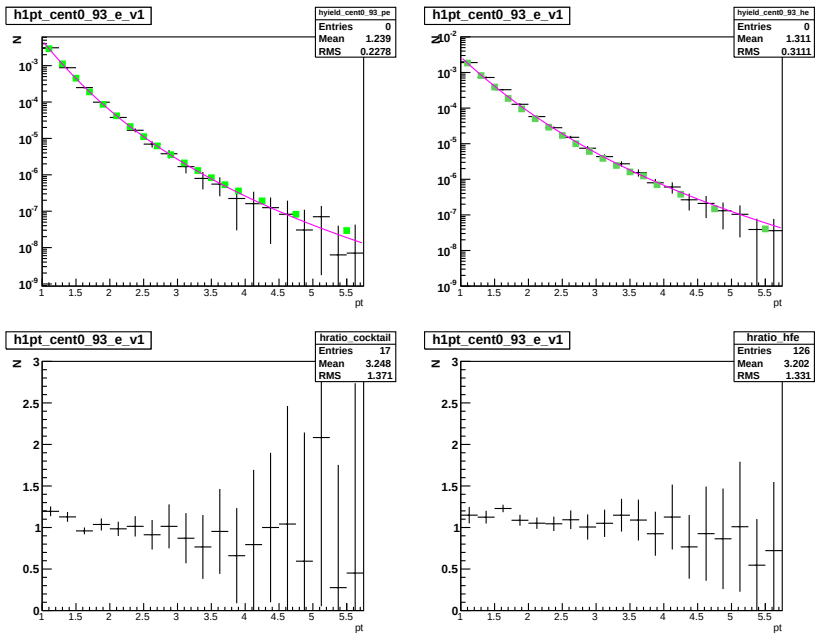

Figure 7.15: Left top: Photonic e invariant yield in Run11(black) and Run4(green), Run4 yield is fitted with magenta curve. Left bottom: Run11 to Run4 conversion e ratio. Right top: heavy flavor e invariant yield in Run11(black) and Run4(green), Run4 yield is fitted with magenta curve. Right bottom: Run11 to Run4 heavy flavor e ratio. (All in MB data, same scale factor applied to both Run11 photonic and heavy flavor spectra)

Then, the heavy flavor fraction R_{HF} in the Run-11 analysis with veto cuts is defined as:

$$R_{HF} = \frac{N_{HF}^{AfterVeto}}{N_{HF}^{AfterVeto} + N_{P}^{AfterVeto}} \tag{7.7}$$

Fig. 7.16 shows the comparison between the R_{HF} estimated from Run-4 R_{NP} accounting in the increased detector material in Run-11 and the new R_{HF} calculated by the conversion veto efficiency. Although the new R_{HF} is a little bit larger than Run-4 estimation around $p_T = 2\ GeV/c$, the shapes are very close. This cross check provides an estimation of the systematic uncertainties in the heavy flavor component when doing the DCA decomposition and charm bottom separation.

Once the R_{HF} is calculated, we can easily multiply the inclusive electron yield with R_{HF} to obtain the yield of heavy flavor electrons.

In summary, using the VTX detector, the photonic electron background can be directly subtracted from the inclusive electron yield to obtain heavy flavor electrons by the conversion

veto method. The next step of the analysis is to decomposite the DCA distribution of heavy flavor electrons and separate charm and bottom.

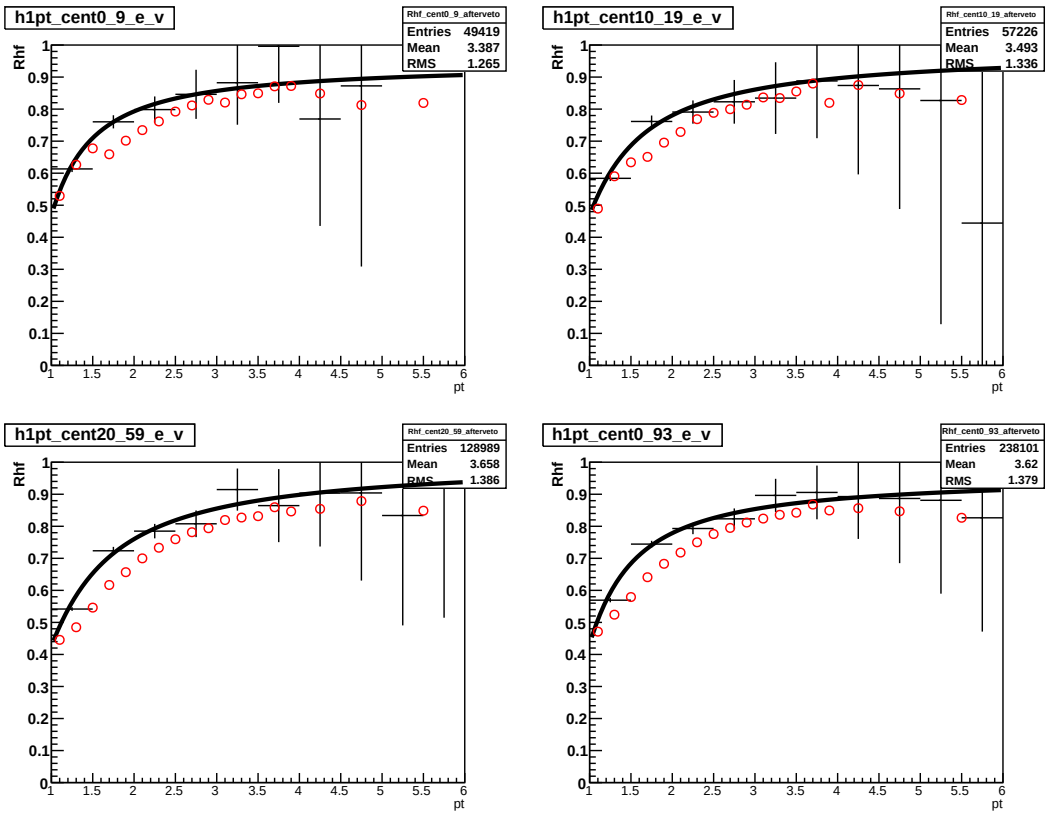

Figure 7.16: R_{HQ} calculated from Run-11 data and conversion veto efficiency (in black) and R_{HQ} based on Run-4 result (in red open circle) in 4 centrality bins (0-10,10-20,20-60 and MB)

CHAPTER 8. SUMMARY

The invariant yield and elliptic flow of electrons from heavy flavor meson semi-leptonic decays were measured in Au + Au collisions at $\sqrt{s_{NN}}$ = 62 Gev in PHENIX. The integrated invariant yield per binary collision indicates a different suppression pattern compared to the previous PHENIX measurement of heavy flavor electrons in Au + Au and d + Au collisions at $\sqrt{s_{NN}}$ = 200 GeV. The initial state Cronin enhancement competes with the energy loss in the medium and becomes the dominant effect at low to moderate p_T for heavy quarks at this lower beam energy. The non-zero v_2 of heavy flavor electrons indicates that heavy quarks flow at $\sqrt{s_{NN}}$ = 62.4 GeV. Further understanding of the properties of the medium and energy loss of the heavy quarks at 62.4 GeV requires the measurement of heavy flavor electrons in d + Au, Cu + Au collisions at $\sqrt{s_{NN}}$ = 62.4 GeV, and the study of electron-hadron correlation.

The separation of charm and bottom is also critical to understand the different energy loss mechanism of charm and bottom quarks in the QGP. With the newly upgraded VTX detector, the PHENIX experiment is capable of measuring D and B quarks separately by an accurate measurement of the distance of closest approach (DCA). Currently, the VTX detector successfully measured the heavy flavor fraction in the inclusive electron spectrum using the conversion veto method. The next step is to measure the DCA distribution of heavy flavor electrons and decompose it to DCA of electrons from D decays and DCA of electrons from B decays.

APPENDIX . DATA TABLES

Tables of Inclusive Electron Invariant Yield

Table A.1: Inclusive electron invariant yield (centrality: 0-20% and 20-40%) in Au + Au collisions at $\sqrt{s_{NN}} = 62.4$ GeV

Centrality 0-20%				Centrality 20-40%			
p_T	*inv.yield*	**stat. error**	**syst. error**	p_T	*inv.yield*	**stat. error**	**syst. error**
1.05	0.00673218	8.08709e-05	0.000942505	1.05	0.00286411	3.67004e-05	0.000400975
1.15	0.00422175	5.48592e-05	0.000591044	1.15	0.00179554	2.53219e-05	0.000251376
1.25	0.00250687	3.6075e-05	0.000350962	1.25	0.00110232	1.73393e-05	0.000154324
1.35	0.00150026	2.43902e-05	0.000210036	1.35	0.000673788	1.19451e-05	9.43303e-05
1.45	0.000963047	1.78623e-05	0.000134827	1.45	0.0004166	8.70676e-06	5.8324e-05
1.55	0.000627356	1.3337e-05	8.78298e-05	1.55	0.000283813	6.76552e-06	3.97338e-05
1.65	0.00039947	9.98612e-06	5.59259e-05	1.65	0.00020061	5.30079e-06	2.80855e-05
1.75	0.000261977	7.62493e-06	3.66767e-05	1.75	0.000119135	3.91047e-06	1.66789e-05
1.85	0.000179184	6.06846e-06	2.50858e-05	1.85	8.2815e-05	3.12186e-06	1.15941e-05
1.95	0.000119	4.78495e-06	1.666e-05	1.95	5.6408e-05	2.4781e-06	7.89712e-06
2.05	8.17413e-05	3.82991e-06	1.14438e-05	2.05	3.9618e-05	2.0621e-06	5.54652e-06
2.15	4.99638e-05	2.99289e-06	6.99493e-06	2.15	2.66703e-05	1.64754e-06	3.73384e-06
2.25	3.84157e-05	2.57517e-06	5.37819e-06	2.25	1.83428e-05	1.32038e-06	2.56799e-06
2.35	2.86372e-05	2.03482e-06	4.00921e-06	2.35	1.2534e-05	1.07728e-06	1.75475e-06
2.45	1.93706e-05	1.66024e-06	2.71189e-06	2.45	9.40013e-06	8.85383e-07	1.31602e-06
2.55	1.31176e-05	1.34599e-06	1.83647e-06	2.55	6.41897e-06	7.26064e-07	8.98656e-07
2.65	1.21272e-05	1.20894e-06	1.69781e-06	2.65	4.72438e-06	6.02369e-07	6.61413e-07
2.75	7.27627e-06	9.90271e-07	1.01868e-06	2.75	3.61813e-06	5.35149e-07	5.06538e-07
2.85	7.04805e-06	9.67135e-07	9.86727e-07	2.85	3.06942e-06	4.7605e-07	4.29719e-07
2.95	4.1346e-06	7.08209e-07	5.78845e-07	2.95	1.62071e-06	3.7164e-07	2.269e-07
3.05	4.30604e-06	6.87123e-07	6.02846e-07	3.05	1.4753e-06	3.46107e-07	2.06541e-07
3.15	2.50833e-06	5.48318e-07	3.51166e-07	3.15	7.75256e-07	2.6316e-07	1.08536e-07
3.25	2.32521e-06	4.581e-07	3.2553e-07	3.25	9.03227e-07	2.72985e-07	1.26452e-07
3.35	1.45573e-06	4.35694e-07	2.03802e-07	3.35	4.76618e-07	2.0194e-07	6.67266e-08
3.45	1.0166e-06	3.38248e-07	1.42324e-07	3.45	6.35547e-07	1.9238e-07	8.89765e-08
3.55	2.20543e-07	2.48397e-07	3.08761e-08	3.55	7.27428e-07	2.14847e-07	1.0184e-07
3.65	9.67874e-07	2.87515e-07	1.35502e-07	3.65	1.07786e-07	9.12395e-08	1.50901e-08
3.75	3.95769e-07	2.09649e-07	5.54076e-08	3.75	2.40437e-07	1.18116e-07	3.36612e-08
3.85	7.01301e-07	2.66257e-07	9.81822e-08	3.85	1.91933e-07	1.07246e-07	2.68706e-08
3.95	3.15083e-07	1.79874e-07	4.41117e-08	3.95	1.32882e-07	7.70567e-08	1.86035e-08
4.05	3.36994e-07	1.51404e-07	4.71792e-08	4.05	1.03823e-08	5.3585e-08	1.45352e-09
4.15	3.2035e-07	1.31297e-07	4.48491e-08	4.15	1.35347e-07	8.95654e-08	1.89485e-08
4.25	-2.2824e-08	1.03649e-07	3.19536e-09	4.25	1.61704e-07	8.11642e-08	2.26386e-08
4.35	3.18621e-07	1.43076e-07	4.4607e-08	4.35	1.60998e-07	8.07966e-08	2.25397e-08
4.45	2.04515e-07	1.02603e-07	2.86321e-08	4.45	3.99561e-08	4.00923e-08	5.59385e-09
4.55	4.97766e-08	4.99311e-08	6.96872e-09	4.55	3.88996e-08	3.90266e-08	5.44595e-09
4.65	9.08026e-09	6.30341e-08	1.27124e-09	4.65	3.8097e-08	3.82162e-08	5.33359e-09
4.75	4.82704e-08	4.84081e-08	6.75785e-09	4.75	3.77231e-08	3.78362e-08	5.28123e-09
4.85	0	0	0	4.85	3.62802e-08	3.63846e-08	5.07923e-09
4.95	5.47584e-08	7.55125e-08	7.66618e-09	4.95	0	0	0
5.05	0	0	0	5.05	0	0	0
5.15	4.5165e-08	4.5275e-08	6.3231e-09	5.15	0	0	0

Table A.2: Inclusive electron invariant yield (centrality: 40-60% and Minimum Bias) in Au + Au collisions at $\sqrt{s_{NN}} = 62.4$ GeV

Centrality 40-60%				Minimum Bias			
p_T	*inv.yield*	**stat. error**	**syst. error**	p_T	*inv.yield*	**stat. error**	**syst. error**
1.05	0.000839801	1.39583e-05	0.000117572	1.05	0.00204133	2.21248e-05	0.000285786
1.15	0.000504572	9.83594e-06	7.06401e-05	1.15	0.00127379	1.45348e-05	0.000178331
1.25	0.000312632	7.02885e-06	4.37684e-05	1.25	0.000766936	9.30944e-06	0.000107371
1.35	0.000192344	5.06392e-06	2.69282e-05	1.35	0.000463287	6.07927e-06	6.48601e-05
1.45	0.000127527	3.88039e-06	1.78537e-05	1.45	0.000296297	4.30912e-06	4.14816e-05
1.55	7.99314e-05	2.94937e-06	1.11904e-05	1.55	0.00019419	3.15417e-06	2.71866e-05
1.65	5.11228e-05	2.23934e-06	7.15719e-06	1.65	0.000127972	2.33402e-06	1.79161e-05
1.75	3.38439e-05	1.75296e-06	4.73814e-06	1.75	8.14829e-05	1.73002e-06	1.14076e-05
1.85	2.26246e-05	1.40462e-06	3.16745e-06	1.85	5.59829e-05	1.35944e-06	7.83761e-06
1.95	1.49315e-05	1.10763e-06	2.09042e-06	1.95	3.75532e-05	1.06235e-06	5.25745e-06
2.05	1.09931e-05	9.20233e-07	1.53904e-06	2.05	2.591e-05	8.52629e-07	3.6274e-06
2.15	8.328e-06	7.63206e-07	1.16592e-06	2.15	1.71048e-05	6.73324e-07	2.39467e-06
2.25	5.80282e-06	6.4165e-07	8.12395e-07	2.25	1.2396e-05	5.61657e-07	1.73544e-06
2.35	4.05617e-06	5.05581e-07	5.67864e-07	2.35	8.94174e-06	4.47788e-07	1.25184e-06
2.45	2.39938e-06	4.02544e-07	3.35913e-07	2.45	6.11247e-06	3.63064e-07	8.55746e-07
2.55	1.79044e-06	3.40419e-07	2.50662e-07	2.55	4.26685e-06	2.97723e-07	5.97358e-07
2.65	1.53563e-06	2.92804e-07	2.14988e-07	2.65	3.56945e-06	2.58762e-07	4.99723e-07
2.75	1.33809e-06	2.69856e-07	1.87333e-07	2.75	2.45781e-06	2.19757e-07	3.44093e-07
2.85	1.02767e-06	2.37577e-07	1.43874e-07	2.85	2.1648e-06	2.05309e-07	3.03073e-07
2.95	3.06579e-07	1.25995e-07	4.29211e-08	2.95	1.15657e-06	1.49979e-07	1.6192e-07
3.05	6.78612e-07	1.9689e-07	9.50056e-08	3.05	1.25149e-06	1.50362e-07	1.75209e-07
3.15	4.10761e-07	1.55086e-07	5.75065e-08	3.15	7.18608e-07	1.17716e-07	1.00605e-07
3.25	2.91032e-07	1.28981e-07	4.07445e-08	3.25	6.93076e-07	1.05534e-07	9.70306e-08
3.35	2.36565e-07	1.16262e-07	3.31191e-08	3.35	4.27481e-07	9.22362e-08	5.98474e-08
3.45	1.76396e-07	8.86321e-08	2.46955e-08	3.45	3.59843e-07	7.49259e-08	5.0378e-08
3.55	1.25848e-07	7.29935e-08	1.76187e-08	3.55	2.30313e-07	6.59436e-08	3.22438e-08
3.65	1.22421e-07	7.09888e-08	1.71389e-08	3.65	2.21258e-07	5.6025e-08	3.09761e-08
3.75	1.55799e-07	7.82262e-08	2.18119e-08	3.75	1.61039e-07	4.84666e-08	2.25454e-08
3.85	1.5367e-07	7.71414e-08	2.15138e-08	3.85	2.0259e-07	5.47822e-08	2.83626e-08
3.95	7.52499e-08	5.34072e-08	1.0535e-08	3.95	1.03031e-07	3.75295e-08	1.44243e-08
4.05	0	0	0	4.05	5.98038e-08	2.84323e-08	8.37254e-09
4.15	3.54395e-08	3.55575e-08	4.96154e-09	4.15	9.32005e-08	3.12456e-08	1.30481e-08
4.25	0	0	0	4.25	4.09696e-08	2.6432e-08	5.73574e-09
4.35	6.83716e-08	4.84948e-08	9.57202e-09	4.35	1.07517e-07	3.26238e-08	1.50523e-08
4.45	0	0	0	4.45	4.37036e-08	1.96124e-08	6.1185e-09
4.55	0	0	0	4.55	1.70191e-08	1.20727e-08	2.38268e-09
4.65	0	0	0	4.65	1.00915e-08	1.3537e-08	1.41281e-09
4.75	0	0	0	4.75	1.65042e-08	1.17044e-08	2.31059e-09
4.85	0	0	0	4.85	7.93644e-09	7.95842e-09	1.1111e-09
4.95	3.06361e-08	3.07082e-08	4.28905e-09	4.95	1.7447e-08	1.50602e-08	2.44258e-09
5.05	0	0	0	5.05	0	0	0
5.15	0	0	0	5.15	7.72126e-09	7.74028e-09	1.08098e-09

Tables of Photonic Electron Invariant Yield

Table A.3: Photonic electron invariant yield (centrality: 0-20% and 20-40%) in Au + Au collisions at $\sqrt{s_{NN}} = 62.4$ GeV

Centrality 0-20%				Centrality 20-40%			
p_T	*inv.yield*	**stat. error**	**syst. error**	p_T	*inv.yield*	**stat. error**	**syst. error**
1.05	0.0065983	3.63048e-05	0.000583894	1.05	0.00325982	1.81654e-05	0.000251628
1.15	0.00389601	2.24611e-05	0.000342799	1.15	0.00190743	1.11352e-05	0.000147477
1.25	0.00229466	1.38523e-05	0.000200884	1.25	0.00111657	6.77824e-06	8.64442e-05
1.35	0.00137684	8.62232e-06	0.000119958	1.35	0.00068378	4.31293e-06	5.30153e-05
1.45	0.000879509	5.76391e-06	7.60957e-05	1.45	0.000424329	2.76226e-06	3.29311e-05
1.55	0.000543805	3.68293e-06	4.68205e-05	1.55	0.000269038	1.78799e-06	2.08881e-05
1.65	0.000348148	2.43305e-06	2.97823e-05	1.65	0.000168541	1.15638e-06	1.31092e-05
1.75	0.000221646	1.6063e-06	1.88626e-05	1.75	0.000110093	7.80794e-07	8.56589e-06
1.85	0.000147155	1.088e-06	1.24413e-05	1.85	7.25182e-05	5.25457e-07	5.64478e-06
1.95	9.56452e-05	7.28587e-07	8.03736e-06	1.95	4.69526e-05	3.44669e-07	3.65894e-06
2.05	6.42795e-05	5.01105e-07	5.37022e-06	2.05	3.20041e-05	2.42915e-07	2.49291e-06
2.15	4.22932e-05	3.39665e-07	3.51395e-06	2.15	2.2049e-05	1.70329e-07	1.71746e-06
2.25	2.94996e-05	2.39149e-07	2.43487e-06	2.25	1.47238e-05	1.161e-07	1.14849e-06
2.35	2.02551e-05	1.66997e-07	1.6612e-06	2.35	1.05535e-05	8.46372e-08	8.21237e-07
2.45	1.37703e-05	1.16302e-07	1.12269e-06	2.45	7.31052e-06	5.95294e-08	5.68724e-07
2.55	9.28354e-06	7.93287e-08	7.53117e-07	2.55	5.16576e-06	4.26135e-08	4.02211e-07
2.65	6.63536e-06	5.76406e-08	5.34814e-07	2.65	3.63553e-06	3.05277e-08	2.82749e-07
2.75	4.72041e-06	4.19074e-08	3.77917e-07	2.75	2.59722e-06	2.2102e-08	2.01836e-07
2.85	3.36477e-06	2.99711e-08	2.67404e-07	2.85	1.90005e-06	1.65928e-08	1.47527e-07
2.95	2.43634e-06	2.21076e-08	1.92399e-07	2.95	1.3661e-06	1.1851e-08	1.06028e-07
3.05	1.74618e-06	1.60479e-08	1.37042e-07	3.05	1.00747e-06	8.92925e-09	7.80981e-08
3.15	1.32436e-06	1.22467e-08	1.03046e-07	3.15	7.22872e-07	6.52486e-09	5.60861e-08
3.25	9.32745e-07	8.53588e-09	7.21947e-08	3.25	5.70615e-07	5.19838e-09	4.40096e-08
3.35	6.87332e-07	6.46457e-09	5.28713e-08	3.35	3.96077e-07	3.60948e-09	3.06604e-08
3.45	5.25084e-07	4.92154e-09	4.00549e-08	3.45	2.97203e-07	2.76276e-09	2.29573e-08
3.55	3.91883e-07	3.70833e-09	2.97074e-08	3.55	2.29822e-07	2.15373e-09	1.76948e-08
3.65	3.00679e-07	2.88706e-09	2.26161e-08	3.65	1.74289e-07	1.65524e-09	1.3398e-08
3.75	2.20203e-07	2.12189e-09	1.64627e-08	3.75	1.32953e-07	1.28008e-09	1.01958e-08
3.85	1.69954e-07	1.62188e-09	1.26139e-08	3.85	1.0164e-07	9.75133e-10	7.7845e-09
3.95	1.33836e-07	1.29572e-09	9.84531e-09	3.95	7.82349e-08	7.58221e-10	5.98022e-09
4.05	9.9587e-08	9.83947e-10	7.28771e-09	4.05	6.08283e-08	5.98462e-10	4.63088e-09
4.15	7.88823e-08	7.72639e-10	5.72436e-09	4.15	4.64247e-08	4.53123e-10	3.53586e-09
4.25	6.09057e-08	6.04472e-10	4.38847e-09	4.25	3.60986e-08	3.50488e-10	2.74421e-09
4.35	4.79312e-08	4.67121e-10	3.42785e-09	4.35	2.81491e-08	2.79144e-10	2.13612e-09
4.45	3.75657e-08	3.68777e-10	2.66639e-09	4.45	2.27112e-08	2.27962e-10	1.71479e-09
4.55	3.04531e-08	2.99578e-10	2.14343e-09	4.55	1.81132e-08	1.81084e-10	1.36449e-09
4.65	2.3967e-08	2.38313e-10	1.67462e-09	4.65	1.43822e-08	1.45357e-10	1.07985e-09
4.75	1.90834e-08	1.89229e-10	1.32364e-09	4.75	1.15701e-08	1.17557e-10	8.65429e-10
4.85	1.54776e-08	1.52713e-10	1.06582e-09	4.85	9.08571e-09	9.17132e-11	6.7814e-10
4.95	1.22941e-08	1.21965e-10	8.3951e-10	4.95	7.34511e-09	7.49942e-11	5.46884e-10
5.05	1.00984e-08	9.93502e-11	6.80265e-10	5.05	5.74908e-09	5.91846e-11	4.25509e-10
5.15	8.10156e-09	8.14497e-11	5.41642e-10	5.15	4.63302e-09	4.7969e-11	3.41482e-10

Table A.4: Photonic electron invariant yield (centrality: 40-60% and Minimum Bias) in Au + Au collisions at $\sqrt{s_{NN}} = 62.4$ GeV

Centrality 40-60%				Minimum Bias			
p_T	*inv.yield*	**stat. error**	**syst. error**	p_T	*inv.yield*	**stat. error**	**syst. error**
1.05	0.00118574	6.61131e-06	0.000111148	1.05	0.00249627	1.40548e-05	0.000212314
1.15	0.000679376	3.95723e-06	6.32787e-05	1.15	0.00146293	8.54059e-06	0.000124261
1.25	0.000403179	2.4414e-06	3.72815e-05	1.25	0.000873469	5.28724e-06	7.41096e-05
1.35	0.000242923	1.50158e-06	2.23178e-05	1.35	0.000533261	3.36823e-06	4.51501e-05
1.45	0.000147361	9.49234e-07	1.34553e-05	1.45	0.000330673	2.16944e-06	2.79452e-05
1.55	9.60326e-05	6.35048e-07	8.68521e-06	1.55	0.000205664	1.39717e-06	1.73677e-05
1.65	6.07914e-05	4.15357e-07	5.4576e-06	1.65	0.000128937	8.96336e-07	1.08728e-05
1.75	3.97772e-05	2.77456e-07	3.54114e-06	1.75	8.51155e-05	6.04595e-07	7.15623e-06
1.85	2.62723e-05	1.88401e-07	2.31923e-06	1.85	5.51111e-05	3.99691e-07	4.62912e-06
1.95	1.74379e-05	1.27926e-07	1.52712e-06	1.95	3.69064e-05	2.77466e-07	3.08618e-06
2.05	1.19128e-05	8.89018e-08	1.03403e-06	2.05	2.42554e-05	1.86463e-07	2.02717e-06
2.15	8.19896e-06	6.27143e-08	7.04783e-07	2.15	1.63179e-05	1.27656e-07	1.36009e-06
2.25	5.59608e-06	4.37675e-08	4.76945e-07	2.25	1.1319e-05	9.00333e-08	9.39601e-07
2.35	3.89163e-06	3.09587e-08	3.28947e-07	2.35	7.84518e-06	6.37667e-08	6.49506e-07
2.45	2.73584e-06	2.1779e-08	2.29113e-07	2.45	5.33496e-06	4.45915e-08	4.40674e-07
2.55	1.97555e-06	1.60152e-08	1.63606e-07	2.55	3.83168e-06	3.22678e-08	3.15103e-07
2.65	1.42326e-06	1.17818e-08	1.16711e-07	2.65	2.69213e-06	2.31271e-08	2.207e-07
2.75	1.05205e-06	8.85766e-09	8.51944e-08	2.75	1.91969e-06	1.66522e-08	1.57042e-07
2.85	7.53064e-07	6.46564e-09	6.05331e-08	2.85	1.38654e-06	1.22546e-08	1.1279e-07
2.95	5.45245e-07	4.73689e-09	4.34191e-08	2.95	9.74467e-07	8.59589e-09	7.91905e-08
3.05	4.17372e-07	3.61563e-09	3.28094e-08	3.05	7.21066e-07	6.56406e-09	5.83218e-08
3.15	3.10129e-07	2.75233e-09	2.40996e-08	3.15	5.19766e-07	4.764e-09	4.18732e-08
3.25	2.30825e-07	2.04543e-09	1.77648e-08	3.25	3.97404e-07	3.6374e-09	3.1809e-08
3.35	1.70671e-07	1.55194e-09	1.30145e-08	3.35	3.08285e-07	2.83531e-09	2.4494e-08
3.45	1.31006e-07	1.19912e-09	9.86443e-09	3.45	2.2153e-07	2.0717e-09	1.75714e-08
3.55	9.88553e-08	9.04222e-10	7.37824e-09	3.55	1.66615e-07	1.56964e-09	1.31652e-08
3.65	7.75932e-08	7.18716e-10	5.70648e-09	3.65	1.23739e-07	1.18662e-09	9.74402e-09
3.75	6.07192e-08	5.67075e-10	4.4078e-09	3.75	9.60369e-08	9.23281e-10	7.52063e-09
3.85	4.69938e-08	4.41597e-10	3.37117e-09	3.85	7.32949e-08	6.96005e-10	5.70259e-09
3.95	3.60417e-08	3.44031e-10	2.56045e-09	3.95	5.45128e-08	5.36606e-10	4.22887e-09
4.05	2.87372e-08	2.75841e-10	2.01213e-09	4.05	4.26292e-08	4.20958e-10	3.28688e-09
4.15	2.28074e-08	2.2417e-10	1.57743e-09	4.15	3.31811e-08	3.23693e-10	2.54563e-09
4.25	1.79001e-08	1.75878e-10	1.22292e-09	4.25	2.64389e-08	2.61942e-10	2.01243e-09
4.35	1.39225e-08	1.37091e-10	9.41052e-10	4.35	2.02417e-08	1.9955e-10	1.53504e-09
4.45	1.1277e-08	1.12291e-10	7.51641e-10	4.45	1.55499e-08	1.53186e-10	1.17575e-09
4.55	8.99513e-09	9.14174e-11	5.9077e-10	4.55	1.25469e-08	1.25415e-10	9.39277e-10
4.65	7.24262e-09	7.27139e-11	4.70449e-10	4.65	9.94396e-09	9.91905e-11	7.40169e-10
4.75	5.66484e-09	5.7442e-11	3.64472e-10	4.75	8.29745e-09	8.37057e-11	6.11587e-10
4.85	4.65387e-09	4.70764e-11	2.94279e-10	4.85	6.57808e-09	6.6567e-11	4.82707e-10
4.95	3.80366e-09	3.82613e-11	2.37515e-10	4.95	5.22582e-09	5.29444e-11	3.81314e-10
5.05	3.10255e-09	3.16664e-11	1.9009e-10	5.05	4.17092e-09	4.20257e-11	3.00383e-10
5.15	2.46353e-09	2.52098e-11	1.49456e-10	5.15	3.37235e-09	3.4162e-11	2.41163e-10

Tables of Heavy Flavor Electron Invariant Yield

Table A.5: Heavy Flavor electron invariant yield (centrality: 0-20% and 20-40%) in Au + Au collisions at $\sqrt{s_{NN}} = 62.4$ GeV

Centrality 0-20%				Centrality 20-40%			
p_T	*inv.yield*	**stat. error**	**syst. error**	p_T	*inv.yield*	**stat. error**	**syst. error**
1.05	0.0018664	8.49879e-05	0.00110871	1.05	0.000651313	3.85909e-05	0.000473389
1.15	0.00136509	5.71611e-05	0.000683261	1.15	0.000508035	2.63425e-05	0.000291444
1.25	0.000832841	3.73923e-05	0.000404387	1.25	0.000353072	1.78857e-05	0.000176886
1.35	0.000500613	2.51374e-05	0.000241878	1.35	0.000217566	1.22624e-05	0.000108207
1.45	0.000328916	1.83129e-05	0.000154818	1.45	0.000135222	8.88317e-06	6.69786e-05
1.55	0.000237185	1.3581e-05	9.953e-05	1.55	0.000106592	6.8595e-06	4.48897e-05
1.65	0.000151285	1.01266e-05	6.33615e-05	1.65	9.01659e-05	5.35034e-06	3.09943e-05
1.75	0.000104788	7.70416e-06	4.1243e-05	1.75	4.74687e-05	3.94064e-06	1.87499e-05
1.85	7.55062e-05	6.11353e-06	2.80015e-05	1.85	3.59139e-05	3.13875e-06	1.28952e-05
1.95	5.20222e-05	4.81025e-06	1.84974e-05	1.95	2.6215e-05	2.48711e-06	8.70358e-06
2.05	3.69895e-05	3.84466e-06	1.26412e-05	2.05	1.91868e-05	2.0674e-06	6.08099e-06
2.15	2.06808e-05	3.00145e-06	7.82796e-06	2.15	1.26896e-05	1.65075e-06	4.10989e-06
2.25	1.81251e-05	2.58004e-06	5.90369e-06	2.25	9.05647e-06	1.32221e-06	2.81311e-06
2.35	1.47939e-05	2.03778e-06	4.33975e-06	2.35	5.93794e-06	1.07845e-06	1.93742e-06
2.45	1.00149e-05	1.66197e-06	2.93509e-06	2.45	4.8625e-06	8.86077e-07	1.43365e-06
2.55	6.84167e-06	1.34697e-06	1.98489e-06	2.55	3.23099e-06	7.26492e-07	9.84559e-07
2.65	7.67045e-06	1.2095e-06	1.78005e-06	2.65	2.49792e-06	6.02629e-07	7.19315e-07
2.75	4.12696e-06	9.90649e-07	1.08652e-06	2.75	2.03913e-06	5.35299e-07	5.4527e-07
2.85	4.81969e-06	9.67321e-07	1.02232e-06	2.85	1.92274e-06	4.76143e-07	4.54338e-07
2.95	2.53128e-06	7.08345e-07	6.09982e-07	2.95	8.01869e-07	3.717e-07	2.50451e-07
3.05	3.16402e-06	6.87195e-07	6.18226e-07	3.05	8.75993e-07	3.46143e-07	2.20814e-07
3.15	1.64961e-06	5.4837e-07	3.65973e-07	3.15	3.47592e-07	2.63185e-07	1.22171e-07
3.25	1.72359e-06	4.5813e-07	3.3344e-07	3.25	5.69758e-07	2.73e-07	1.33891e-07
3.35	1.01514e-06	4.35712e-07	2.10549e-07	3.35	2.45751e-07	2.0195e-07	7.34336e-08
3.45	6.82806e-07	3.38261e-07	1.47853e-07	3.45	4.63756e-07	1.92386e-07	9.18905e-08
3.55	-2.70186e-08	2.48406e-07	4.2847e-08	3.55	5.95834e-07	2.1485e-07	1.03366e-07
3.65	7.79407e-07	2.8752e-07	1.37377e-07	3.65	8.75808e-09	9.12437e-08	2.01797e-08
3.75	2.5858e-07	2.09653e-07	5.78016e-08	3.75	1.65536e-07	1.18118e-07	3.51714e-08
3.85	5.96186e-07	2.66258e-07	9.89892e-08	3.85	1.35093e-07	1.07248e-07	2.79754e-08
3.95	2.33039e-07	1.79876e-07	4.5197e-08	3.95	8.94794e-08	7.70577e-08	1.9541e-08
4.05	2.76263e-07	1.51405e-07	4.77387e-08	4.05	-2.30259e-08	5.35858e-08	4.85363e-09
4.15	2.72648e-07	1.31298e-07	4.52129e-08	4.15	1.0999e-07	8.95657e-08	1.92756e-08
4.25	-5.93945e-08	1.0365e-07	5.42853e-09	4.25	1.42141e-07	8.11644e-08	2.28043e-08
4.35	2.90056e-07	1.43077e-07	4.47385e-08	4.35	1.4586e-07	8.07967e-08	2.26407e-08
4.45	1.82295e-07	1.02603e-07	2.8756e-08	4.45	2.78745e-08	4.00925e-08	5.85078e-09
4.55	3.19146e-08	4.99314e-08	7.29091e-09	4.55	2.93421e-08	3.90267e-08	5.61429e-09
4.65	-4.87487e-09	6.30343e-08	2.10247e-09	4.65	3.05769e-08	3.82162e-08	5.4418e-09
4.75	3.724e-08	4.84082e-08	6.88626e-09	4.75	3.17308e-08	3.78362e-08	5.35167e-09
4.85	-8.88183e-09	8.15656e-11	1.06582e-09	4.85	3.16116e-08	3.63847e-08	5.1243e-09
4.95	4.77625e-08	7.55125e-08	7.71201e-09	4.95	-3.7436e-09	3.4944e-11	5.46884e-10
5.05	-5.66887e-09	5.20875e-11	6.80265e-10	5.05	-2.8963e-09	2.72947e-11	4.25509e-10
5.15	4.06513e-08	4.5275e-08	6.34626e-09	5.15	-2.31129e-09	2.18766e-11	3.41482e-10

Table A.6: Heavy Flavor electron invariant yield (centrality: 40-60% and Minimum Bias) in Au + Au collisions at $\sqrt{s_{NN}} = 62.4$ GeV

Centrality 40-60%				Minimum Bias			
p_T	*inv.yield*	**stat. error**	**syst. error**	p_T	*inv.yield*	**stat. error**	**syst. error**
1.05	9.88175e-05	1.45104e-05	0.000161793	1.05	0.000383724	2.3883e-05	0.000356021
1.15	8.27139e-05	1.01131e-05	9.48379e-05	1.15	0.000309442	1.55113e-05	0.000217354
1.25	6.40884e-05	7.17419e-06	5.74942e-05	1.25	0.000195213	9.88492e-06	0.000130464
1.35	4.35585e-05	5.1391e-06	3.49745e-05	1.35	0.00011703	6.43099e-06	7.90277e-05
1.45	3.78247e-05	3.91895e-06	2.23562e-05	1.45	8.3243e-05	4.5122e-06	5.00166e-05
1.55	2.20299e-05	2.97164e-06	1.41654e-05	1.55	6.25514e-05	3.26781e-06	3.22606e-05
1.65	1.47388e-05	2.25166e-06	9.0006e-06	1.65	4.60404e-05	2.39635e-06	2.09572e-05
1.75	1.02363e-05	1.75985e-06	5.91521e-06	1.75	2.78682e-05	1.76761e-06	1.34664e-05
1.85	7.16308e-06	1.4085e-06	3.92576e-06	1.85	2.15003e-05	1.38006e-06	9.10257e-06
1.95	4.75074e-06	1.10985e-06	2.58881e-06	1.95	1.46952e-05	1.07481e-06	6.09633e-06
2.05	4.09961e-06	9.215e-07	1.85415e-06	2.05	1.09807e-05	8.59525e-07	4.15541e-06
2.15	3.62945e-06	7.6395e-07	1.36238e-06	2.15	7.14475e-06	6.77342e-07	2.75396e-06
2.25	2.62319e-06	6.42072e-07	9.42052e-07	2.25	5.5538e-06	5.64005e-07	1.97347e-06
2.35	1.86319e-06	5.05843e-07	6.56259e-07	2.35	4.23841e-06	4.49236e-07	1.41031e-06
2.45	8.71961e-07	4.02703e-07	4.06609e-07	2.45	2.93907e-06	3.6392e-07	9.62546e-07
2.55	6.99733e-07	3.40518e-07	2.9933e-07	2.55	2.01023e-06	2.98258e-07	6.75372e-07
2.65	7.57553e-07	2.92865e-07	2.44625e-07	2.65	1.99756e-06	2.59071e-07	5.46289e-07
2.75	7.70132e-07	2.69893e-07	2.05796e-07	2.75	1.34541e-06	2.19942e-07	3.78236e-07
2.85	6.2412e-07	2.37598e-07	1.5609e-07	2.85	1.3702e-06	2.05414e-07	3.2338e-07
2.95	1.71182e-08	1.26017e-07	6.10527e-08	2.95	6.01684e-07	1.50048e-07	1.80247e-07
3.05	4.59882e-07	1.96898e-07	1.00511e-07	3.05	8.45024e-07	1.50401e-07	1.8466e-07
3.15	2.50097e-07	1.55091e-07	6.23521e-08	3.15	4.28336e-07	1.17742e-07	1.08971e-07
3.25	1.726e-07	1.28985e-07	4.44488e-08	3.25	4.73741e-07	1.05551e-07	1.02111e-07
3.35	1.49802e-07	1.16264e-07	3.55845e-08	3.35	2.59478e-07	9.22473e-08	6.46658e-08
3.45	1.10633e-07	8.86338e-08	2.65927e-08	3.45	2.39955e-07	7.49331e-08	5.33545e-08
3.55	7.66595e-08	7.29947e-08	1.91012e-08	3.55	1.40957e-07	6.59482e-08	3.48279e-08
3.65	8.43777e-08	7.09896e-08	1.8064e-08	3.65	1.55467e-07	5.6028e-08	3.24725e-08
3.75	1.26414e-07	7.82266e-08	2.22528e-08	3.75	1.10522e-07	4.84686e-08	2.37667e-08
3.85	1.31195e-07	7.71417e-08	2.17763e-08	3.85	1.64482e-07	5.47832e-08	2.89302e-08
3.95	5.81802e-08	5.34074e-08	1.08417e-08	3.95	7.4916e-08	3.75304e-08	1.50314e-08
4.05	-1.34142e-08	1.17024e-10	2.01213e-09	4.05	3.80631e-08	2.8433e-08	8.99461e-09
4.15	2.49233e-08	3.55576e-08	5.20626e-09	4.15	7.64479e-08	3.12459e-08	1.32941e-08
4.25	-8.15279e-09	7.24586e-11	1.22292e-09	4.25	2.77927e-08	2.64322e-08	6.07854e-09
4.35	6.20979e-08	4.84948e-08	9.61817e-09	4.35	9.7516e-08	3.26239e-08	1.51304e-08
4.45	-5.01094e-09	4.49366e-11	7.51641e-10	4.45	3.6082e-08	1.96126e-08	6.23044e-09
4.55	-3.93846e-09	3.59985e-11	5.9077e-10	4.55	1.09607e-08	1.20728e-08	2.56113e-09
4.65	-3.13633e-09	2.82498e-11	4.70449e-10	4.65	5.34086e-09	1.35371e-08	1.59495e-09
4.75	-2.42981e-09	2.19877e-11	3.64472e-10	4.75	1.25982e-08	1.17045e-08	2.39016e-09
4.85	-1.96186e-09	1.77232e-11	2.94279e-10	4.85	4.86861e-09	7.95847e-09	1.21143e-09
4.95	2.90527e-08	3.07082e-08	4.29563e-09	4.95	1.50354e-08	1.50603e-08	2.47217e-09
5.05	-1.26727e-09	1.15433e-11	1.9009e-10	5.05	-1.89057e-09	1.71077e-11	3.00383e-10
5.15	-9.96374e-10	9.04838e-12	1.49456e-10	5.15	6.21073e-09	7.74029e-09	1.10755e-09

Tables of R_{np}

Table A.7: R_{np} (centrality: 0-20% and 20-40%) in Au + Au collisions at $\sqrt{s_{NN}}$ = 62.4 GeV

Centrality 0-20%				Centrality 20-40%			
p_T	R_{np}	**stat. error**	**syst. error**	p_T	R_{np}	**stat. error**	**syst. error**
1.05	0.383576	0.0182056	0.255119	1.05	0.294339	0.0179939	0.233452
1.15	0.477861	0.0209238	0.272504	1.15	0.394588	0.0211818	0.252265
1.25	0.497506	0.0232774	0.276126	1.25	0.471236	0.0246939	0.266904
1.35	0.50079	0.0260522	0.276732	1.35	0.476886	0.027677	0.268711
1.45	0.518689	0.0297815	0.280032	1.45	0.48057	0.0323018	0.270167
1.55	0.607901	0.0357767	0.296482	1.55	0.601464	0.0395214	0.293082
1.65	0.609564	0.0416868	0.296789	1.65	0.816391	0.0494598	0.333388
1.75	0.666638	0.0498956	0.307313	1.75	0.66236	0.0557208	0.306011
1.85	0.728277	0.0598209	0.318678	1.85	0.765737	0.0676788	0.325994
1.95	0.776705	0.0726263	0.327608	1.95	0.868247	0.0831126	0.345933
2.2	0.837481	0.0542783	0.338815	2.2	0.93193	0.0625227	0.359832
2.6	1.23308	0.113995	0.411759	2.6	1.09535	0.121464	0.394892
3	2.08568	0.254929	0.568972	3	1.31936	0.24871	0.442302
3.4	2.09077	0.467413	0.56991	3.4	2.16094	0.513449	0.609965
3.8	3.64109	0.934972	0.855775	3.8	1.45481	0.726892	0.479348
4.5	4.18454	1.22014	0.955982	4.5	3.81199	1.29234	0.959332

Table A.8: R_{np} (centrality: 40-60% and Minimum Bias) in Au + Au collisions at $\sqrt{s_{NN}} = 62.4$ GeV

Centrality 40-60%				Minimum Bias			
p_T	R_{np}	**stat. error**	**syst. error**	p_T	R_{np}	**stat. error**	**syst. error**
1.05	0.13336	0.0197896	0.232546	1.05	0.231493	0.0149266	0.233678
1.15	0.19607	0.0242502	0.245413	1.15	0.320881	0.0167993	0.251327
1.25	0.257856	0.0292	0.25809	1.25	0.341447	0.0180541	0.255941
1.35	0.29276	0.0348753	0.265252	1.35	0.337986	0.0193379	0.255982
1.45	0.42167	0.0441233	0.291702	1.45	0.390713	0.0220318	0.2668
1.55	0.380473	0.0516681	0.283249	1.55	0.475176	0.0258025	0.283782
1.65	0.40509	0.0622139	0.2883	1.65	0.561935	0.0303099	0.301298
1.75	0.433601	0.0748522	0.29415	1.75	0.519786	0.0338649	0.293974
1.85	0.463284	0.0913825	0.300241	1.85	0.623511	0.0409816	0.314901
1.95	0.466637	0.109265	0.300929	1.95	0.642888	0.0479326	0.319537
2.2	0.72005	0.0853823	0.352925	2.2	0.766235	0.0358255	0.345421
2.6	0.781849	0.166684	0.365605	2.6	1.02193	0.0714732	0.399801
3	1.25999	0.342809	0.46371	3	1.58597	0.155464	0.516984
3.4	1.59207	0.650266	0.531848	3.4	1.86753	0.288474	0.579611
3.8	3.74083	1.32081	0.972738	3.8	2.76879	0.545091	0.770197
4.5	1.38307	1.19683	0.488965	4.5	3.62853	0.765329	0.96422
5.5	nan	nan	nan	5.5	0.2507	1.7556	0.267757

Tables of Inclusive Eelectron dN/dϕ Distribution w.r.t. Reaction Plane

Table A.9: Inclusive electron dN/dϕ distribution vs $\phi - \Phi_{rp}$ in Au + Au collisions at $\sqrt{s_{NN}} =$ 62.4 GeV (centrality: 0-20%)

	p_T 1-1.3 GeV/c		p_T 1.3-1.6 GeV/c		p_T 1.6-1.9 GeV/c	
$\phi - \Phi_{rp}$	**dN/dϕ**	**stat. error**	**dN/dϕ**	**stat. error**	**dN/dϕ**	**stat. error**
0.0523599	4957.61	89.2496	1619.83	49.9799	481.625	27.9241
0.15708	4850.15	87.9519	1549.87	50.3124	465.91	28.2487
0.261799	4793.29	87.9055	1534.63	49.9839	497.743	28.3678
0.366519	4829.12	86.7416	1606.34	49.7262	453.969	26.7433
0.471239	4769.81	87.2068	1533.91	49.6805	440.949	26.9406
0.575959	4694.13	86.3284	1429.35	48.5712	481.714	27.3652
0.680678	4472.46	85.3294	1458.08	48.2736	496.106	27.2503
0.785398	4396.77	84.0547	1442.02	48.8377	482.244	26.72
0.890118	4334.97	83.5539	1540.98	48.7932	442.273	26.7178
0.994838	4363.29	84.1628	1388.95	48.3677	428.341	26.3159
1.09956	4287.83	82.9784	1423.45	47.9444	379.596	25.2563
1.20428	4397.7	83.2044	1356.81	47.5245	436.273	26.6052
1.309	4115.91	82.6622	1340.47	46.1367	455.459	26.9907
1.41372	4288.54	82.7779	1296.73	46.2863	423.341	26.2207
1.51844	4263.59	81.8103	1401.11	46.5046	415.851	25.8501

Table A.10: Inclusive electron dN/dϕ distribution vs $\phi - \Phi_{rp}$ in Au + Au collisions at $\sqrt{s_{NN}}$ = 62.4 GeV (centrality: 0-20%)

	p_T 1.9-2.2 GeV/c		p_T 2.2-2.5 GeV/c		$p_T > 2.5$ GeV/c		
$\phi - \Phi_{rp}$	**dN/dϕ**	**stat. error**	**dN/dϕ**	**stat. error**	$\phi - \Phi_{rp}$	**dN/dϕ**	**stat. error**
0.0523599	164.391	17.1543	73.7742	10.9328	0.15708	176.176	16.2705
0.15708	179.156	17.0682	65.0291	10.241	0.471239	163.548	15.9704
0.261799	171.901	17.0286	66.8429	10.2575	0.785398	134.941	14.3452
0.366519	178.362	16.3827	74.4704	10.4829	1.09956	138.5	14.6209
0.471239	169.97	16.753	55.0978	9.35776	1.41372	146.921	15.5364
0.575959	170.852	16.5133	58.5879	10.1422			
0.680678	192.48	17.0694	74.2154	10.749			
0.785398	176.107	16.4937	62.0978	9.72459			
0.890118	180.411	16.9315	53.333	10.1742			
0.994838	184.431	16.3426	61.2841	9.75858			
1.09956	153.666	15.9382	60.2154	10.0767			
1.20428	156.666	16.0321	65.2154	10.3219			
1.309	167.362	16.0434	56.8429	9.75788			
1.41372	157.803	15.6015	49.5879	9.68839			
1.51844	141.529	16.0203	75.794	9.89608			

Table A.11: Inclusive electron dN/dϕ distribution vs $\phi - \Phi_{rp}$ in Au + Au collisions at $\sqrt{s_{NN}}$ = 62.4 GeV (centrality: 20-40%)

	p_T 1-1.3 GeV/c		p_T 1.3-1.6 GeV/c		p_T 1.6-1.9 GeV/c	
$\phi - \Phi_{rp}$	**dN/dϕ**	**stat. error**	**dN/dϕ**	**stat. error**	**dN/dϕ**	**stat. error**
0.0523599	2854.36	59.012	1002.63	34.5135	341.805	19.6034
0.15708	2892.07	58.9489	933.633	33.499	314	19.1948
0.261799	2825.73	57.6166	935.145	33.4819	328.633	20.2065
0.366519	2743.04	58.1868	939.535	33.0891	333.731	19.8029
0.471239	2606.68	56.2644	903.73	32.7267	276.024	18.032
0.575959	2652.02	56.9697	897.071	33.1496	294.195	18.9891
0.680678	2479.43	54.6139	847.95	31.9671	286.219	18.6359
0.785398	2378.51	53.5333	826.365	31.0557	263.073	17.366
0.890118	2383.65	53.7916	830.999	31.5328	268.78	17.7927
0.994838	2296.19	52.8971	800.925	31.3078	236.78	16.8695
1.09956	2303.78	52.793	686.633	29.5835	234.756	16.9667
1.20428	2207.41	51.5899	702.511	29.3799	241.512	17.1259
1.309	2234.51	51.6466	726.121	29.3749	212.024	16.1602
1.41372	2175.65	51.2942	726.609	29.4284	259.585	17.1882
1.51844	2097.04	50.7581	722.365	29.3335	253.78	17.3661

Table A.12: Inclusive electron dN/dϕ distribution vs $\phi - \Phi_{rp}$ in Au + Au collisions at $\sqrt{s_{NN}}$ = 62.4 GeV (centrality: 20-40%)

	p_T 1.9-2.2 GeV/c		p_T 2.2-2.5 GeV/c		$p_T > 2.5$ GeV/c		
$\phi - \Phi_{rp}$	**dN/dϕ**	**stat. error**	**dN/dϕ**	**stat. error**	$\phi - \Phi_{rp}$	**dN/dϕ**	**stat. error**
0.0523599	147.146	13.0276	44.195	7.49302	0.15708	105.902	11.276
0.15708	126.902	12.1716	54.7072	8.00012	0.471239	90.1462	10.6169
0.261799	107.609	11.7537	43.9756	7.02046	0.785398	93.39	10.8301
0.366519	92.9023	10.684	40.7072	7.0712	1.09956	63.4145	9.0556
0.471239	109.414	11.3139	47.7072	7.54996	1.41372	70.9267	9.31989
0.575959	123.878	12.2652	40.4389	7.32919			
0.680678	110.39	11.5884	41.7317	6.76129			
0.785398	100.122	11.314	37.2195	6.62258			
0.890118	103.902	11.1869	48.9511	7.71839			
0.994838	98.1462	10.9872	35.9511	6.82449			
1.09956	70.6584	9.51712	26.4633	5.86773			
1.20428	92.4389	10.2819	25.9756	5.59346			
1.309	93.9267	10.4814	26.2195	5.73223			
1.41372	100.414	10.9089	23.7317	5.26451			
1.51844	89.1706	10.3166	29.4633	6.11802			

Table A.13: Inclusive electron dN/dϕ distribution vs $\phi - \Phi_{rp}$ in Au + Au collisions at $\sqrt{s_{NN}}$ = 62.4 GeV (centrality: 40-60%)

	p_T 1-1.3 GeV/c		p_T 1.3-1.6 GeV/c		p_T 1.6-1.9 GeV/c	
$\phi - \Phi_{rp}$	**dN/dϕ**	**stat. error**	**dN/dϕ**	**stat. error**	**dN/dϕ**	**stat. error**
0.0523599	972.717	32.1119	318.41	18.3579	93.4871	9.80532
0.15708	946.396	31.9292	325.358	18.8305	93.9743	9.96438
0.261799	930.37	31.761	324.897	18.6052	90.9743	9.81268
0.366519	925.768	31.2025	331.923	18.6512	102.974	10.4062
0.471239	887.96	30.7855	295.141	17.8249	92.2178	9.94289
0.575959	891.473	30.7994	324.141	18.6206	94.9485	10.2751
0.680678	851.499	30.0552	279.41	17.263	84.9743	9.50204
0.785398	805.768	29.2164	283.461	17.0714	98.7307	10.1349
0.890118	788.473	29.0793	271.949	16.81	91.2436	9.62144
0.994838	828.96	29.8119	271.653	17.0758	86.4614	9.71767
1.09956	745.499	28.2368	259.141	16.7847	68.4871	8.43471
1.20428	793.743	29.1013	251.166	16.3841	74.2178	8.99227
1.309	709.473	27.6876	241.974	15.7254	85.2178	9.58441
1.41372	740.255	28.1202	254.166	16.4754	80.4614	9.40389
1.51844	754.307	28.1809	246.436	16.1159	68.7307	8.5274

Table A.14: Inclusive electron dN/dϕ distribution vs $\phi - \Phi_{rp}$ in Au + Au collisions at $\sqrt{s_{NN}}$ = 62.4 GeV (centrality: 40-60%)

	p_T 1.9-2.2 GeV/c		p_T 2.2-2.5 GeV/c		$p_T > 2.5$ GeV/c		
$\phi - \Phi_{rp}$	**dN/dϕ**	**stat. error**	**dN/dϕ**	**stat. error**	$\phi - \Phi_{rp}$	**dN/dϕ**	**stat. error**
0.0523599	44	6.63325	9.24356	3.25149	0.15708	28.2436	5.43803
0.15708	29.2436	5.52921	20.4871	4.81086	0.471239	43.2178	7.06123
0.261799	45.7307	7.051	18	4.24264	0.785398	42	6.48074
0.366519	31.4871	5.84332	12	3.4641	1.09956	26	5.09902
0.471239	38	6.16441	14	3.74166	1.41372	28.2436	5.43803
0.575959	36.2436	6.12962	19.7307	4.86997			
0.680678	28.4871	5.58072	8	2.82843			
0.785398	34.2436	5.96424	11.2436	3.54573			
0.890118	21.4871	4.91369	16	4			
0.994838	35.2436	6.0475	15.4871	4.25962			
1.09956	35.7307	6.30211	14	3.74166			
1.20428	39.4871	6.49187	16	4			
1.309	40.2436	6.44765	8	2.82843			
1.41372	34	5.83095	9	3			
1.51844	27.2436	5.3453	10.2436	3.40179			

Tables of Inclusive Electron ${v_2}^{raw}$

Table A.15: Inclusive electron ${v_2}^{raw}$ in Au + Au collisions at $\sqrt{s_{NN}}$ = 62.4 GeV (centrality: 0-20%, 20-40% and 40-60%)

Centrality 0-20%			Centrality 20-40%			Centrality 40-60%		
p_T	${v_2}^{raw}$	**stat. error**	p_T	${v_2}^{raw}$	**stat. error**	p_T	${v_2}^{raw}$	**stat. error**
1.15	0.0377337	0.00343961	1.15	0.0717088	0.00402341	1.15	0.0654557	0.00650033
1.45	0.0399913	0.00602966	1.45	0.0801968	0.00688108	1.45	0.073302	0.0110693
1.75	0.0337465	0.0109097	1.75	0.0858577	0.0119903	1.75	0.0642915	0.0199536
2.05	0.0285613	0.0176706	2.05	0.079292	0.0196487	2.05	0.0253166	0.0327775
2.35	0.0277411	0.0292374	2.35	0.154052	0.0314399	2.35	0.0681766	0.0521207
3.25	0.0554675	0.0328572	3.25	0.116749	0.0376862	3.25	0.0514709	0.0546229

Tables of Inclusive Electron v_2

Table A.16: Inclusive electron v_2 in Au + Au collisions at $\sqrt{s_{NN}} = 62.4$ GeV (centrality: 0-20%)

p_T	v_2	**stat. error**	**syst. error**
1.15	0.0700903	0.00638907	0.00350451
1.45	0.0742839	0.0112001	0.0037142
1.75	0.0626842	0.0202647	0.00313421
2.05	0.0530526	0.0328231	0.00265263
2.35	0.0515292	0.0543085	0.00257646
3.25	0.103031	0.0610324	0.00515155

Table A.17: Inclusive electron v_2 in Au + Au collisions at $\sqrt{s_{NN}} = 62.4$ GeV (centrality: 20-40%)

p_T	v_2	**stat. error**	**syst. error**
1.15	0.115108	0.00645844	0.0057554
1.45	0.128733	0.0110456	0.00643665
1.75	0.13782	0.019247	0.006891
2.05	0.127281	0.0315403	0.00636404
2.35	0.247286	0.0504678	0.0123643
3.25	0.187408	0.0604944	0.00937039

Table A.18: Inclusive electron v_2 in Au + Au collisions at $\sqrt{s_{NN}} = 62.4$ GeV (centrality: 40-60%)

p_T	v_2	**stat. error**	**syst. error**
1.15	0.154648	0.015358	0.00773242
1.45	0.173187	0.0261529	0.00865933
1.75	0.151898	0.0471432	0.0075949
2.05	0.0598141	0.0774415	0.00299071
2.35	0.161077	0.123143	0.00805385
3.25	0.121607	0.129054	0.00608037

Tables of Photonic Electron v_2

Table A.19: Photonic electron v_2 in Au + Au collisions at $\sqrt{s_{NN}}$ = 62.4 GeV (centrality: 0-20%)

p_T	v_2	**stat. error**	**syst. error**
1.15	0.0736391	0.00227136	0.00471291
1.45	0.0856241	0.00250792	0.00547994
1.75	0.0974553	0.00301315	0.00623714
2.05	0.0904097	0.00270129	0.00578622
2.35	0.0989942	0.00302541	0.00633563
3.25	0.0959512	0.0022071	0.00614088

Table A.20: Photonic electron v_2 in Au + Au collisions at $\sqrt{s_{NN}}$ = 62.4 GeV (centrality: 20-40%)

p_T	v_2	**stat. error**	**syst. error**
1.15	0.140513	0.0022645	0.00899286
1.45	0.15889	0.00242871	0.010169
1.75	0.170093	0.00289051	0.0108859
2.05	0.177383	0.00251164	0.0113525
2.35	0.170773	0.00284	0.0109294
3.25	0.169412	0.00204107	0.0108424

Table A.21: Photonic electron v_2 in Au + Au collisions at $\sqrt{s_{NN}}$ = 62.4 GeV (centrality: 40-60%)

p_T	v_2	**stat. error**	**syst. error**
1.15	0.181978	0.00221142	0.0116466
1.45	0.187403	0.00235834	0.0119938
1.75	0.195614	0.00277549	0.0125193
2.05	0.203373	0.00242	0.0130159
2.35	0.204871	0.00273789	0.0131117
3.25	0.21079	0.00189584	0.0134906

Tables of Heavy Flavor Electron v_2

Table A.22: Heavy Flavor electron v_2 in Au + Au collisions at $\sqrt{s_{NN}}$ = 62.4 GeV (centrality: 0-20%)

p_T	v_2	**stat. error(+)**	**stat. error(-)**	**syst. error (+)**	**syst. error (-)**
1.15	0.0616936	0.0221707	0.0221715	0.00885719	0.0156334
1.45	0.053703	0.0318713	0.0318755	0.0107259	0.021811
1.75	0.012774	0.0496539	0.0496911	0.0179593	0.0393416
2.05	0.0095972	0.0711403	0.0711637	0.0139097	0.0276563
2.35	0.00588851	0.106616	0.106631	0.0134239	0.0251969
3.25	0.107233	0.0972745	0.0972697	0.00602801	0.00574351

Table A.23: Heavy Flavor electron v_2 in Au + Au collisions at $\sqrt{s_{NN}}$ = 62.4 GeV (centrality: 20-40%)

p_T	v_2	**stat. error(+)**	**stat. error(-)**	**syst. error (+)**	**syst. error (-)**
1.15	0.0461808	0.0250372	0.0251095	0.0405645	0.128124
1.45	0.0724147	0.0321566	0.0322001	0.0253856	0.0571644
1.75	0.0922228	0.0467384	0.0467822	0.019141	0.0362636
2.05	0.0707011	0.0673631	0.0674212	0.0201126	0.0383717
2.35	0.318883	0.0979229	0.0978704	0.040802	0.0240721
3.25	0.19831	0.0972196	0.097177	0.0115731	0.0106239

Table A.24: Heavy Flavor electron v_2 in Au + Au collisions at $\sqrt{s_{NN}}$ = 62.4 GeV (centrality: 40-60%)

p_T	v_2	**stat. error(+)**	**stat. error(-)**	**syst. error (+)**	**syst. error (-)**
1.15	0.0111236	0.0980687	0.0989546	0.256923	0.311124
1.45	0.131302	0.103549	0.103626	0.0396055	0.138067
1.75	0.0622758	0.1444	0.144817	0.0449992	0.126619
2.05	-0.166091	0.201699	0.20372	0.0875148	0.133909
2.35	0.105113	0.280622	0.280697	0.0234998	0.04811
3.25	0.0484913	0.236105	0.24122	0.0250248	0.052196

BIBLIOGRAPHY

[1] E.V. Shuryak, Phys. Repts. **61**, 71 (1980).

[2] BNL, BNL:73847:2005 Formal Report (2005),

[3] M. Cacciari, hep-ph/0407187 (2004)

[4] D. Acosta et al., Phys. Rev. Lett. **91**, 241804 (2003).

[5] A. Adare et al., Phys. Rev. Lett. **97**, 252002 (2006).

[6] A. Adare et al., Phys. Rev. Lett. **91**, 072301 (2003)

[7] Y L Dokshitzer and D E Kharzeev, Phys. Lett. **B 519** 199 (2001)

[8] N. Armesto et al., Phys. Rev. **D 71** 054027 (2005)

[9] A. Adare et al., Phys. Rev. Lett. **98**, 172301 (2007)

[10] A. Adare et al., Phys. Rev. **C 84**, 044905 (2011)

[11] S. Wicks et al., Nucl. Phys. **A784**, 426 (2007)

[12] G.Y. Qin and A. Majumder, Phys. Rev. Lett. **105**:262301,2010

[13] G. D. Moore and D. Teaney, Phys. Rev. **C 71**, 064904 (2005)

[14] H. van Hees et al., Phys. Rev. **C 73**, 034913 (2006).

[15] M. G. Mustafa, Phys. Rev. **C 72**, 014905 (2005).

[16] J.J. Aubert et al., (EMC Collaboration), Phys. Lett. **123B**, 275 (1983).

[17] K. J. Eskola et al., hep-ph/0104124.

[18] J. W. Cronin et al. Phys. Rev. **D 11**, 3105 (1975).

[19] A. Adare et al., Phys. Rev. **C 74**, 024904 (2006)

[20] A. Adare et al., Phys. Rev. Lett. **109**, 242301 (2012)

[21] P. J. Siemens and J. O. Rasmussen, Phys. Rev. Lett. **42**, 14 (1979)

[22] P.Houvinen et al. Phys. Lett.**B 503**, 58-64 (2001)

[23] E. Schnedermann et al., Phys. Rev. **C 48**, 2462 (1993)

[24] B. I. Abelev et al.,Phys. Rev. **C 79**, 034909 (2009)

[25] S. Batsouli et al. Phys. Lett. **B 557** 26-32 (2003)

[26] A. Adare et al., Phys. Rev. Lett. **107**, 142301 (2011)

[27] A. Adare et al., Phys. Rev. **C 86**, 064901 (2012)

[28] B. I. Abelev et al., Phys. Rev. Lett. **98**, 192301 (2007)

[29] A. Rossi et al., arXiv:1106.5931

[30] C. Bianchin et al., arXiv:1111.6886

[31] A. Adare et al., Phys. Rev. Lett. 109, 152301 (2012)

[32] L. Adamczyk et al., arXiv:1301.2348

[33] K. Adcox et al., Nucl. Instrum. Methods **A499** 469 (2003).

[34] M. Allen et al., Nucl. Instr. and Meth. **A499** 549 (2003).

[35] C. Adler et al., Nucl. Instr. and Meth. **A470** 488 (2001).

[36] E. Richardson et al., Nucl. Instr. and Meth. **A636** 99-107 (2011).

[37] Z. Fraenkel et al., Nucl. Instrum. Methods **A546** 446 (2005).

[38] W. Anderson et al., Nucl. Instrum. Methods **A646** 35 (2011).

[39] K. Adcox et al., Nucl. Instrum. Methods **A499** 489-507 (2003).

[40] PHENIX webpage

[41] M. Aizawa et al., Nucl. Instrum. Methods **A499** 508-520 (2003).

[42] Y. Akiba et al., Nucl. Instrum. Methods **A433** 143-148 (1999).

[43] L. Aphecetche et al., Nucl. Instrum. Methods **A499** 521-536 (2003)

[44] A. Adare et al., Phys. Rev. Lett. **96**, 202301 (2006)

[45] Y. Riabov (PHENIX), J. Phys. G 34, S925 (2007).

[46] K. Nakamura et al., (Particle Data Group), J. Phys. G 37, 075021 (2010)

[47] Y.Akiba et al., PHENIX analysis note 324.

[48] G. David et al., PHENIX analysis note 592.

[49] X. Gong et al., PHENIX analysis note 940.

[50] Y. Gu et al., PHENIX analysis note 1042.

[51] D. Sharma et al., PHENIX analysis note 999.

[52] M. Basile et al., Il Nuovo Cimento A , Volume 65, Issue 4, pp 421-456 (1981).

[53] R. Vogt, (private communication).

[54] M.Shimomura et al., PHENIX analysis note 777.

[55] S. Cao (private communication).

[56] S. Cao et al., arXiv:1209.5410

[57] C. Shen et al., Phys. Rev. **C 85**, 054902 (2012). arXiv:1202.6620

[58] J. F. Owens, Rev. Mod. Phys. **59** 465 (1987)

[59] K. J. Eskola et al., JHEP 0807:102 (2008), arXiv:0802.0139

[60] Y. Oh et al., Phys. Rev. **C 79** 044905 (2009)

[61] T. Sjostrand et al., PYTHIA 6.4 Physics and Manual, arXiv:hep-ph/0603175

[62] M. L. Miller et al., Ann. Rev. Nucl. Part. Sci.**57** 205-243 (2007)

[63] D. Kharzeev et al., Nucl. Phys. **A 747** 609-629 (2005)

[64] S. Cao et al., arXiv:1205.2396

[65] N. Apadula et al., PHENIX Analysis Note 981

[66] A. Dion, Physics with SVX, PHENIX FOCUS Seminor (2010)

[67] M. Baker et al., Proposal for a Silicon Vertex Tracker (VTX) for the PHENIX Experiment, BNL-72204- 2004, Physics Dept. BNL (2004).

[68] R. Nouicer et al. Journal of Instrumentation, 4, P04011 (2009) [PHENIX] 2011 Nuclear Physics A 862 64

[69] Y. Akiba et al., PHENIX Analysis Note 1064